MODELING OF COUPLED FLOW AND GEOMECHANICS FOR FAULT SLIP, WELLBORE STABILITY, FRACTURE PROPAGATION AND ITS FIELD APPLICATION

A Dissertation

by

SANGCHEOL YOON

Submitted to the Office of Graduate and Professional Studies of
Texas A&M University
in partial fulfillment of the requirements for the degree of

DOCTOR OF PHILOSOPHY

Chair of Committee,	Jihoon Kim
Co-Chairs of Committee,	John Killough
Committee Members,	Eduardo Gildin
	Yalchin Efendiev
Head of Department,	Jeff Spath

August 2021

Major Subject: Petroleum Engineering

ABSTRACT

Coupling between fluid flow and geomechanical responses such as deformation and failure is essential to simulate potential damage in subsurface environments and ground surface structures. To solve the aforementioned coupling problems, there are two solution approaches, fully-coupled and sequential methods. In this study, we take the sequential method to make use of existing individual simulators and minimize coding efforts. We employ the fixed stress split due to its superior behavior in stability and convergence even for strongly coupled problems.

The main body of this study starts with a field application of CO_2 injection into a pilot-scale site for geological storage to investigate fault reactivation and slip. We develop a simulation tool by coupling a multiphase flow simulator with an existing mechanics simulator to model the fault slip and estimate the magnitude of seismic events dynamically with injection-induced pressurization and fault strength.

In the second part of the study, an attempt is made to supplement the capabilities of coupled flow and geomechanics simulation by using it to develop a surrogate model using a U-Net based Convolutional Neural Network which can predict the distribution of displacement, pressure and, saturation fields based on permeability, injection rate, and time inputs.

In the third part of this thesis, how two-way coupled flow and geomechanics can play a critical role in the analysis of wellbore instability during production from methane hydrate-bearing sediments is studied. With ~~field~~ data from the PBU-L106 site in Alaska and UBGH2-6 site in Ulleung Basin, South Korea, axial stress profiles along the wellbore under depressurization-

based gas production are investigated with sensitivity analysis with several sets of properties of interface elements between wellbore and formation to ensure safe and continuous production.

In the last chapter, we propose a numerically stable sequential method for all-way coupled geomechanics and flow simulation in discrete fractured systems. First, we study numerical stability and accuracy for a numerically stable sequential approach between multiphase flow and hydraulic fracturing geomechanics. Furthermore, we investigate the physical responses from multiphase flow on fracture propagation numerically, considering both fluid compressibility and the fracture volume change induced by poromechanics.

The topics covered in this thesis help show how coupled flow and geomechanics is useful in various subsurface applications especially in predicting fluid flow induced mechanical failure.

DEDICATION

To my late mother, my father, and my brother.

CONTRIBUTORS AND FUNDING SOURCES

Contributors

This work was supported by a dissertation committee consisting of Dr. Jihoon Kim, Dr. John Killough, Dr. Eduardo Gildin of the Harold Vance Department of Petroleum Engineering and Dr. Yalchin Efendiev of the Department of Mathematics.

The data used in Chapter 3 was provided by the basic research project of the Geologic CO_2 Storage Group in Korea Institute of Geoscience and Mineral Resources (KIGAM) and the KCRC project supported by the Korea Ministry of Science, ICT & Future Planning. The analyses were published in part article in the 53rd US Rock Mechanics/Geomechanics Symposium in 2019.

The data analyzed for Chapter 5 was provided by Lawrence Berkeley National Laboratory (LBNL) and Korea Institute of Geoscience and Mineral Resources (KIGAM). The analyses were published in part in the report issued in 2020 by the U.S. Department of Energy with issue number DOE-TAMU-FE0028973–1.

All other work conducted for the dissertation was completed by the student independently.

Funding Sources

This graduate study was supported in part by a research assistantship from the Texas A&M Engineering Experiment Station and the Department of Petroleum Engineering at Texas A&M University. This study was also supported by Larry A. Cress '76 Faculty Fellowship from Texas A&M University; the U.S. Department of Energy (Award No. DE-FE0028973),

Methane Hydrate Program.

The contents and results of this work are solely the responsibility of the student and his advisory committee, and do not necessarily represent the official views of the funding sources cited above.

TABLE OF CONTENTS

Page

LIST OF FIGURES

FIGURE Page

LIST OF TABLES

TABLE Page

1. INTRODUCTION AND LITERATURE REVIEW

Numerical simulation has been used in earth sciences for modeling changing hydraulic properties in porous media for producing hydrocarbons, water, or other fluids. There has been growing focus on exploiting more complicated earth systems such as gas hydrates for unconventional gas production, fluid injection (gas/water/nuclear wastes) into underground systems for various purposes such as waste water disposal, safe storage of radioactive waste, CO_2 sequestration, geothermal energy production or even hydrocarbon production from multi-fractured horizontal wells [2] [7] [8] [9] [10] [11] [12] [13] [14]. The advent of these technologies and techniques has brought the necessity of being capable to simulate not only the hydraulic processes associated with flow but also modeling the accompanying geomechanical changes simultaneously. Thus, there has been a renewed push in both the industrial and academic research on applying coupled fluid flow and geomechanics techniques for the detailed characterization of these processes.

The idea conveyed in the preceding lines can be further elaborated through very common examples:

- Reservoirs are often characterized by faults and fractures. There have been seismic events recorded due to anthropogenic activities in numerous U.S. states more recently in Oklahoma, Colorado, or even in injection sites internationally, more recently in South Korea. Most of these occurrences have been results of fault reactivation and slip where the geomechanical complications accompanying these activities were often not adequately accounted for.

- Methane hydrates are widely accepted as an untapped energy resource of the future. They are solid structures that when produced undergo depressurization, which is a process accompanied by massive dissociation into gas that can collapse not only the structure through which it is produced but also the overlying sediments. The idea of keeping the well structure and adjacent area safe while draining such systems makes consideration of geomechanics important.

- Numerical simulation of hydraulic fracturing operations has considerably improved over time by the use of up-to-date techniques incorporating field data such as pumping proppants, fluid, and its rate. However, there is still a numerical stability issue with two-way coupled flow-discrete fracture geomechanics with sequential methods.

The crux of this thesis is therefore to present the power of utilizing coupled flow and geomechanics modeling through topics studying fault reactivation and slip, induced seismicity, wellbore stability, and fracture propagation. Most of the topics covered in this thesis also include investigations carried on field-level applications to show the scalability of proposed methods on a larger and more relevant scale. For the first part, we conduct a detailed site-specific study of fault reactivation and slip during CO_2 sequestration operations in South Korea. The results from this study underline the importance of characterizing fault properties and modeling various scenarios during injection to prevent occurrences of fault rupture or even estimate the magnitude of seismic events that may occur. The second part addresses the issue of wellbore instability in Methane hydrate deposits, given these issues are critical to feasibly produce gas and protect the surrounding zones from contamination due to unexpected occurrences. The results show how during depressurization induced production, vertical displacement along hy-

drate zones makes careful consideration of wellbore stability essential using coupled flow and geomechanics simulation. In the last part, we address why it is important to monitor the geomechanical properties (like fracture volume change) to simulate fracture propagation with the addition of an appropriate stabilization term

1.1 Literature review

1.1.1 Fault reactivation and slip in geological CO_2 sequestration

In this chapter, we cover the topic of CO_2 sequestration activity related to induced seismicity due to reactivation of faults and their slip. With the increasing focus on climate change mitigation technologies due to rising global temperatures brought about by anthropogenic greenhouse gas emissions due to fossil fuel use (IPCC 2018), the importance of CO_2 sequestration technologies has increased. Carbon captured from point sources and stored (CCS) in deep subsurface geologic formations (e.g., saline aquifers, depleted hydrocarbon reservoirs, coal beds) has been suggested as a promising method for significantly reducing the emission of greenhouse gases into the atmosphere [15] [16] [17]. CCS technologies are in fact a very effective and environmental-friendly way to reduce atmospheric CO_2 concentrations. Under the aegis of this technique, a large volume of super-critical CO_2 (more than 1 Mton/year or more) is injected at a commercial scale into a target formation (laterals extending greater than 10 km in radius) for a long period of time (a few years to decades) [18]. Injecting such a large volume of CO_2 is often accompanied by an increase in reservoir pressure which causes changes in stress and may even lead to deformation in the reservoir and the surrounding formations [19]. These injection-induced changes can give rise to several geomechanical

risks: hydro-fracturing of the seal rock, surface ground uplift, reactivation of faults within or bounding the reservoir, shear failure at the reservoir-cap rock interface, and casing damage, etc. [20] [19]. Among geomechanical risks, surface ground uplift and fault reactivation are big concerns with regard to induced seismicity. Pressure build-up in the storage formation results in an expansion of the reservoir, causing surface ground uplift or heave in opposite direction to surface subsidence which is caused by reservoir compaction due to the extraction of underground fluids [21] [13] [22] [23] [24] [25]. The rate of surface ground uplift from subsurface fluid injection depends on the injection rate, material properties of the reservoir and overburdens, and in-situ stress field. At the CO_2 storage site of the In Salah project in Algeria, a surface-ground uplift rate of 5 mm/year has been observed around the sites of the CO_2 injection wells [21] [13] [22]. When fractures or faults exist in a CO_2 storage site, pressure build-up in the formations may lead to shear-slip along the pre-existing discontinuities, potentially enhancing the fault permeability and leakage of stored CO_2 along the fault [26] [27] [11]. Shear-induced permeability enhancement in fractures has been observed in various scales ranging from laboratory tests to field measurements. Laboratory studies on bare fractured rocks (rock-on-rock) without infill materials (e.g., clay) between them have shown that a shear displacement of a few millimeters along the fracture plane can significantly increase the fracture permeability due to shear dilation [28] [29] [30]. In the field, temperature surveys along boreholes drilled through highly fractured and faulted crystalline rocks have shown that the permeability of active (or critically stressed) faults and fractures is much higher than those of non-critically stressed ones, which are typically not optimally oriented relative to the in-situ stress field (Barton, 1995). Natural analogue studies show gas springs and travertines

along fault traces at the surface, which are evidence of possible long-term leakage of CO_2 along faults with a relatively high hydraulic conductivity [31] [32]. In addition, gas concentration anomalies (mainly radon and CO_2) have been reported in areas in close proximity to the outcrops of active faults [33] [34] [35]. Fault reactivation occurs in either aseismic- or seismic-slip modes depending on the fault internal structure and material composition [36]. In the case of seismic slip, it induces micro-seismicity and occasionally triggers 'felt' seismic events (M_w > 3.0). The latter or specifically earthquakes induced by massive fluid injection at depth are well-documented [37] [38] [7] [39] [27] [40] [41] [42] [43] [25] [44] [45]. Injection-induced seismicity was first documented in the 1960s at the Rocky Mountain Arsenal, where a 3.6 km borehole was drilled to dispose of wastewater containing hazardous chemicals. Earthquakes occurred several months after the injection started, and a total of 35 earthquakes having M_w > 3.0 were recorded during the injection period from 1962 to 1967. Even after injection operations ceased, earthquakes were observed for several more decades, albeit at a reduced rate. Inducing notable seismicity can significantly impact the integrity of subsurface CO_2 repository systems which puts the viability of the injection projects at risk [10] [44] [45]. A recent well-known example is the shut-down of the geothermal project in Pohang, Korea after the occurrence of an M_w = 5.4 earthquake [44] [45] which caused injuries and substantial structural damage to buildings in the epicenter area. As with any subsurface injection project, the long-term integrity of the storage site must be ascertained with a good degree of accuracy and confidence. This helps to avoid the aforementioned geomechanical hazards and to secure a stable and permanent CO_2 storage in deep geologic formations. It is therefore critical to identify potential geomechanical risks during the stage of site characterization, this involves

analyzing the hydro-geomechanical effects in order to define the conditions (e.g., maximum sustainable injection pressure) for ensuring safe and continuous operation. In this dissertation, as an effort to define the allowable injection pressure before injection, we have estimated the maximum sustainable injection pressure relevant to the reactivation of a fault in a pilot-scale CO_2 storage site. For the estimations, we have employed analytical and numerical methods. We have then compared the results and to draw conclusions and make recommendations.

1.1.2 Application of Deep-Learning based Surrogate Models.

Though the application of the in-house flow and geomechanics simulator was affirmed with its use in studying a pilot-scale CO_2 geological storage operation, the idea of the work done throughout this dissertation has been to push the boundaries of the capabilities of coupled flow and geomechanics simulation. With the advances in computational power and research around deep-learning algorithms capable of learning complex relationships between parameters at various scales, there has been an increasing body of work looking into applications in various spheres especially in the field of surrogate model development in oil and gas and allied fields that involve studying flow in geological media [46] [47] [48][49]. Specifically, there is a growing amount of work around the use of Data-driven and physics-based modeling approaches that can take varying input parameters to predict the temporal variation of dynamic properties in various geological domains. Kim et al., [50] implemented a CNN-based proxy model to optimize well locations and NPV calculations under geological uncertainty for different reservoir conditions. Jin et al. [51] presented a variational U-Net based method to quantify uncertainty during reservoir simulation. Given the sheer power of these methods to complement the advances made in numerical simulations while also saving on the immense

amount of time often spent waiting on simulation results, invariably point to the need to adopt them more widely. Tang et al. [47] talks of a deep-learning-based surrogate model using a method called 3D recurrent residual U-Net, which uses convolutional and recurrent neural networks to predict flow responses for new geo-models. Wen et al. [52] develops a deep learning model capable of supplanting computationally intensive numerical simulators for tasks such as predicting injection performance during CO_2 storage operations. However, a close look at all the literature published in the area of case-specific surrogate model development shows that most of these papers have focused on aspects that supplant the use of flow simulators. The scope of use of deep learning methods in helping develop models that mirror coupled flow and geomechanics simulation results remains practically unexplored. This is a huge void that has immense promise given the computationally intensive operations that these simulations require. With appropriate training and validation, surrogate models can help complement the power of flow and geomechanics simulations given their importance in studying areas where flow-based processes have the power to alter system mechanical properties to disastrous effects. For this purpose, we present a proof of concept wherein we use a 3D U-Net based convolutional neural network to train on various geo-model realizations to predict displacement, saturation, and pressure field for a CO_2 storage operation. The developed model shows promising results and shows how this method with a larger training sample (or real-world data of the appropriate size) can also be extended for predicting other complicated results obtained from flow and geomechanics simulations like fault activation, slip, seismic magnitudes, etc.

1.1.3 Well stability in Methane hydrate deposits

Gas Hydrates are ice-like crystalline minerals that are formed when gases with lower molecular weight e.g., methane, ethane, propane, or carbon dioxide combine with water under certain conditions of pressure and temperature, outside of which these otherwise would have been separate phases. These guest molecules are hydrogen-bonded with water in the lattice spaces which without the support of these trapped molecules would collapse. Hydrates occur in nature in two distinctly unique conditions when the necessary physical conditions exist: beneath the permafrost above the Arctic Circle and in deep oceanic sediments. It is the deposits located in the latter that have garnered the most interest from researchers worldwide. Data from studies conducted suggest that gas hydrate resources occur in huge amounts and include more than 700 trillion cubic feet (tcf) of trapped methane in formations that can often be several hundred meters thick. In fact, data gleaned from research in this arena suggests that there are more than 230 gas hydrate discoveries throughout the world accounting for huge amounts of untapped gas resources. Among the various lattice structures possible for hydrates/clathrates, most natural gas hydrates assume "Structure I", with methane as the trapped gas.

The studies conducted for this portion of the work focuses on two sites, the importance of each is enlisted below:

- Ulleung Basin, South Korea. South Korea is dependent on importing huge amounts of gases for the use of its citizens. In fact, data from 2019 show that it is the third-largest importer of Liquefied Natural Gas (LNG) and therefore its methane hydrate de-

posits are an important future energy resource for the country. Expeditions investigating the hydrate reserves and their characteristics in the Ulleung Basin (UBGH1, 2007 and UBGH2, 2010) located in the East sea of South Korea showed that the deposits here range from 4.4×10^6 to 9.2×10^9 m^3. [53] The deposits in this location are situated in between interspersed layers of sand and mud with an approximate thickness of 20 m [54].

- PBU L-106 site, North Slope, Alaska Gas Hydrates have been known to exist in the Alaskan North Slope since their first direct confirmation from a single well located in the Prudhoe Bay Field [5][55]. In fact, the gas hydrate resource in place within the Eileen Gas Hydrate Accumulation is estimated to be about 1.2 tcf [56] which is more than twice the volume of conventional gas in the Prudhoe Bay field. The deposits investigated in this case are bounded at the top and bottom by shale and characterized by high permeabilities, porosity, and hydrate saturation, as well as hydrostatic pressure distribution [57].

There have been several methodologies that have been suggested for extracting natural gas from hydrate-bearing sediment (HBS) [58] [59]. The commonly suggested ones involve some form of thermal or inhibitor injection, depressurization, CO_2/CH_4 exchange or a combination of all these techniques. The major aim of all these techniques is to bring about hydrate dissociation from its ice-like structure to a gaseous or liquid state by increasing its temperature or reducing its pressure. Of all these methods, depressurization is widely accepted as the most promising technique and has been applied as a production technique in various hydrate production field test sites (e.g., Malik site in 2002, Ignik Sikumi Field trials in 2012, Nankai

Trough in 2013 among others). Since the process of depressurization breaks the solid lattice structure of hydrates into gas/liquids, significant ground settlement occurs due to these phase changes as it invariably reduces the strength and stiffness of the hydrates which causes the effective stresses around the HBS to increase. In fact, technical problems associated with the mechanisms mentioned above have also been observed across field tests for gas hydrate production. Numerical analysis makes it possible to look at various scenarios that help pre-empt complications and therefore ensure not only the productivity of the gas hydrates from these sediments but also ensure stability of production facilities during field tests. Thus, detailed Thermal-hydraulic-mechanical (THM) coupled numerical analysis to simulate gas hydrate production mechanisms is necessary before any field-level operation. TOUGH+Hydrate, HydrateResSim, MH21, and STOMP-HYD [60] are some commonly used numerically coupled simulators based on kinetic and equilibrium model designed for such applications. Other simulators include the THM coupled simulator using FLAC3D [61]. The results from numerical analyses, e.g., the potential for energy recovery and geological hazards prevention is affected by the input parameters (e.g., boundary condition, intrinsic hydrate reaction rate, intrinsic permeability, initial hydrate saturation, overall heat conductivity, wellbore heating temperature, bottom hole pressure, etc.) and constitutive models (e.g., permeability model, stiffness model, and heat transfer model). There have been numerous numerical studies on the efficiency and productivity of gas hydrates in various systems. However, notwithstanding its importance to field production very few studies have investigated or even considered stability analyses in hydrate-bearing sediments or the wellbore.

Elaborating more on the mechanisms involved in depressurization induced production in

HBS, pressure reduction causes the evolution of frictional forces at the interface between the production wellbore and the soil layer due to the difference in the stiffness of materials which in turn induces axial stresses on the production wellbore. This underlies the importance of analyses like soil–structure interaction analysis for understanding the stability of the wellbore and hydrate-bearing sediments. To simulate interfacial stress behavior in numerical analyses concepts of shear and normal coupling stiffness or interfacial stiffness based on the linear Coulomb shear strength criterion have been widely used [62]. Interface models have been used to investigate the non-linear behavior of the soil-structure and the displacement behavior [63]. Rutqvist et al. [64] performed investigations on the geomechanical responses relating to wellbore stability during methane production using numerical analyses (e.g., pressure, temperature, hydrate saturation, and volumetric strain). It is essential to consider confining stress variations according to depressurization while conducting analyses on stability. This dissertation attempts to fill this lacuna through the work presented in the next few chapters.

1.1.4 Numerical stability for fracture propagation

Numerical methods of hydraulic fracture propagation have been studied in order to accurately model behavior of the created fractures in reservoirs in order to optimize production of gas as well as to reduce environmental impacts. For example, the discrete element method takes intact rock and fractures separately and performs numerical simulations of fracture propagation, splitting nodes followed by creating a new fracture, this method however may require high computational cost due to remeshing [65] [66]. The extended finite element method is widely used in modeling crack propagation in fracture mechanics. They are based on the continuum approach with discontinuous interpolation functions that can allow discontinuous

displacement, not requiring the remeshing procedure [67] [68]. The displacement discontinuity method has also frequently been applied in modeling the fracture behavior in fractured reservoir systems [69] [70] [71]. In particular, this method is widely used for solving fractured thermo-poro-elastic problems in an enhanced geothermal system, which contains a discrete fracture network in a porous medium. The phase-field approach has recently been applied to hydraulic fracturing simulation [72] [73]. The hydraulic fracture can propagate in an arbitrary direction with the adaptive mesh [74]. In addition to hydraulic fracturing simulation, geophysical methods often monitor the spatial-temporal changes of fractured volume and fluid flow. For example, fracturing results in microearthquake events, provide general information of locations of fracturing events. High ratios of compressional and shear wave velocity are often associated with high porosity and fluid zones in fracture networks [75]. Electromagnetic geophysical methods can also delineate fluid flow in fractured zones where there is often a high contrast between injected electrically-conductive fluids and resistive shale formation [76] [77]. Yet, rigorous simulation of fracture propagation coupled to multiphase flow that accounts for both fluid compressibility and dynamic change of the fracture volume has not been studied in depth. Geertsma and de Klerk [78] and Detournay [79] have analytically investigated the fracture tip behavior considering the dynamic change of the fracture volume, but not fluid compressibility, which have shown some vacuum area at the fracture tip [80]. This implies that a dry zone is possible near the fracture tip in multiphase flow, i.e., a high gas saturated zone between the fracture tip and the front of the injected water. Still, the analytical approach takes some assumptions such as incompressible flow of single-phase, and it has limitation to capture strongly coupled geomechanics and multiphase flow, typically nonlinear. For exam-

ple, Raterman et al. [81] analyzed samples of the stimulated rock volume from an Eagle Ford field. The results show that most of the fractures are dry, not saturated with proppants. The absence of proppants implies that the idealized hydraulic fracturing models cannot explain this behavior. Furthermore, the effects of not only the fracture volume but also fluid compressibility become important when compressible fluid such as gas is used as a fracturing fluid. Kim and Moridis [82] took the concept for single vertical fracture propagation with coupled multiphase flow and geomechanics and simulated a dry zone at the fracture tip while tensile strength was employed for hydraulic fracturing in relatively large-scale simulation. But using rock toughness rather than tensile strength might be more consistent with fracture mechanics and appropriate for accurately modeling the physics near the fracture tips. The aforementioned studies of phase field geomechanics considered fluid compressibility in the flow problem for hydraulic fracturing, but not fully in the change of the fracture volume. Hence, more rigorous simulation in the coupled physical processes including multiphase flow is required. There are two approaches to solve the coupled problems: Fully implicit and sequential implicit methods. The fully implicit method solves the coupled systems simultaneously, and its main advantage is unconditional stability [83]. But it may require huge computational cost in solving a large system of coupled linear equations as well as much effort in developing a unified code. On the other hand, the sequential implicit method solves the coupled problems sequentially, facilitating using the individual existing codes of the sub-problems by constructing an interface code only. Thus, it can reduce not only the coding effort significantly but also computational cost because of a smaller linear system. However, the sequential implicit method may not provide numerical stability. In particular, numerical stability for hydraulic fracturing simu-

lation has not sufficiently been discussed. Even though stability of the sequential methods for poromechanics has been studied substantially, their stability for the coupled flow-discrete fracture geomechanics problems is still unclear because the fractures are treated as boundaries in geomechanics. In the conventional poromechanics problems, the undrained and fixed stress methods are unconditionally stable [84] [85]. Esfahani and Gracie [86] applied the undrained sequential method to the hydraulic fracturing simulation. However, from Kim et al. [87], the undrained method can be less accurate for strongly coupled flow and geomechanics and even non-convergent for incompressible fluid flow. On the other hand, the fixed-stress method provides high accuracy for the strongly coupled problems including incompressible fluid flow. The fixed-stress method solves the flow problem first, where the stabilization term is estimated from the drained bulk modulus. However, unlike the typical poromechanics problems, the drained bulk modulus of the fractures is not explicitly defined for the opening mode of the hydraulically fractured systems. Just as determination of the bulk modulus is a key factor in the fixed stress method of the poromechanics problems, it is important to estimate the fracture volume change and to determine an appropriate stabilization term effectively when solving the flow problem within the fracture.

1.2 Focus and novelty of dissertation

Through the topics covered in this dissertation, we seek to bring forward the benefits and importance of coupling geomechanics and multiphase fluid flow. Simultaneously accounting for failure phenomena ensures that many geomechanical aspects that affect well productivity are not neglected or simplified. Ranging from their applications in burgeoning technologies and hydrocarbon extraction techniques like Carbon Capture and Storage (CCS) and Methane

hydrates to topics covering their utility in understanding fracture propagation, the work done for this dissertation continuously tries to reaffirm the need for the wider use of these study techniques. The use of coupled flow and geomechanics simulation is often discounted on the basis of its numerical complications, computation time, etc. However, with improving simulation efficiency and better mathematical models, the work done in this dissertation shows the power of using these numerical methods of simulation and the pitfalls of not taking them into consideration. Moreover, the code-base presented in this work has wider applications in a wide range of areas involving the production or injection fluids in porous systems and the accompanying processes thereof.

The chapter on geomechanical responses in the CO_2 storage site in Korea can help avoid risky situations involving tension/shear failure in any geological location. The results from this study have wider application not only for CO_2 storage but also the study of geothermal wells where often injection of water is involved into geologic systems or even water disposal wells for unconventionals. The studies conducted for well stability in Methane hydrate deposits clearly demonstrate how processes like sand production, capillarity, secondary hydrate formation, etc. require the use of coupled flow and geomechanics simulation to adequately understand their mechanisms and effects. The solutions to the well stability problem for gas hydrate production have applications for enlisting the phenomena that need to be considered while not only drilling but also producing from such a system. The chapter on numerical study for fracture propagation adds to the body of work that has been done relating to the simulation of fracture propagation in a bi-wing fractured system in unconventional formations.

The findings presented in this study, therefore, cover areas that not only add to limited

research done in the application areas but also make a strong case for integrated simulation of flow and geomechanical processes while considering complicated physics in porous systems.

2. MATHEMATICAL FORMULATION

2.1 Governing Equation

The governing equation for the flow and geomechanics is described separately for the sequential method. The governing equation for multi-component fluid flow is derived from the mass balance equation as follows [88],

$$\frac{dm^k}{dt} + \mathrm{Div}\, \boldsymbol{w}^k = (\rho f)^k, \tag{2.1}$$

where the superscript k indicates the fluid component, m^k, $\boldsymbol{w}^k$, and f^k are the fluid mass of the component k, and its mass flux, and volumetric source and sink term on the volume of the domain Ω with the boundary surface Γ, respectively.

Under equilibrium, the mass accumulation term for component k is given by

$$m^k = \phi \sum_{J=A,G,S} S_J \rho_J X_J^k, \tag{2.2}$$

where ϕ is the true porosity which means the ratio of the pore volume to the bulk volume in the deformed configuration. S_J and ρ_J are saturation and density of phase J, respectively. And X_J^k is the mass fraction of component k in phase J. For the project involving geological storage of CO_2, we consider only two components, H_2O and CO_2 among three phases (aqueous, gaseous, and solid). For the wellbore stability analysis in methane hydrate reservoir, two components, H_2O and CH_4 distributed among four phases (aqueous, gaseous, hydrate, and

ice) are taken into account since hydrate is one of the states with H_2O and CH_4.

The mass flux term $\boldsymbol{w}^k$ is limited to the mobile phases, aqueous and gaseous and is given by

$$\boldsymbol{w}^k = \sum_{J=A,G} \boldsymbol{w}_J^k, \tag{2.3}$$

For aqueous phase, the phase flux is described by Darcy's law as follows

$$\boldsymbol{w}_A^k = \rho_A X_A^k \boldsymbol{v}_A = -\rho_A X_A^k \frac{k_{rA}}{\mu_A} \mathbf{k}(\mathbf{Grad}\, P_A - \rho_A \boldsymbol{g}), \tag{2.4}$$

where $\boldsymbol{v}_J$ is the volumetric flux of phase J. $\mathbf{k}$ is the absolute permeability tensor. k_{rJ}, μ_J, and P_J are the relative permeability, viscosity, and fluid pressure fo the phase J, respectively. $\mathbf{Grad}$ is the gradient operator and $\boldsymbol{g}$ is the gravity vector.

The mass flux of the gaseous phase incorporates convective and diffusive mass flow of component k as

$$\boldsymbol{w}^k{}_G = -\rho_G X_G^k \left(1 + \frac{K_k}{P_G}\right) \mathbf{k} \frac{k_{rG}}{\mu_G} (\mathbf{Grad}\, P_G - \rho_G \boldsymbol{g}) + \boldsymbol{J}_{\boldsymbol{G}}^{\boldsymbol{k}}, \tag{2.5}$$

where K_k is the Klinkenberg factor for gas slippage effect. The term $\boldsymbol{J}_{\boldsymbol{G}}^{\boldsymbol{k}}$ is the diffusive mass flux of component k in the gaseous phase and is described by

$$\boldsymbol{J}_{\boldsymbol{G}}^{\boldsymbol{k}} = -\phi S_G \tau_G \mathbf{D}_G^k \rho_G\, \mathbf{Grad}\, X_G^k, \tag{2.6}$$

where $\mathbf{D}_G^k$ is the hydrodynamic dispersion tensor, and τ_G is gas tortuosity computed from the $Milington\ and\ Quirk$ model as $\tau_G = \phi^{1/3} {S_G}^{7/3}$

We adopt the poroelasticity and poroelastoplasticity theories [89] with assumptions of small deformation (i.e., infinitesimal transformations) and no stress-dependence of flow properties. The governing equation for geomechanics can be written as

$$\mathrm{Div}\,\boldsymbol{\sigma} + \rho_b \boldsymbol{g} = \mathbf{0}, \tag{2.7}$$

where $\mathrm{Div}(\cdot)$ is the divergence operator, $\boldsymbol{\sigma}$ is the Cauchy total stress tensor, ρ_b is the bulk density which can be expressed as $\rho_b = \phi\rho_f + (1-\phi)\rho_s$ where ρ_f is fluid density and ρ_s is the density of the solid phase. For the sign convention in this study, tensile stress is positive.

2.2 Constitutive Relations between Flow and Geomechanics

Fluid flow and geomechanics are coupled through the constitutive equation by Biot's theory [89, 90, 91, 92]. We can express the total stress σ and fluid mass m_J with functions of the total strain ε and fluid pressure p_J as

$$\delta\sigma = \mathbf{C}_{dr} : \delta\boldsymbol{\varepsilon} - b_J \delta p_J \mathbf{1}, \tag{2.8}$$

$$\left(\frac{\delta m}{\rho}\right)_K = b_J \delta\varepsilon_v + \frac{1}{M}\delta p_J, \tag{2.9}$$

where $\mathbf{C}_{dr}$ is the drained elasticity moduli, $\mathbf{1}$ is the rank-2 identity tensor. b is the Biot coefficient ($b_J = bS_J$) and M is the Biot moduli matrix. J and k represent two fluid phases, aqueous and gaseous phase. For a two-phase and two-component fluid system, M^{-1} can be

found in [93] and written as

$$
\begin{aligned}
M^{-1} = N_{JK} &= \begin{bmatrix} N_{gg} & N_{gw} \\ N_{wg} & N_{ww} \end{bmatrix} \\
&= \begin{bmatrix} \phi S_g c_g - \phi \frac{dS_w}{p_{cg}} + S_g \frac{b-\phi}{K_s} S_g & \phi \frac{dS_w}{dp_c g} + S_g \frac{b-\phi}{K_s} S_w \\ \phi \frac{dS_w}{p_{cg}} + S_w \frac{b-\phi}{K_s} S_g & \phi S_w c_w - \phi \frac{dS_w}{p_{cg}} + S_w \frac{b-\phi}{K_s} S_w \end{bmatrix}
\end{aligned}
\tag{2.10}
$$

where c_J and Pc are the compressibility of the fluid phase J and the capillary pressure, respectively. K_s is the intrinsic solid grain bulk modulus. Double indices (e.g., JK) indicate the summation according to Einstein notation. Another well-known example of Einstein notation is $\boldsymbol{\sigma}_{ij}$, stress tensor.

Using Equation 2.9, Equation 2.1 (governing equation of fluid flow) can be expressed in terms of pressure and volumetric strain as

$$
\frac{1}{M}\frac{\partial p}{\partial t} + b\frac{\partial \varepsilon_v}{\partial t} + \operatorname{Div} \boldsymbol{v} = f, \tag{2.11}
$$

With bulk volume variation and pore volume variation, we can derive the porosity function.

$$
\begin{aligned}
\delta\Phi &= \left(\frac{b-\Phi}{K_s}\right) \sum_{J=A,G} S_J \delta p_J + b\delta\varepsilon_v, \\
&= \left(\frac{b^2}{K_{dr}} + \frac{b-\Phi}{K_s}\right) \sum_{J=A,G} S_J \delta p_J - b\delta\sigma_v,
\end{aligned}
\tag{2.12}
$$

where Φ is Lagrange's porosity defined as the ratio of the pore volume in the deformed configuration to initial configuration of the bulk volume. We can also consider the true porosity as

Lagrange's porosity in Equation 2.10 since it is also symmetric and positively definite, which means that the difference is negligible.

2.3 Numerical Discretization

2.3.1 Porosity Updating for Reservoir Domain

Two-way coupling method with the fixed-stress sequential manner can take a solution strategy by fixing one state variable to solve the two sub-problems in a sequence. Specifically, the total stress is kept constant while solving the fluid flow problem as follows

$$\begin{bmatrix} \boldsymbol{u}^n \\ \boldsymbol{p}_J^n \end{bmatrix} \xrightarrow{\mathcal{A}_{ss}^p} \begin{bmatrix} \boldsymbol{u}^* \\ \boldsymbol{p}_J^{n+1} \end{bmatrix} \xrightarrow{\mathcal{A}_{ss}^u} \begin{bmatrix} \boldsymbol{u}^{n+1} \\ \boldsymbol{p}_J^{n+1} \end{bmatrix}, \tag{2.13}$$

$$\text{where} \quad \begin{cases} \mathcal{A}_{ss}^p : \dot{m} + \operatorname{Div} \boldsymbol{w} = \rho_{f,0} f,\ \delta\dot{\sigma} = 0, \\ \mathcal{A}_{ss}^u : \operatorname{Div} \boldsymbol{\sigma} + \rho_b \boldsymbol{g} = \mathbf{0},\ p_J : \text{ prescribed}. \end{cases}$$

where $\mathcal{A}_{ss}^p$ and $\mathcal{A}_{ss}^u$ stand for the fluid flow and geomechanics steps. u is an intermediate displacement.

During the $\mathcal{A}_{ss}^p$ step with $\delta\dot{\sigma} = 0$, Equation 2.12 under the backward Euler method can be restated as

$$\Phi^{n+1} - \Phi^n = \left(\frac{b^2}{K_{dr}} + \frac{b-\phi}{K_s} \right) \sum_{J=A,G} S_{J,e}^{n+1} (p_J^{n+1} - p_J^n) - \Delta\Phi \tag{2.14}$$

$$\text{where} \quad S_{J,e} = \frac{S_J}{\sum\limits_{J=A,G} S_J},$$

$$\Delta\Phi = \frac{b^2}{K_{dr}} \sum_{J=A,G} S^n_{J,e}(p^n_J - p^{n-1}_J) - b(\varepsilon^n_v - \varepsilon^{n-1}_v),$$

where $\Delta\Phi$ is the porosity-correction term, which is the main difference from the one-way coupling process. σ_v is the volumetric mean total stress. n denotes the temporal point in the discretized time domain. The term $\frac{b^2}{K_{dr}} + \frac{b-\phi}{K_s}$ represents the pore compressibility c_p used in one-way coupling of fluid flow and geomechanics. The two-way coupling process for tightly coupled problem considers the correction term of the porosity $\Delta\Phi$ calculated by changes in geomechanical properties.

2.3.2 Flow within Fracture and Stabilization

In numerical simulation of fracture propagation, we divide the domain, reservoir formation Ω_m and fracture Ω_f. Equation 2.11 can be considered as fluid flow problem in matrix domain Ω_m. The mass variation of the fluid within the fracture volume becomes $\delta m_f = \delta(\rho_f w_f dA_f)$, where w_f is the fracture aperture and dA_f is the surface area of the fracture domain Ω_f. With Equation 2.1 and Equation 2.9, we can write the fluid flow problem in fracture domain Ω_f without the source and sink term as follows

$$c_f \frac{\partial p}{\partial t} + \frac{1}{w_f}\frac{\partial w_f}{\partial t} + \text{Div}\, v = 0, \tag{2.15}$$

where c_f is fluid compressibility and $k_p = w_f^2/12$

By comparing Equation 2.11 with Equation 2.15, we can utilize the same approach used in

porosity updating by taking Biot moduli, coefficient, and volumetric strain changes as $1/M = c_f$, $b = 1$, and $\delta\varepsilon_v = \delta \log w_f$, respectively. The changes in volume within the fracture while propagating the domain is relatively large. For the large deformations,

$$\delta\varepsilon_v = \delta \log J, \tag{2.16}$$
$$\text{where} \quad J = \det \boldsymbol{F} \quad \text{and} \quad \boldsymbol{F} = \mathbf{1} + \frac{\partial \boldsymbol{u}}{\partial \boldsymbol{X}} \left(F_{ij} = \delta_{ij} + \frac{\partial u_j}{\partial X_j} \right),$$

where $\boldsymbol{F}$ and $\boldsymbol{X}$ indicate the formation gradient and the coordinates in the initial configuration. The subscripts i and j denote the coordinates, and δ_{ij} is the Kronecker delta function. Thus, the fracture volume change is consistent with Equation 2.16.

Equation 2.15 multiplied by the aperture can be restated without gravity as follows

$$w_f c_f \frac{\partial p}{\partial t} + \frac{\partial w_f}{\partial t} + \frac{\partial q_f}{\partial x} = 0, \quad \text{where} \quad q_f = -\frac{w_f^3}{12\mu_f} \frac{\partial p}{\partial x}, \tag{2.17}$$

The flow capacity in the fracture strongly depends on the fracture opening w_f, described by the cubic law [94] [95]. With an assumption of incompressible fluid, the lubrication equation can be obtained from Equation 2.17 which is typically used in analytical solutions.

$$\frac{\partial w_f}{\partial t} + \frac{\partial q_f}{\partial x} = 0, \tag{2.18}$$

Firstly, we can rewrite the Equation 2.9 with fixed stress method separately in reservoir

matrix domain as follows

$$\left(\frac{\delta m}{\rho}\right)_J = \left(N_{JK} + \frac{b^2 S_J S_K}{K_{dr}}\right)\delta p_K + \frac{bS_J}{K_{dr}}\delta\sigma_v, \tag{2.19}$$
$$\text{where} \quad \frac{bS_J}{K_{dr}}\delta\sigma_v = -\frac{b^2 S_J S_K}{K_{dr}}\delta p_K + b_J \delta\varepsilon_v,$$

And Equation 2.19 can be discretized as

$$\left(\frac{m^{n+1,k+1} - m^n}{\rho}\right)_J = \left(N_{JK} + \frac{b^2 S_J S_K}{K_{dr}}\right)(p_K^{n+1,k+1} - p_K^n) + \frac{bS_J}{K_{dr}}(\sigma_v^{n+1,k} - \sigma_v^n), \tag{2.20}$$
$$\text{where} \quad \frac{bS_J}{K_{dr}}(\sigma_v^{n+1,k} - \sigma_v^n) = -\frac{b^2 S_J S_K}{K_{dr}}(p_K^{n+1,k} - p_K^n) + b_J(\varepsilon_v^{n+1,k} - \varepsilon_v^n),$$

where the superscript n and k indicate the discrete time level and iteration level, respectively.

To solve the flow problem within the fracture, it is necessary to modify K_{dr} used for the flow problem because deformability of the fracture is different from that of the reservoir (intrinsic rock). Let K_{dr}^{fr} denote an apparent fracture stiffness, which represents deformability of the fracture. Let us estimate an appropriate K_{dr}^{fr} to determine the stabilization term. When the pressure in the fracture is constant, the fracture aperture can analytically be obtained for bi-wing fracture geometry as follows

$$w_f = \frac{2(1-\nu)L_f(p - \sigma_H)}{G_{dr}}\sqrt{1-x^2}, \tag{2.21}$$

$$\Rightarrow \delta w_f = \underbrace{\frac{2(1-\nu)L_f}{G_{dr}}\sqrt{1-x^2}}_{1/K_{dr}^{fr}}\delta p,$$

where G_{dr} is the drained shear modulus of the reservoir. Note that K_{dr}^{fr} depends on L_f and the

location of fracture gridblocks from the injection point.

we can there fore extend Equation 2.17 as

$$w_f N_{JK}^f c_f \frac{\partial p_K}{\partial t} + S_J \frac{\partial w_f}{\partial t} + \frac{\partial q_J}{\partial x} = 0, \quad \text{where} \quad q_J = -\left(\frac{w_f^3 k_r}{12\mu}\frac{\partial p}{\partial x}\right), \tag{2.22}$$

where N_{JK}^f is modified for multiphase flow along the fracture and it becomes

$$N_{JK}^f = \begin{bmatrix} N_{gg}^f & N_{gw}^f \\ N_{wg}^f & N_{ww}^f \end{bmatrix} = \begin{bmatrix} S_g c_g - \frac{dS_w}{p_{cg}} & \frac{dS_w}{dp_c g} \\ \frac{dS_w}{p_{cg}} & S_w c_w - \frac{dS_w}{p_{cg}} \end{bmatrix} \tag{2.23}$$

Then, we can also discretize Equation 2.20 in time similar to Equation 2.14 as follows

$$w_f^k \left(N_{JK}^f + \frac{S_J S_K}{K_{dr}^{fr}}\right)(p_K^{n+1,k+1} - p_K^n) - w_f^k \frac{S_J S_K}{K_{dr}^{fr}}(P_K^{n+1,k} - P_K^n) + S_J^k (w_f^{n+1,k} - w_f^n) + \Delta t \frac{\delta q_J^{n+1,k+1}}{\delta x} = 0, \tag{2.24}$$

$$\text{where} \quad q_J^{n+1,k+1} = -\left(\frac{w_f^{3\,n+1,k} k_r}{12\mu}\frac{\delta p^{n+1,k+1}}{\delta x}\right),$$

The fracture conductivity in $q_J^{n+1,k+1}$ is calculated from the fracture aperture at the previous iteration level. Note that the assumption of constant pressure in Equation 2.21 is only used for estimating K_{dr}^{fr}, which does not mean constant pressure of the flow problem within the fracture.

2.4 Failure model

We used two different approaches to model the mechanical failure. Firstly, we employ the Mohr-Coulomb model to see the stress evolution. The Mohr-Coulomb failure criterion has been widely used for various mechanical analysis. Still, many routine design calculations in the geomechanics are still conducted under Mohr-Coulomb criterion based on an assumption that failure is determined by the maximum shear stress and that this failure shear stress relies on the normal stress. Instead of using Mohr's circle, we employ the principal stress path in relation to Mohr-Coulomb failure criterion for states of stress at each time step in terms of the maximum and minimum principal stresses, which is written as

$$f = \tau'_m - \sigma'_m \sin\Psi_f - c_h \cos\Psi_f \leq 0, \tag{2.25}$$

$$g = \tau'_m - \sigma'_m \sin\Psi_d - c_h \cos\Psi_d \leq 0, \tag{2.26}$$

$$\text{where} \quad \sigma'_m = \frac{(\sigma'_1 + \sigma'_3)}{2} \quad \text{and} \quad \tau'_m = \frac{(\sigma'_1 - \sigma'_3)}{2},$$

where σ'_1 and σ'_3 are the maximum and minimum principle effective stresses, respectively. Ψ_f and Ψ_f are the friction and dilation angles.

2.4.1 Shear and Tensile Failure with Interface Element

For the analysis of fault reactivation and slip behavior and wellbore stability in methane hydrate deposits, we developed the two-way coupled flow and geomechanics simulator with FLAC3D (Fast Lagrangian Analysis of Continua in 3 Dimensions). Both studies need to define the slippage phenomenon and normal detachment on the surface of interest (e.g., Surface of

the fault core, and surface between production wellbore and reservoir formation) because pressurization or depressurization results in the frictional forces on the surface due to the different properties of the materials. These frictional forces cause tensile, compressive, shear stresses on the materials and seismic events when the slip area sufficiently large. FLAC3D provides the interface model characterized by Coulomb sliding and/or tensile and shear bonding so that we can investigate the non-linear behavior of the surface. The normal and shear forces at the interface are determined at calculation time $(t + \Delta t)$ through the following equations

$$F_n^{(t+\Delta t)} = k_n u_n A + \sigma_n A, \tag{2.27}$$

$$F_{si}^{(t+\Delta t)} = F_{si}^{(t)} + k_s \Delta u_{si}^{\left(t+\frac{1}{2}\Delta t\right)} A + \sigma_{si} A, \tag{2.28}$$

where F_n and F_{si} are the normal force and shear force vector, respectively. u_n is the absolute normal penetration of the interface node into the target face, and Δu_{si} is the incremental shear displacement vector. σ_n and σ_{si} denote the additional normal and shear stress vector added due to stress initialization on interface, respectively. k_n and k_s are the normal and shear stiffness. A is the surface area formed by the interface elements and nodes.

Figure 2.1 shows the schematic concept of force transfer at the interface with stiffness. T_s and S_s are the tensile strength and shear strength, respectively. D and S denote dilation and slider.

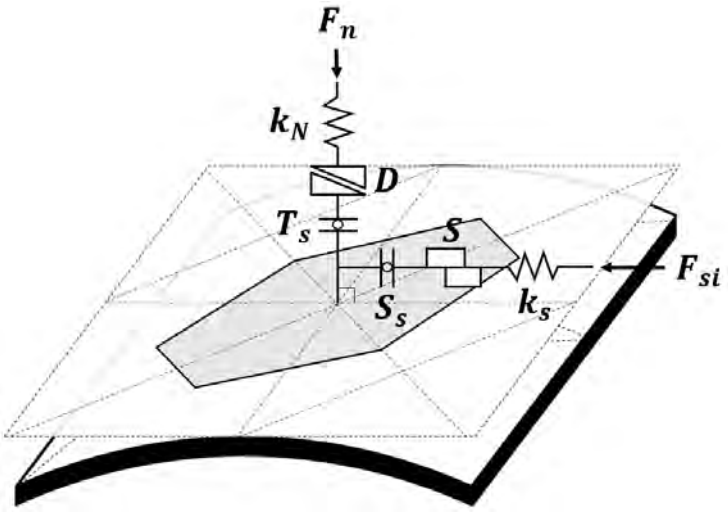

Figure 2.1: Components of the interface constitutive model.

According to Equation 2.28, we note that the transferred shear stress at the interface is a function of coupling stiffness K_n and K_s, shear displacement, shear stress vector Δu_{si}, and area A. K_n and K_s are usually determined by measurements of stress and deformation through triaxial test or direct shear test [96] [97]. In this study, the normal and shear stiffness are based on empirical models provided by FLAC3D, which are a function of bulk and shear modulus of the material as follows

$$k_s = k_n = \max \left[\frac{K + \frac{4}{3}}{\Delta Z_{min}} \right] \tag{2.29}$$

where ΔZ_{min} is the smallest width of the nearest zone in the normal direction. The $\max$ [ ] notation denotes that the maximum value among all zones near the interface that is to be used [62].

The shear stress on the interface is proportional to the displacement of the adjoining zone due to the shear displacement term. Shear failure occurs when the shear stress on the interface

reaches the shear strength since the shear stress at the interface elements cannot exceed the shear strength of the material. Here, we adopt a slip-weakening law instead of Coulomb friction law as it enables to reduce the coefficient of friction from static to dynamic friction value against the given slip displacement (critical shear strain) shown in Figure 2.2. One of the key input parameters in the modeling of post-failure behavior of fault is the coefficient of friction. A microseismic event is observed as fault weakens when the fault slip happens at a higher rate than the rate of release of tectonic stresses caused by fault movement. Thus, we adopt the slip weakening model which is commonly used in other studies [98] [99]. For example, the coefficient of friction gradually reduces from an initial value (static) of 0.6 to a residual value (dynamic) of 0.3 over a pre-defined slip displacement. As discussed in several papers [100] [101], the coefficient of friction often is treated uncertain and it can be considered as one set of possible parameters having a relatively large influence on modeling fault movement and estimating the magnitude of an injection-induced seismic event.

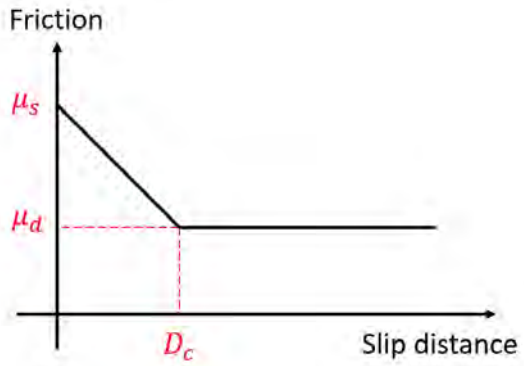

Figure 2.2: Slip weakening friction model showing friction value as a function of cumulative slip distance, where μ_s static friction, μ_d dynamic friction, and D_c slip-weakening critical distance.

2.4.2 Tensile Failure for Fracture Propagation

In fracture mechanics, the fracture propagates when the stress intensity factor σ'_{SIF} exceeds material toughness K_{IC} as follows [102]

$$\sigma'_{SIF} > K_{IC} \tag{2.30}$$

For the case of the bi-wing vertical fracture propagation under the plane strain condition shown in Figure 2.3, the criterion of the fracture propagation can be expressed as [78]

$$\int_0^{L_f} \frac{p - \sigma_H}{\sqrt{L_f^2 - x^2}} dx \geq \frac{K_{IC}}{2L_f}, \tag{2.31}$$

where L_f and σ_H are the fracture half-length and magnitude of far-field in-situ minimum horizontal total stress, respectively. In this study, we consider this bi-wing fracture case typically employed in the hydraulic fracture analysis. In the numerical simulation, a fracture node can be split when Equation 2.31 is satisfied [65].

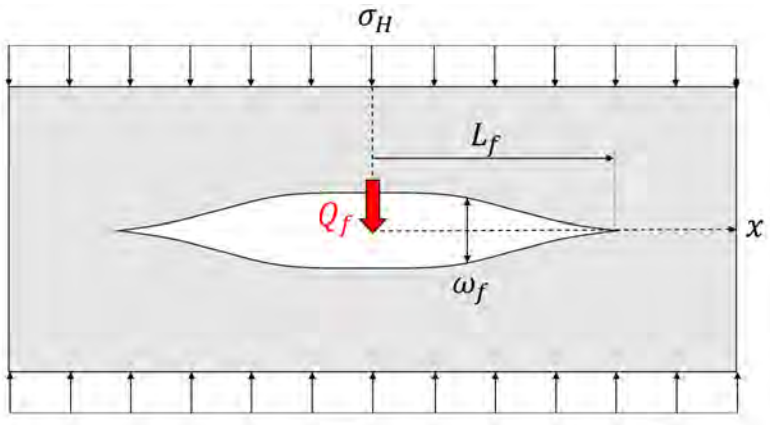

Figure 2.3: A bi-wing vertical hydraulic fracture under the plane strain condition.

3. FAULT REACTIVATION, SLIP AND INDUCED SEISMICITY FOR GEOLOGICAL CO_2 STORAGE SITE

In this chapter, we explain the newly developed coupled flow (inhouse)-geomechanics simulator using FLAC3D. The simulator can be used on any complex 3D structural model to conduct the study with various applicable scenarios to understand the risks of situations like tension/shear failure in any geological location while monitoring the effects of reservoir pressurization. Furthermore, we model the post-failure behavior of faults and estimate the seismic magnitude in a pilot-scale CO_2 storage site named Janggi sedimentary basin located in the southeast area of South Korea.

3.1 Simulator and its Validation

For this study, the developed simulator was designed with the aim of it being capable of analyzing coupled flow, thermal and geomechanical processes reliably while accounting for all known flow, physical and thermodynamic processes that are associated with simulating processes involving CO_2 and water (the two components considered in this study along with its possible phases). The complexity and the extreme non-linearity of the problems investigated in this study prevent the exact benchmarking of the developed code with solutions for full validation. However, to reliably assess the accuracy of our coupled simulator:

- First, we validate the flow simulator against results from TOUGH2/ECO2N which is an established simulator capable of accurately simulating CO_2 sequestration processes in aquifers.

- Second, we validate the geomechanics modules of our simulator against the analytical solution to the displacement function provided by McNamee and Gibson.

Moreover, to validate the successful coupling of the flow and geomechanics modules we try to illustrate the effectiveness of the developed simulator in capturing the Mandel-Cryer effect accurately.

3.1.1 Validation of the Flow Simulator

Several numerical simulations were performed to validate the accuracy of our in-house flow simulator with the results from existing solutions developed using the TOUGH2/ECO2N simulator [103]. The results from one of these studies is presented here. The TOUGH2/ECO2N manual provides values of density, viscosity, and mass fraction of dissolved fluid in each phase at select pressures at a temperature of 45°C. Table 3.1 provides the comparison for density, viscosity, and mass fraction of dissolved carbon dioxide in aqueous phase, while Table 3.2 lists the density and viscosity values along with the water mass fraction in gaseous phase. Figure 3.1 shows the set of results associated with these two tables in the form of a graph. At the listed pressures and temperatures, there is less than 1% discrepancy in density and viscosity values between the two simulators in aqueous phase, while the mass fraction of dissolved carbon dioxide shows a difference of around 3% compared to the reference value. For the gaseous phase, our in-house simulator generates similar results in density and mass fraction of water. The results of viscosity tend to show a minor deviation against the reference value as pressures decrease. It is surmised that the minor deviations in the results are owing to different equations being used for calculating these thermophysical properties. All in all, the accuracy of our in-house simulator is supported by the near agreement of our results with the

	Density, Kg/m3		Viscosity, Pa·s		Water mass fraction	
Pressure, Bar	TOUGH2	INHOUSE	TOUGH2	INHOUSE	TOUGH2	INHOUSE
120	658.261	638.065	5.176E-05	3.721E-05	2.147E-03	2.097E-03
160	769.931	733.489	6.565E-05	5.555E-05	2.416E-03	2.374E-03
200	813.504	790.908	7.452E-05	7.099E-05	2.544E-03	2.527E-03
240	850.176	833.224	8.159E-05	7.904E-05	2.627E-03	2.628E-03

Table 3.1: Comparison of PVT properties at a temperature of 45 °C and at selected pressures for single phase with gas.

	Density, Kg/m3		Viscosity, Pas		CO_2 mass fraction	
Pressure, Bar	TOUGH2	INHOUSE	TOUGH2	INHOUSE	TOUGH2	INHOUSE
120	1005.79	1008.95	5.978E-04	5.979E-04	5.206E-02	5.128E-02
160	1008.00	1011.17	5.983E-04	5.986E-04	5.551E-02	5.363E-02
200	1009.94	1013.28	5.989E-04	5.993E-04	5.766E-02	5.596E-02
240	1011.74	1015.31	5.995E-04	6.001E-04	5.919E-02	5.735E-02

Table 3.2: Comparison of PVT properties at a temperature of 45 °C and at selected pressures for single phase with liquid.

ones generated using TOUGH2/ ECO2N.

3.1.2 Validation of the coupled flow and geomechanical model

We employ a 2D plane strain problem with a strip-footing for the validation of coupling process shown in Figure 3.2, also known as the McNamee and Gibson's problem [104][105]. Table 3.3 lists the geomechanics and hydraulic properties that were used in the validation. A grid dimension of 110.0001 m $\times$ 1 m $\times$ 110.0001 m (21 $\times$ 21 $\times$ 1 grids) was used and a very thin layer of thickness 0.0001 m was placed at the top and left boundaries. The grid size for the problem was gradually increased from 1 m to 16 m from these boundaries. For geomechanical boundary conditions, roller boundaries were applied at the left, right, and bot-

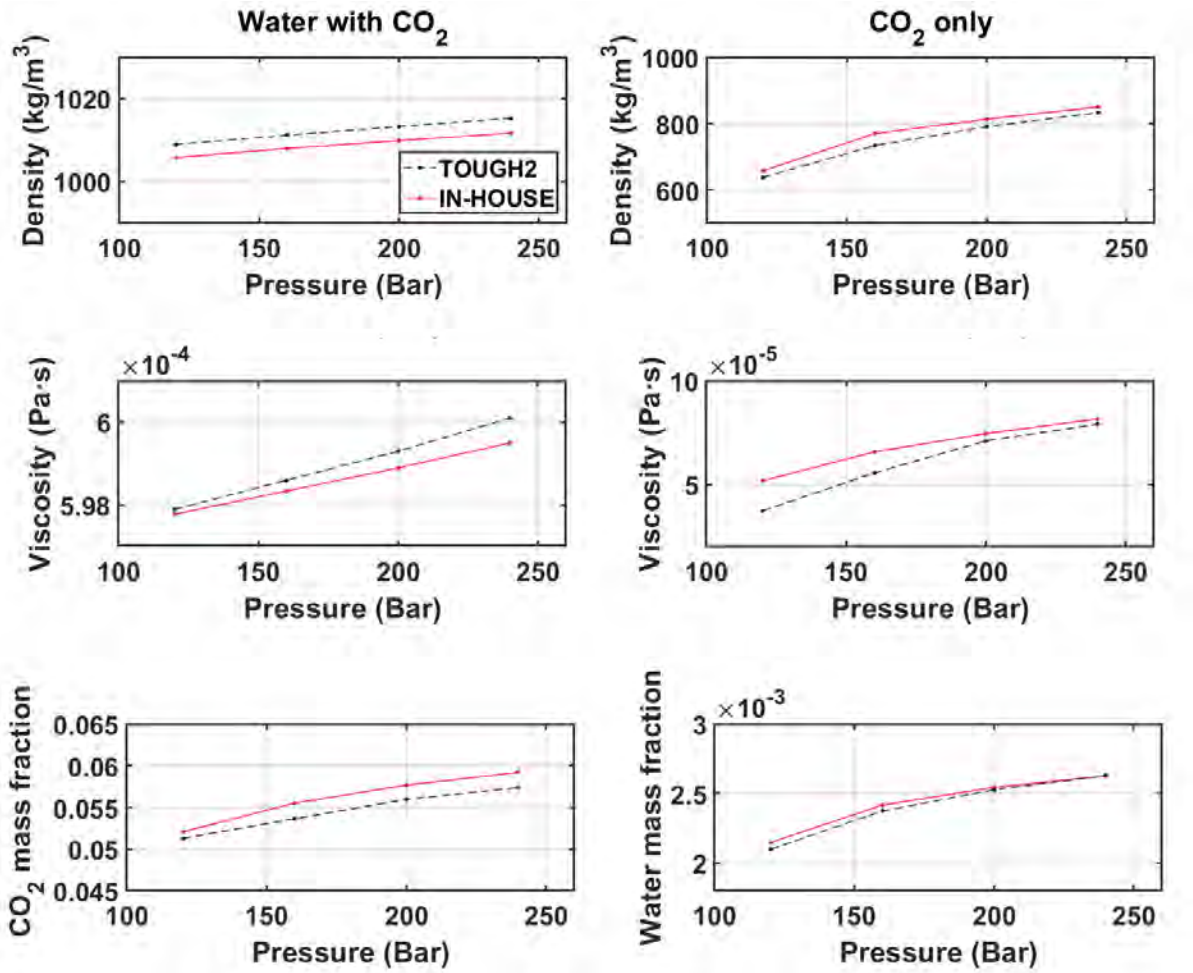

Figure 3.1: Comparison plot for results listed in Table 1 and 2.

tom boundaries. In other words, there is no displacement in a direction perpendicular to any boundary. An overburden of 10 MPa is applied at the left 4.0001 m of the top boundary. For fluid flow conditions, a no-flow boundary is set along all four boundaries. The initial timestep size begins with $\Delta t = 10^{-3}\ s$, which is doubled until it reaches $\Delta t = 1.0\ s$. The evolution of pressure at the monitoring gridblock (Grid1, Centroid=[0.00001 m, 3.5001 m]) marked in Red in Figure 3.2 was used to compare the numerical results with the analytical solution shown in Figure 3.3. Moreover, Figure 3.3(b) shows the spatial distribution of pressure in the entire

Mechanical properties			Hydraulic properties		
Initial total stress	-10	MPa	Porosity	0.25	fraction
Young's modulus	450	MPa	Compressibility	4.00E-10	Pa^{-1}
Poisson's ratio	0		Permeability	50	mD
			Viscosity	1E-3	Pa·s
			Initial pressure	10	MPa
			Boundary condition	No flow	
			Biot's coefficient	1.0	

Table 3.3: Input parameters for McNamee and Gibson's problem.

simulated system after a period of 2000 seconds. Note that in Figure 3.3(a) when traction is applied to the boundary at the initial time, the pore pressure increases due to the compatible interaction between the fluids inside the pore space and the solid skeleton as it deforms. This phenomenon is also called the Mandel–Cryer effect. This effect though derived theoretically has also been observed experimentally for ideal poroelastic materials [106] [107]. The poroelastic response is normally observed under planar strain conditions. Despite the minor error at early times in the validation results, we are able to observe the Mandel-Cryer effect with the proposed numerical simulation method. This validates not only the geomechanics module but also the successful coupling of our flow and geomechanics simulators.

3.2 Geological description of study area

A pilot-scale CO_2 storage project was conducted in the southeast of South Korea in a basin known as the Janggi sedimentary basin. Its geographic location is shown in the right corner of Figure 3.4. Several geophysical surveys (seismic, gravimetric, and magneto-telluric) have been carried out in the area to map in detail the subsurface geological structures in the area. Drill sites were selected in the area for further detailed site characterization based on the in-

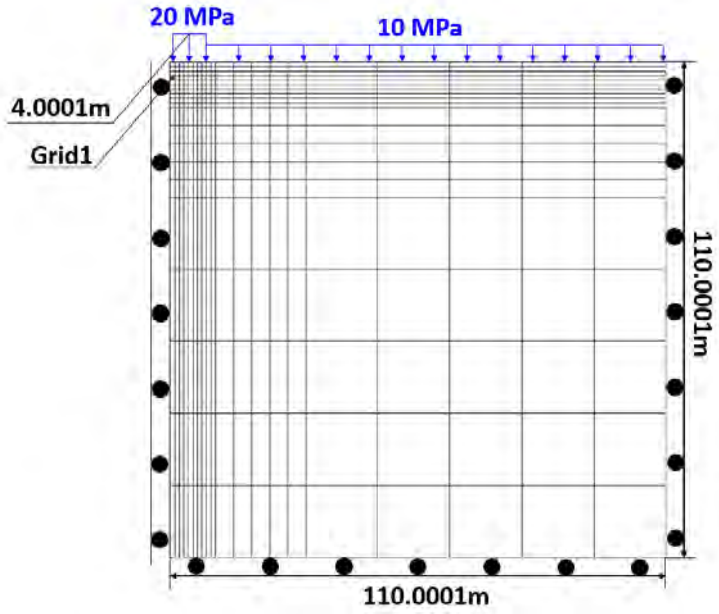

Figure 3.2: A 2-dimensional (2D) plane strain strip-footing consolidation problem (McNamee-Gibson's problem).

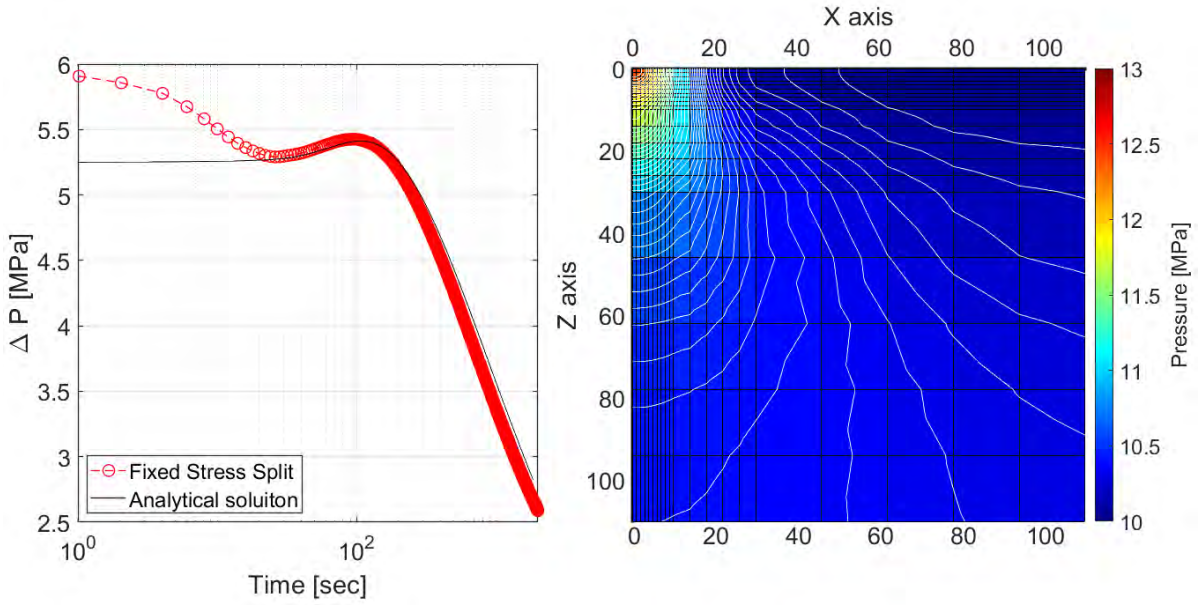

Figure 3.3: (Left) Evolutions of pressure increase from the initial reservoir pressure at the monitoring grid (Grid1 in Figure 3.4) with analytical solution and (Right) pressure distributions at time (t = 2000 s).

terpretation of the geophysical surveys. A total of 7 exploration boreholes were drilled, which have been located according to their names in Figure 3.4 (JG1-JG7). All the wells that were drilled in the area were logged and whole-round cores were extracted along their trajectories from the surface to the target depth. All the acquired cores were analyzed in a laboratory setting to estimate their petrophysical properties. The core logs were used to construct stratigraphic columns [1] shown in Figure 3.5. Results from well-logging and geophysical survey were later tied to core log results to integrate data across scales. An Injection well was also drilled in the area shown as the red dot in Figure 3.4.

The site characterization studies identified the Janggi conglomerate consisting of mainly clastic conglomeratic sandstone and fine grain sandstones as a potential reservoir stratum. It belongs stratigraphically to the lower part of early Miocene Seongdong-ri sedimentary formation [108] which in itself is a thick layer consisting mainly of interbedded mudstones and sandstones as well as some layers of igneous lithology (Noeseongsan basaltic rocks) located at some depths. The reservoir thickness varies from 50 m to over 200 m based on data acquired from the drilled wells.

For example, at JG6, the Janggi conglomerate is located between a depth interval of 950 m and 1050 m, and the layer lies just above the Eocene volcanic basement rock. The overlaying upper regions of the Seongdong-ri formation (discussed before) above the reservoir stratum appear to provide a good seal for the containment of injected CO_2. Interpretations of the geophysical survey data seem to indicate the presence of a normal fault striking $\sim 40^\circ$ northeast and dipping $\sim 70^\circ$ towards the northwest. The geological projection of the fault on the surface has been shown in Figure 3.4 with a white dotted line. An injection borehole was drilled $\sim$200

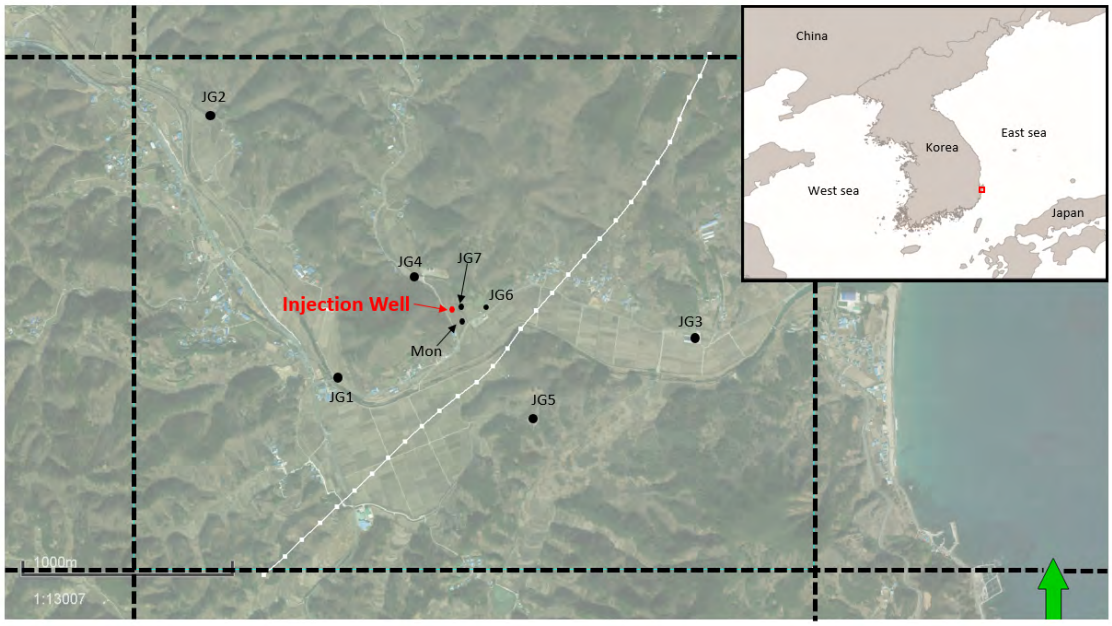

Figure 3.4: Location map of pilot-scale CO_2 storage site in South Korea showing the area enclosed by black-dashed lines representing the simulated zone for CO_2 storage, the location of appraisal boreholes (JG1 to JG7), and an injection well

m away from the fault, while a monitoring borehole was drilled ∼30 m southeast away from the injection borehole to observe the effects of the injection process. One of the operational issues of this project is the potential reactivation of the reservoir-bounding fault due to elevated reservoir pressure caused by CO_2 injection into the reservoir. Fault reactivation has been a documented cause of leakage of stored CO_2 due to the creation of channels of enhanced permeability along the fault due to the effects of slippage and/or an earthquake [109]. Therefore, it is very crucial to avoid fault reactivation to ensure the success of CO_2 storage. In this study, we have run numerical simulations to evaluate various cases that might cause fault instability due to CO_2 injection at different rates.

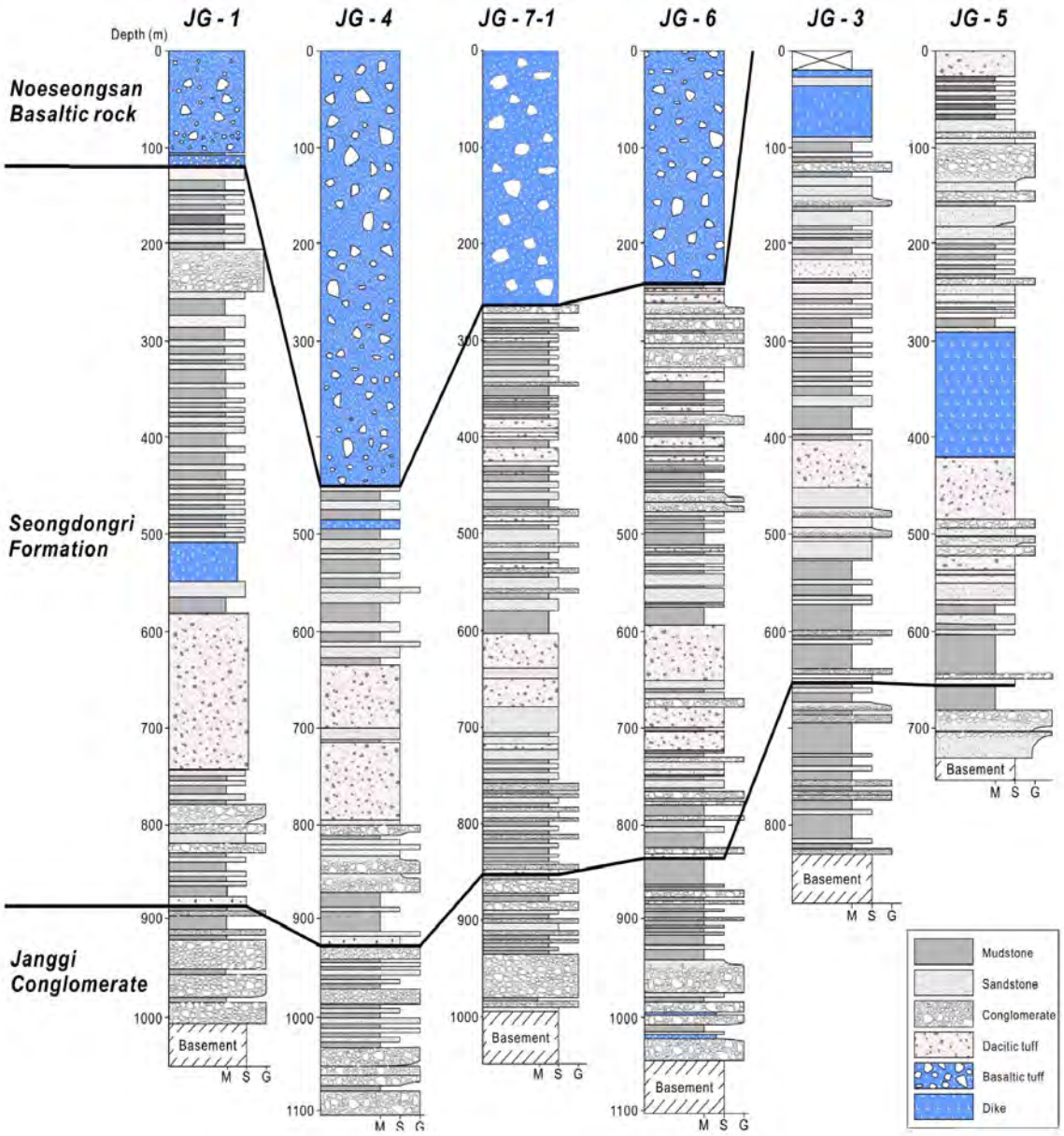

Figure 3.5: Stratigraphic columns constructed from core logging [1]

3.3 Numerical modeling

3.3.1 Model description

A subsurface model of the geological structure was built by processing and interpreting the field geophysical data and integrating it with results from well logging and core analyses. Figure 3.6(a) shows the resulting structural model which dimension is $\sim$3 km $\times$ $\sim$1.9 km $\times$ $\sim$1.25 km in the East (X), North (Y) and downward (Z) directions, respectively. The portion of structural model is used for the simulation of fluid flow illustrated in Figure 3.6(b) and Figure 3.6(c). The numerical model for the fluid flow shown in Figure 3.6(b) consists of 4 layers intersected by a growing normal fault (representing the fault identified in the area from the geophysical surveys). An injection borehole (representing a well, JG9) is located at the center of the model, which had been proposed to be drilled approximately $\sim$200 m away from the fault. A monitoring borehole (JG8) was drilled $\sim$30 m southeast of the injection borehole.

As mentioned before, (in-house)-FLAC3D flow and geomechanics simulator is used to conduct a detailed coupled multiphase fluid flow and geomechanical analysis of the fracture zone response with the complex 3D grid system. To construct the 3D grid, representing the geological structure, we have meshed the geometry of the subsurface geological model first and a reservoir model is embedded as part of the geomechanical model. Note that, the domain for the geomechanical model is much larger than the flow model not only to capture geomechanical responses including surface uplifting phenomena but also to gauge the magnitude of surface uplift it is necessary to consider the structure in its entirety. This contrasts with the flow model wherein we are only interested in the layers representing the reservoir

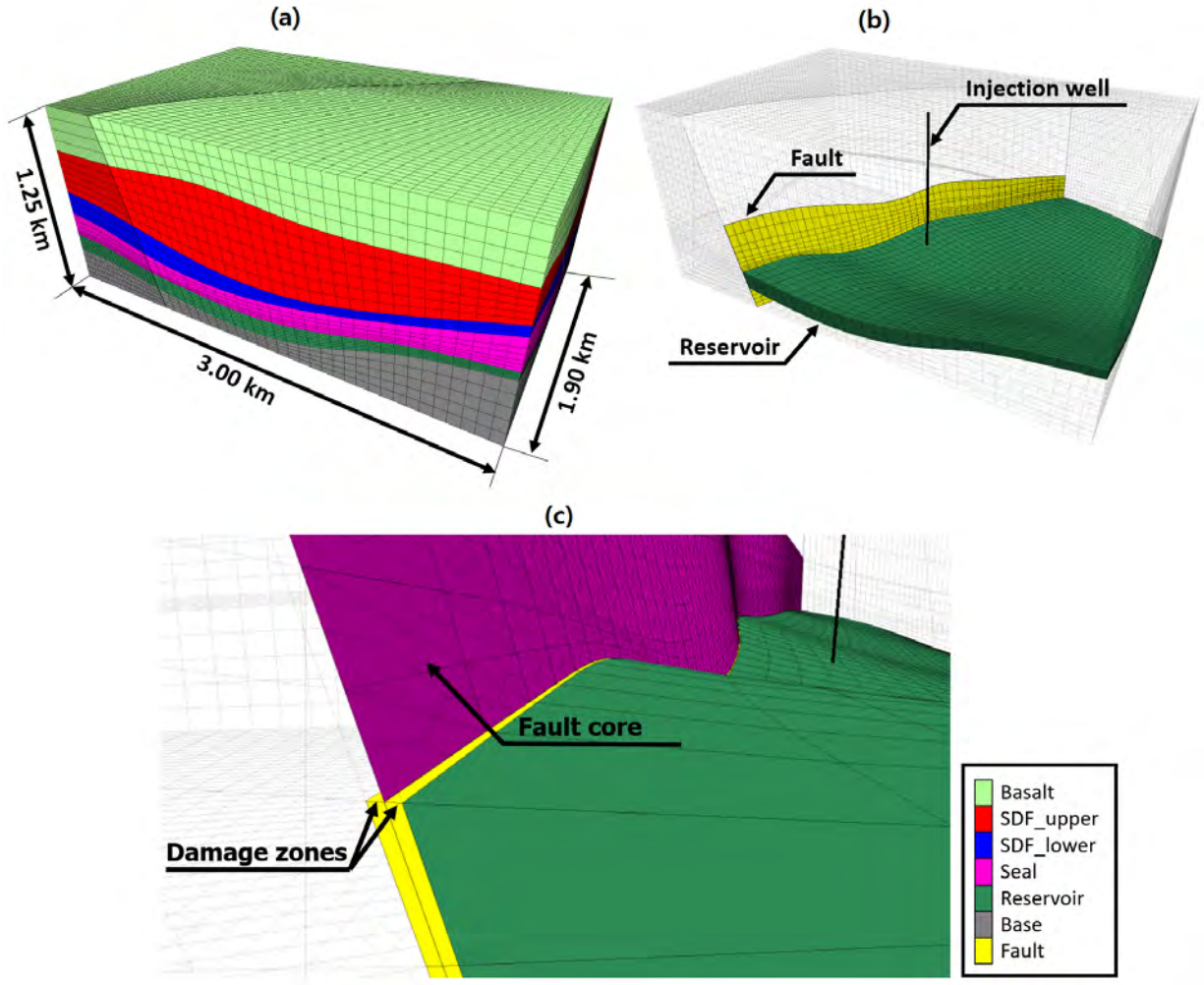

Figure 3.6: (a) A subsurface model based on 7 different types of lithology (93000 grids), (b) representation of fault, reservoir, and injection well location by discrete interfaces (9000 grids), and (c) structure with a single core fault surrounded damage zones.

for flow simulation and pressurization. The logic for using such an approach is explained in greater detail in the ensuing sections. The numerical model for geomechanics has 93,000 gridblocks for the whole geological structure while the reservoir and fault are represented in total by 9000 gridblocks. To observe the impact of injection-induced pressurization on the compaction of the overburden and underburden layers, few test simulations were run. Inves-

tigation of the results seen in Figure 3.7 shows that the observable pressure changes in the layers right above and below the reservoir vary between 1.6 MPa and -3.9 MPa. The pressure change observed is evidently higher only in the vicinity of the injection well. Nevertheless, these values are not significant when compared to the pressure changes that shall be observed in the reservoir due to the entire injection process. Thus, we can conclude that we need to only consider the reservoir and fault for the fluid flow numerical model to save computational cost. The reservoir-bounding fault is represented by solid elements with a thickness of $\sim$2 m. Using such an approach facilitates the creation of 3D grids which can take the complex geometry often seen in discrete faults into consideration. By integrating this sort of mesh into our in-house simulator, we are able to build a structural model of a curved fault without any simplification, as shown in Figure 3.6(b). This is one of the many benefits of the workflow used in our in-house simulator as it is able to bypass a general lack of flexibility or modularity in terms of integrating any scientific source or solutions into the numerical simulation process. This is in sharp contrast with the issues often faced when dealing with commercially available solutions for numerical analyses as they are typically very rigid in terms of integrating new physics into simulation studies.

A key feature of this study is that we treat the fault core as a discontinuous surface surrounded by damage zones as shown in Figure 3.6(c). The use of this logic enables us to accurately model fault slip movement, as due to this consideration, the displacement along this region can be discontinuous and therefore it can be under evolving fluid pressure and fault strength. The details of the method are provided by FLAC3D [62] and the mathematical formulation of zero-thickness elements are covered in detail in Section 2. Left figure of Fig-

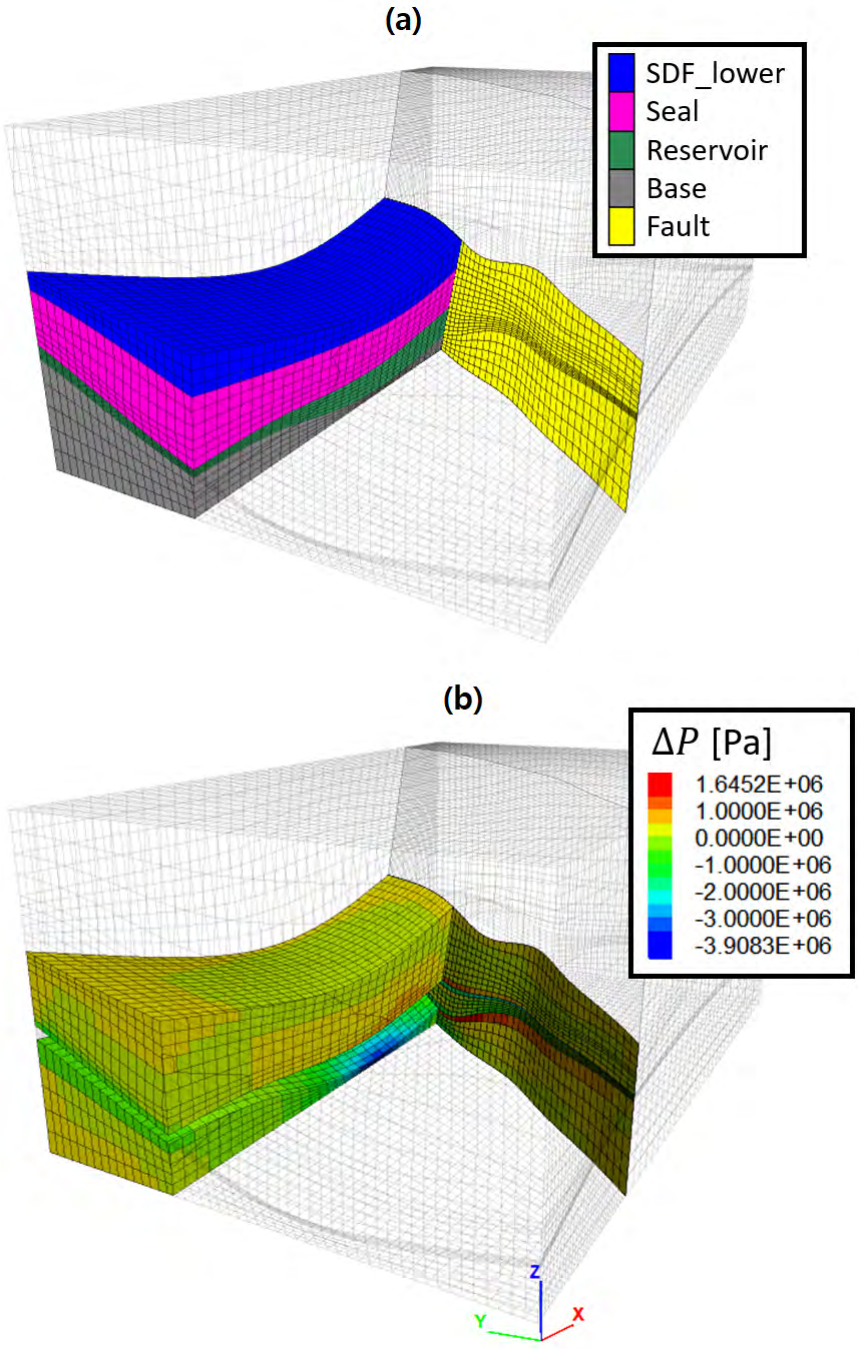

Figure 3.7: (a) Numerical model for fluid flow demonstrating the impact of the pressurization on over- and under-burden layers. (b) simulation results of pressure changes over the domain for 20-year injection at 200 tons/day.

ure 3.8 represents the schematic image of a fault consisting of damage zones and a single fault core (highlighted in red), the simplified structure of the same used in the numerical model is shown in Figure 3.8(right).

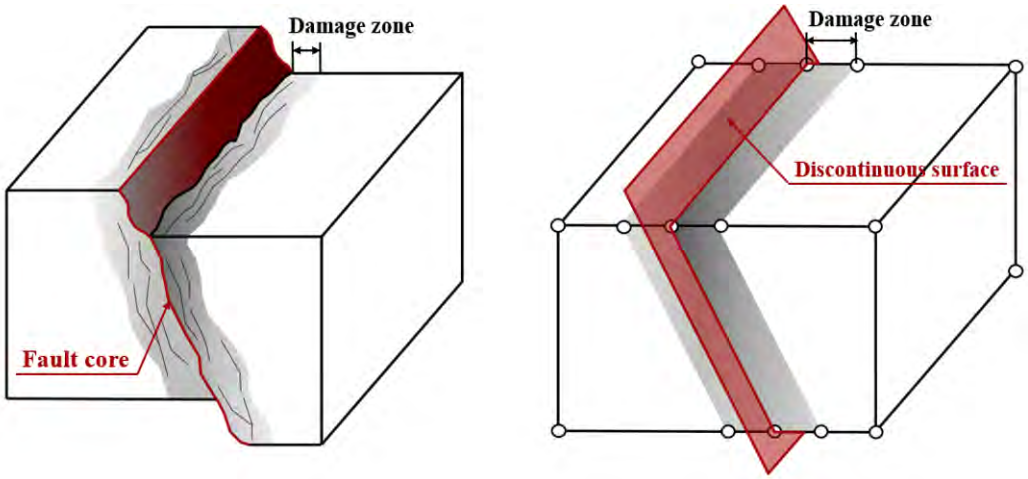

Figure 3.8: (Left) Schematic image of the fault zone and its terminology. (Right) Representation of numerical model.

With the two-way sequential coupling method, as mentioned before, our in-house simulator deals only with 9000 gridblocks for fluid flow and delivers values to FLAC3D to perform geomechanical analysis by implementing a specific routine written in FISH, the internal programming language of FLAC3D, to update reservoir properties with the newly calculated values (Figure 3.9 shows the implemented algorithm). The explicit finite difference method and the finite volume method are used for space discretization in geomechanics (FLAC3D) and fluid flow (in-house code), respectively. The backward Euler method is employed for time discretization. The Injection well has the same coordinates as specified in the geographical map shown in Figure 3.4. The introduction of interfaces in the numerical model makes it

possible to investigate in detail the potential of fault reactivation/slip brought about by stress changes due to fluid flow within the reservoir.

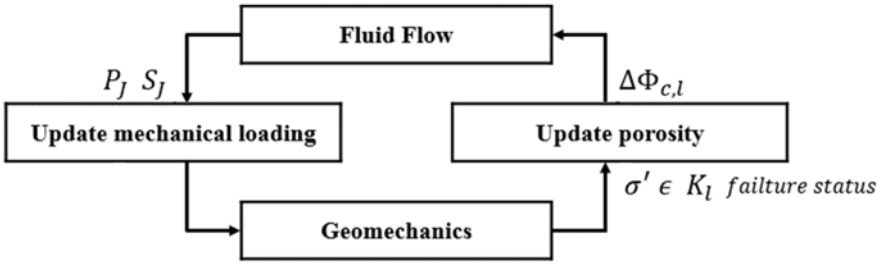

Figure 3.9: Sequential implicit algorithm based on fixed-stress split method [2].

3.3.2 Petrophysical Properties of Simulation Domain

7 appraisal boreholes were drilled in the area and cores from which were extracted from the surface to the target depth are tested. Petrophysical properties acquired from these were used in characterizing the material properties of the lithologies that were used as a reference to divide the zones during numerical simulation. Results from the analysis and lab test helped us conclude that the permeability of the system representing the reservoir is about 16.7 mD (=1.670E-14 m^2) on average. We also require constitutive relationships for relative permeability and capillary pressure in the geologic media of this project. For the purposes of this study, we employed Corey's curves for relative permeability and the van Genuchten function for capillary pressure. Uniaxial and triaxial compression tests under the drained condition on core samples were performed from JG1 and JG4 to determine the mechanical properties of the formations including the reservoir. Furthermore, since geophysical well logging had been

carried out in all wells drilled in the area, we were able to use data to confirm the petrophysical properties that were used in this study. Since none of the appraisal boreholes drilled in the area passed through the fault, data relating to fault materials and well logging for it was not available. Hence, it is not possible to constrain the mechanical properties of the fault. As an alternative, the mechanical properties of the fault (listed in Table 3.4) was assumed by studying data listed in several papers [110] [111] [112] [113]. The fault is treated as a narrow impermeable zone with low Young's modulus and cohesion-less frictional materials. A strain-softening fault constitutive model is used to simulate the seismic fault slip. Discrete events of fault activation that were observed and the associated seismic moment magnitude have been elaborated in the results. A static friction coefficient of 0.6 (Friction angle $\approx 31^{\circ}$) is used while the dynamic friction is considered to be 0.3 (Friction angle $\approx 16.7^{\circ}$). The assumed values represent a reasonable lower and upper bound value, irrespective of rock types and stresses on the fault, when there are no weak clay materials within the fault plane. As a result, the geological model is structured with 7 zones to assign the different geological parameters for each zone such as density and bulk/shear modulus, which leads to realistic outcomes in values of stress tensor and displacement in FLAC3D. Table 3.4 and Table 3.5 provides the input properties of the reservoir/fault and geomechanics respectively used in the numerical simulation. Note that the assumption of impermeable fault zone allows for having different numerical simulation grids in the in-house simulator and FLAC3D.

3.3.3 Simulation results

For the initialization of pressure distribution due to overburden in the entire system, we start from the pressure of about 0.46 MPa at a depth of 50 m below sea level with a gradient that

Hydraulic properties		
Initial permeability	1.670E-14	m^2
Pore pressure at the surface	4.900E+05	Pa
Pore pressure gradient	-9.806E+03	Pa/m
Biot's coefficient	1.000E+00	
Boundary condition		No flow
Gas density		O'Sullivan et al. (1983)
Gas viscosity		Pritchett et al. (1981)
Relative permeability		Corey et al.(1954)
Capillary pressure		van Genuchten-Mualem(1980)
Henry's constant coefficient		D' Amore and Truesdell(1988)

Fault properties			
Fault permeability		0.000E+00	m^2
Bulk modulus		3.300E+09	Pa
Shear modulus		2.000E+09	Pa
Density		2.300E+03	Kg/m^3
Porosity		3.000E-02	Fraction
Friction angle	static	3.096E+01	degree
	dynamic	1.670E+01	degree
Critical distance		5.000E-04	m
Normal stiffness		1.190E+11	Pa
Shear stiffness		1.190E+11	Pa
Joint tension		1.000E+08	Pa
Cohesion		0.000E+00	Pa
Dilation angle		0.000E+00	degree

Table 3.4: Input parameters of hydraulic and fault properties for numerical simulation

Mechanical properties			
Stress at the surface	x	-1.36E+06	Pa
	y	-9.90E+05	Pa
	z	-1.24E+06	Pa
	xy	-3.13E+05	Pa
Stress gradient	x	2.72E+04	Pa/m
	y	1.98E+04	Pa/m
	z	2.47E+04	Pa/m
	xy	6.26E+03	Pa/m
Lithology 1	Bulk modulus	5.13E+09	Pa
[Basalt]	Shear modulus	4.86E+09	Pa
	Density	2.42E+03	Kg/m^3
	Porosity	1.30E-01	Fraction
Lithology 2	Bulk modulus	3.24E+09	Pa
[SDF_upper]	Shear modulus	1.76E+09	Pa
	Density	2.39E+03	Kg/m^3
	Porosity	2.27E-01	Fraction
Lithology 3	Bulk modulus	5.82E+09	Pa
[SDF_lower]	Shear modulus	4.93E+09	Pa
	Density	2.27E+03	Kg/m^3
	Porosity	1.85E-01	Fraction
Lithology 4	Bulk modulus	3.79E+09	Pa
[Seal]	Shear modulus	2.96E+09	Pa
	Density	2.40E+03	Kg/m^3
	Porosity	4.72E-02	Fraction
Lithology 5	Bulk modulus	2.53E+09	Pa
[Reservoir]	Shear modulus	1.52E+09	Pa
	Density	2.32E+03	Kg/m^3
	Porosity	1.26E-01	Fraction
Lithology 6	Bulk modulus	1.35E+10	Pa
[Base]	Shear modulus	1.33E+10	Pa
	Density	2.46E+03	Kg/m^3
	Porosity	8.00E-02	Fraction

Table 3.5: Input parameters of mechanical properties for numerical simulation

can be seen in Figure 3.10. As mentioned before, the fault has a finite thickness of 2 m and the injection well is located about 200 m from the fault plane. Here, simulation is performed with an injection rate of 200 tons/day which is a relatively large value when considering available pump capacity of 80 tons/day, already possessed by the operator in the site. Expectedly this high injection rate scenario represents an extreme case and it causes obvious shear failure on the fault plane after a certain period of injection. This is an obvious glimpse of the effects that high injection rates can have on the fault. Figure 3.11 shows the spatial distribution of the pressure and gas saturation in the reservoir after injection at a rate of 200 tons/day over 20 years. As is evident in the figures, the gas saturation and the pressure increase near the location of the injection well.

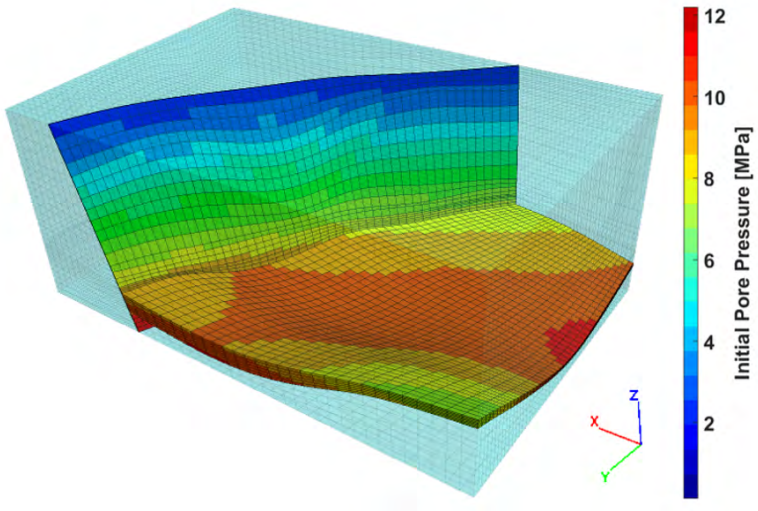

Figure 3.10: An isometric view of initial pressure before the simulation run along the fault and reservoir with gravity gradient.

It is worth noting that the pressure increment is characterized by a slight anisotropy around

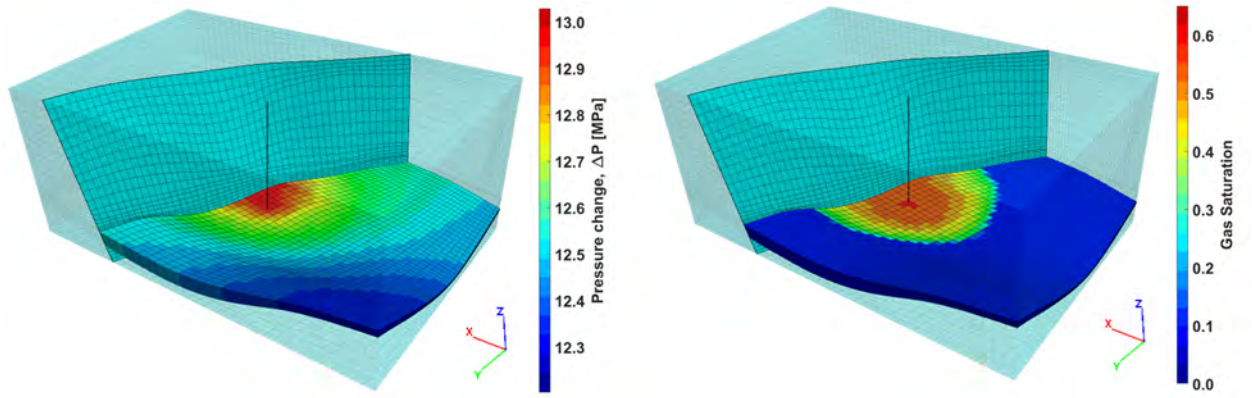

Figure 3.11: (Left) Pressure change and (Right) gas saturation with CO_2 injection of 200 tons/day for 20 years on the reservoir.

the part of the reservoir which has a shallower depth in the region of the injection well shown in Figure 3.11. This is because the fluid displacement is highest (and therefore the corresponding pressure change) in the shallower regions due to gas being a lighter phase than water which thus tends to accumulate in the shallower regions of the reservoir. Furthermore, we are interested in observing the effect of injection fluid on nodal displacement in Z-direction. A single uplift lobe is observed at the region which has a greater thickness, though it is not near the injection well location. This result can be clearly examined along a cross-sectional view passing through the injection well, i.e., the A-A′ section that can be seen in Figure 3.12(Left). The displacement contour lines in Figure 3.12(right) indicate that the displacement tends to be determined more by reservoir thickness rather than the injection point itself, where the thickness of the reservoir considerably varies with distance from the well. To record these changes in reservoir properties with time, we select a monitoring grid, marked in Figure 3.13a, which is the grid block with the least distance from the well located on the top layer of the reservoir. Figure 3.13b shows that two-way coupling imposes more porosity correction than one-way

coupling. Consequently, it leads to less pressure increment as seen in Figure 3.13c, this is because the pore volume increases slowly with time, while saturation changes at the monitoring grid are not influenced significantly by fluid injection (Figure 3.13d).

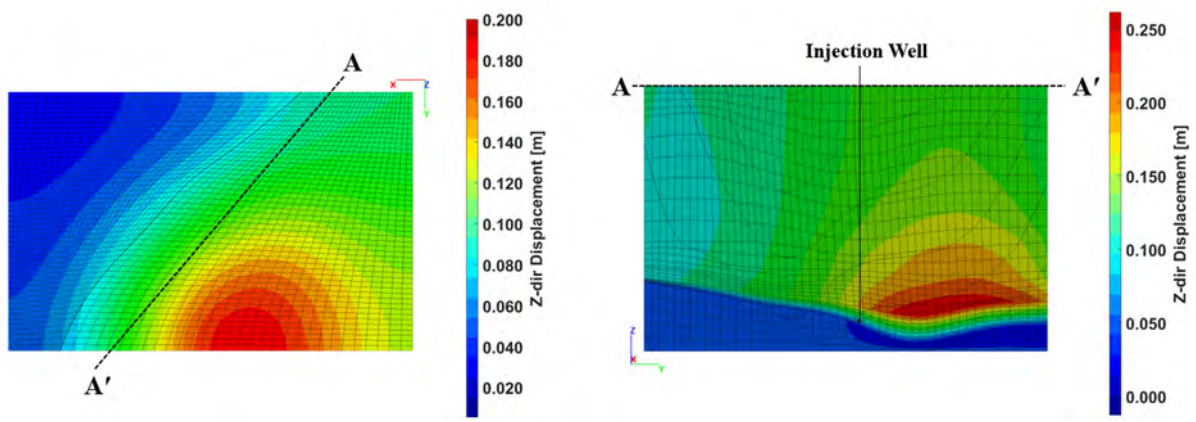

Figure 3.12: (Left) Top view of vertical (z-direction) displacement contour with CO_2 injection of 200 tons/day for 20 years at the ground surface and (Right) Cross-section view with vertical (z-direction) displacement contour with CO_2 injection of 200 tons/day for 20 years along with section A - A′.

3.3.4 Fault response

3.3.4.1 Mohr-Coulomb Failure

Firstly, we consider the fault as a finite thickness zone without using interface elements to track the evolution of stress along the fault plane. At a CO_2 injection rate of 200 tons/day most gridblocks on the fault plane which are in contact with the reservoir section have been activated at the 20-year mark (shown in Figure 3.14). In Figure 3.14, the legend term, 'shear-n' indicates yield in shear now while 'shear-p' indicates elastic state now but yield in shear past. More details on the Mohr-Coulomb failure status with time have been shown in Figure 3.15.

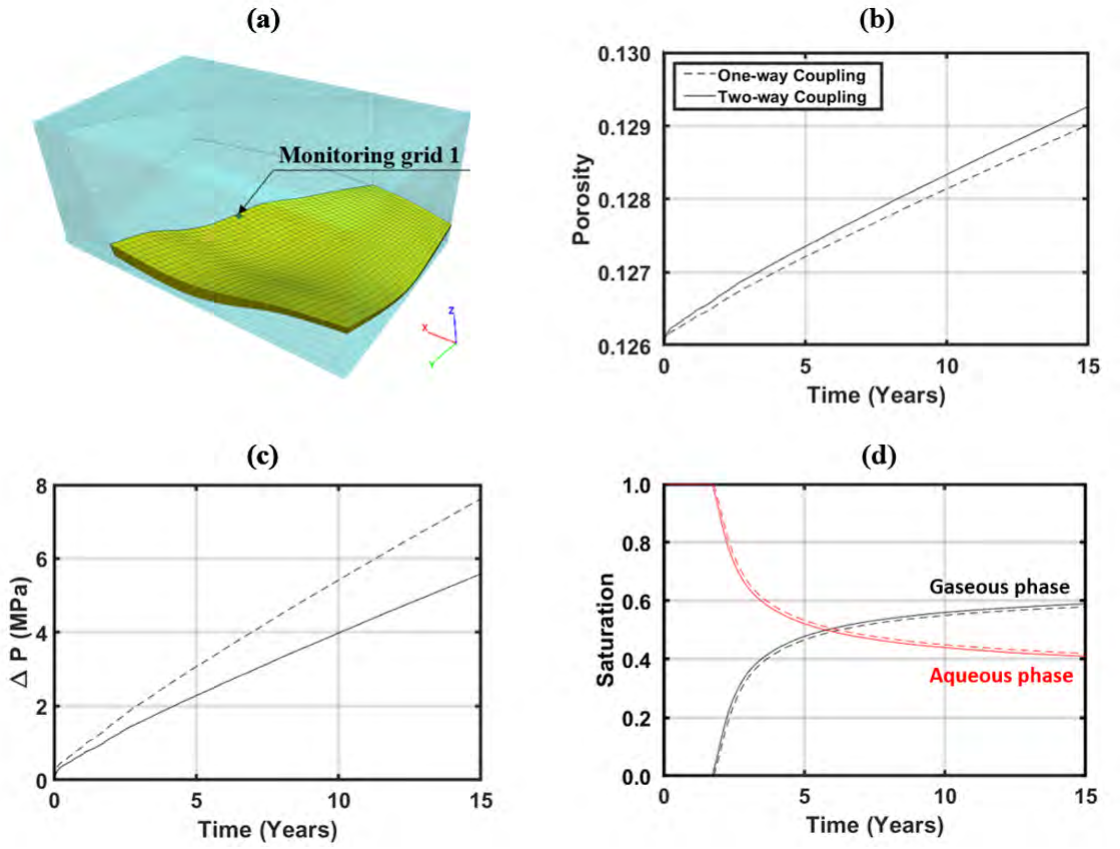

Figure 3.13: (a) An isometric view of monitoring grid 1 on the reservoir. (b) Comparison between one-way and two-way coupling results of porosity, (c) pressure change, and (d) gas/liquid saturation with CO_2injection of 100 tons/day for 15 years at the monitoring grid.

Another monitoring gridblock, (monitoring grid 2 in Figure 3.15(a), which is located right next to the monitoring grid 1 located in the reservoir as seen in Figure 3.15(a)), is selected on the fault plane to track down the evolution of the effective stress with different injection rates. At both CO_2 injection rates of 100 tons/day and 50 tons/day, the fault plane is in elastic state for 20 years. This is in contrast to the case involving injection of CO_2 at a rate of 200 tons/day where the effective stress approaches the failure envelop after 13 years, this is identical to the results of fault status in 20 years injection scenario as shown in Figure 3.14. This indicates that the fault reactivation/slip in this geological storage site could happen at a

high injection rate, leading to fluid leakage along the fault and/or injection-induced seismic events. Utilizing the Mohr-coulomb model, it is only possible to check the fault status in terms of whether it has been reactivated or not. To investigate the post-failure behavior and estimate the scale of seismic events if any, we need to identify the shear slip distance and its area with discontinuous surfaces. This enables the modeling of the two damage zones moving apart independently under frictional forces.

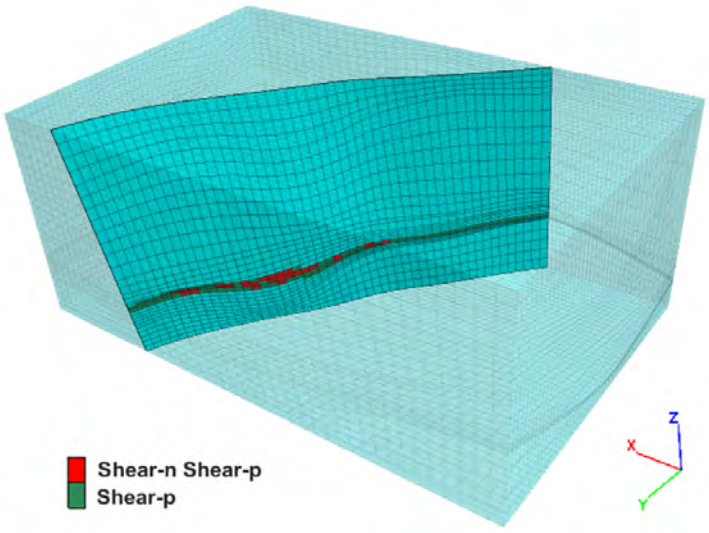

Figure 3.14: An isometric view of fault status with CO_2 injection of 200 tons/day for 20 years on reservoir and fault.

3.3.4.2 Post-Failure Behavior

We apply the interface elements to model the post-failure behavior of the fault after re-activation. We consider three possible injection scenarios to gauge the impact of differing injection quantities over a time period of 20 years at a rate of 100, 200 and, 400 tons/day.

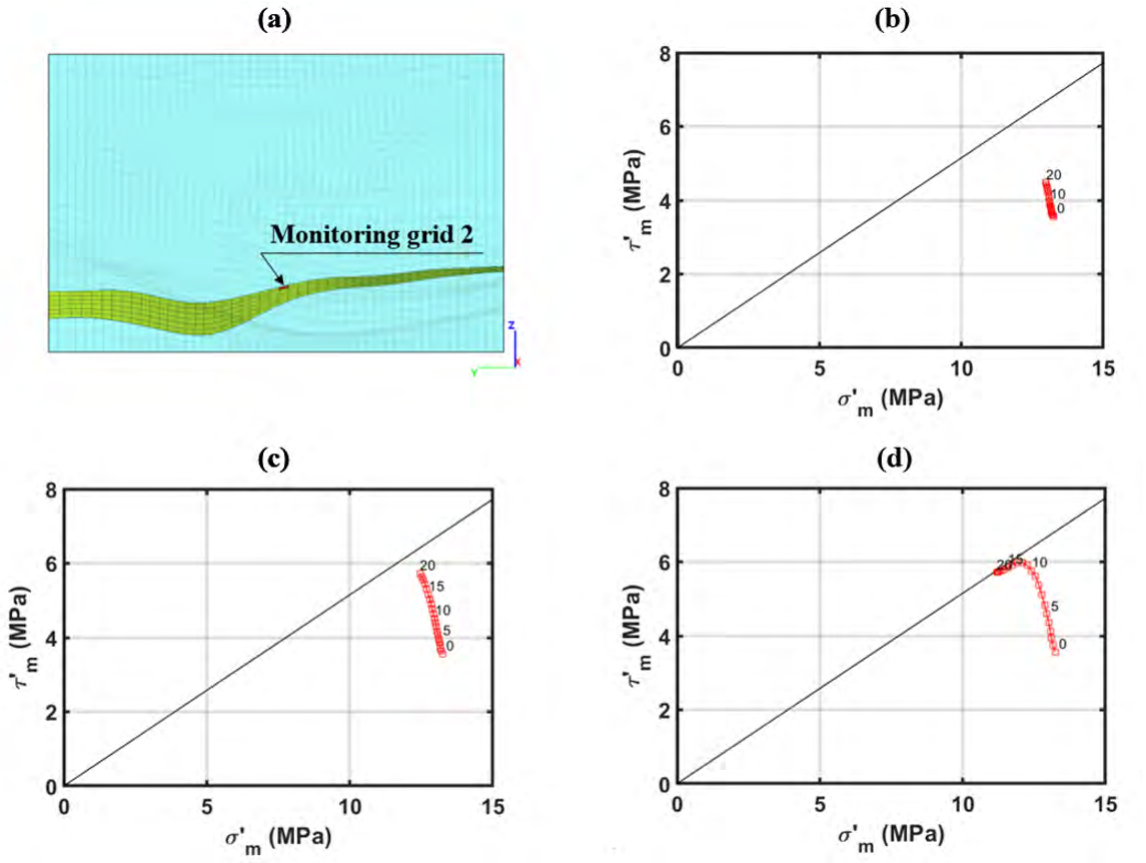

Figure 3.15: (a) A section view of monitoring grid 2 on the fault plane. (b) Change in stress state during CO_2 injection at an injection rate of 50 tons/day, (c) 100 tons/day, and (d) 200 tons/day for 20 years at the monitoring grid 2. Black line indicates Mohr-coulomb failure envelop. Red dotted circles are the evolution of effective stress calculated by using Equation 2.25 and Equation 2.26.

We start discussing post-failure behavior for an injection rate of 200 tons/day first because it presents a clearer picture of fault reactivation and slip. Then, we discuss a lower and higher injection rate to demonstrate how sensitive fault failure behavior is to injection rates. Figure 3.16 and Figure 3.17 show the shear displacement after 5 years and 20 years of injection at a rate of 200 tons/day respectively. In both figures, we have removed all other layers except for the fault plane. The regions at close contact with the reservoir have a greater value in displacement and a lower value in friction coefficient. The friction angle/coefficient varies

between static and dynamic values based on the slip distance because of the adaptations in the shear strain weakening friction law integrated into the study as discussed before. The friction coefficient starts from a static value of 0.6 which gets smaller as the fault shows the shear displacement. When the shear displacement goes over the critical distance of 5.0E-04, in this case, we assume a dynamic friction. value of 0.3. As can be seen in the 5 years injection case,

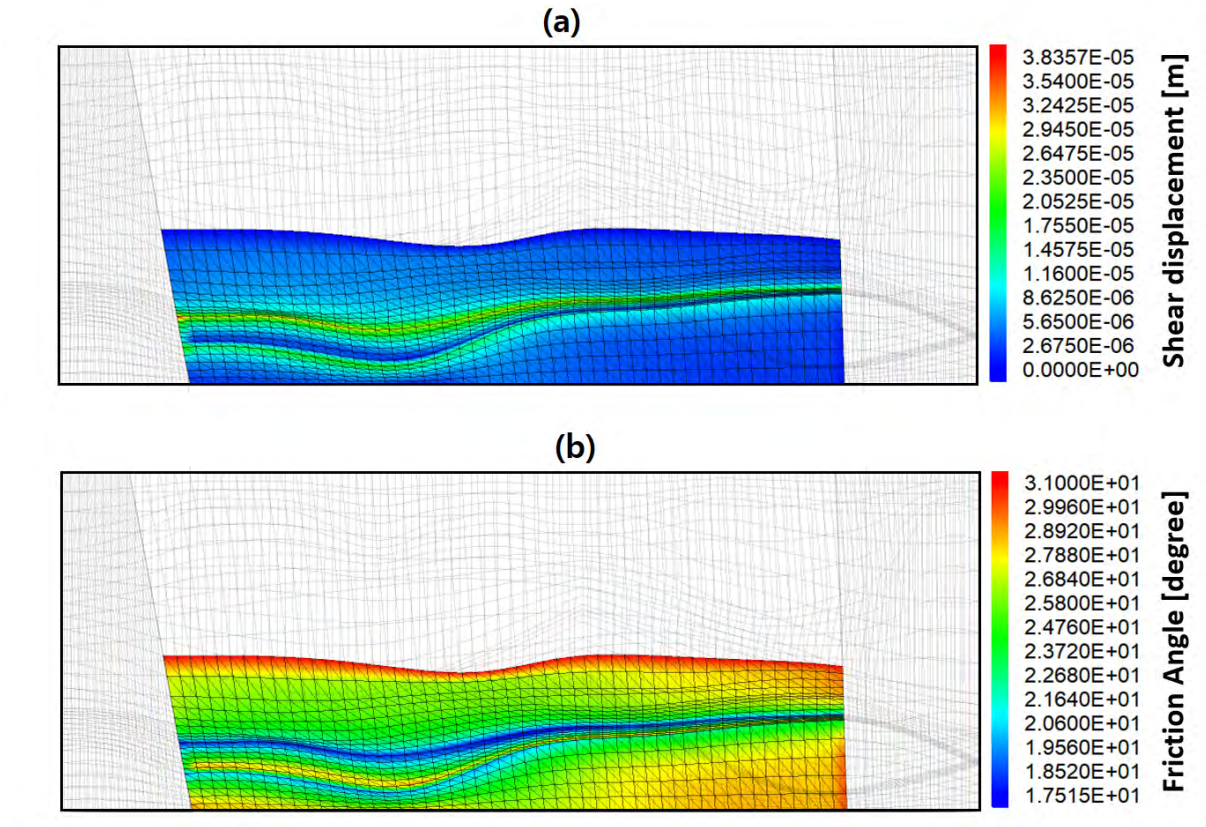

Figure 3.16: (a) Shear displacement and (b) friction angle on fault core (interface element) after 5 years CO_2 injection with 200 tons/day.

some areas in the domain shown in Figure 3.16 are already in slip behavior, however, a larger portion of the areas slip with dynamic friction values. In particular, the greater displacement

is observed right above and below the reservoir formation since the reservoir is expended with fluid injection.

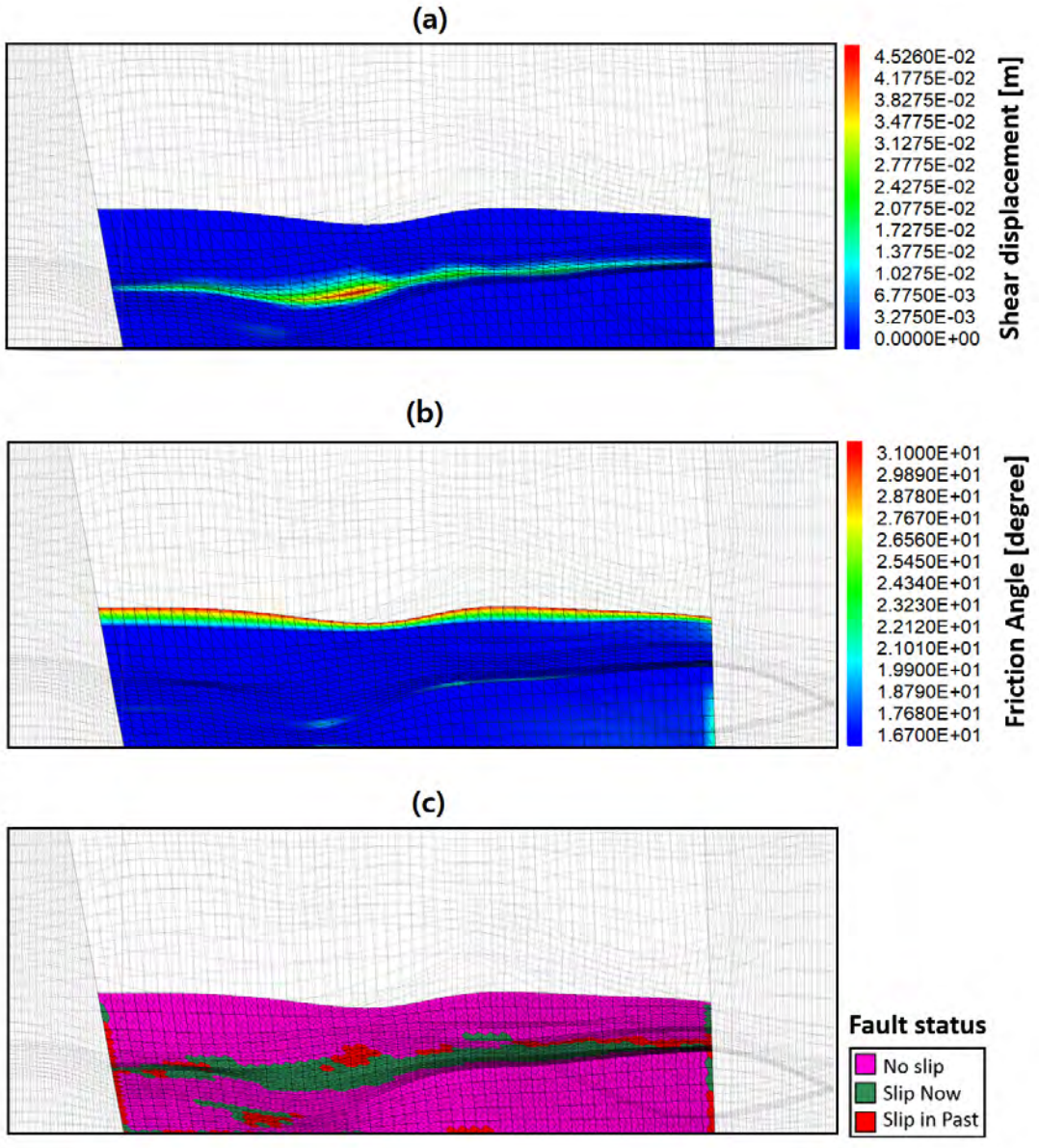

Figure 3.17: (a) Shear displacement, (b) friction angle, and (c) slip status on fault core (interface element) after 20 years CO_2 injection with 200 tons/day

Figure 3.17(c) shows the area of the fault plane that are or were in slip behavior during the injection period of 20 years. Furthermore, the magnitude of seismic moment can be estimated using a widely-used equation in seismology research from Kanamori [114]. The calculated values are listed in Table 3.6. The magnitude scale of the seismic events are calculated as follows,

$$M_w = \frac{2}{3}\log(M_0) - 6.07 \tag{3.1}$$

$$\text{where} \quad M_0 = A\mu s$$

where M_0 is the seismic moment [N·m], A is the area of the fault that slipped [m^2], and μ and S are the shear modulus/rigidity of the material [Pa] and the shear displacement [m].

	Value	Unit	Ratio
Slip area	266,109	m^2	19%
M_w	2.35974		

Table 3.6: Area of the fault in slip behavior and the calculated value of magnitude scale of the seismic events after 20 years injection with 200 tons/day.

In order to get a better understanding of the processes that occur during failure, we record the property changes with time at the location which seems to be the most critical. The monitoring point that has the maximum shear displacement is a grid point with the shortest distance from the injection point shown in Figure 3.18(a). The first three values, viz. friction angle, shear displacement, shear stress evolution, are recorded at this monitoring node with time.

Additionally, a possible seismic magnitude scale over the entire fault plane is recorded in Figure 3.18(b). The results clearly show that displacement and failure along this node on the fault occurs 5 years. We notice that there is a noticeable time gap between the initiation of the seismic event over the entire fault plane and the observed slip at the chosen monitoring node. This can only be indicative of fault slip beginning at other nodal points apart from the one chosen by us for monitoring. Note that the presence of seismic activity (expressed in terms of seismic moment magnitude) is by itself a better indication of fault activation given it is calculated over the entire fault plane instead of the outcomes from a particular nodal point (as is the case with friction angle, shear displacement, shear stress evolution and slip velocity)

The easiest indicator of fault initiation at the monitoring node is the value of the friction angle which continually changes when it is static until the threshold values are reached. It is worth noting that the displacement before activation has non-zero values of less than 5E-04 m. Following reactivation of the fault, the grid blocks between the damage zones are activated which therefore start moving apart. Thus, the shear displacement following activation is much larger than the values observed before activation. We notice that the stress values become smaller (more negative due to compression) with time before fault activation, which starts increasing following fault slip as we let the slip process dissipate the accumulated stresses. Calculating seismic magnitude using Equation 3.1, we can also further confirm that fault begins to slip around 5 years of CO_2 injection. To see the results with a different perspective, we can analyze the plot of Figure 3.18(b) differently using slip velocity in place of shear displacement and the change in seismic magnitude in place of the value of seismic magnitude itself. The resulting plot at each time step is shown in Figure 3.18(c). There are peaks/spikes

in slip velocity which we conclude is clear evidence of a- and co-seismic moments, which are terms used to differential fault slip based on whether they are associated with actual major seismic occurrences. When there is a relatively stable slip velocity in the absence of any major seismicity, it means a-seismic. With an assumption that the fault is activated after the 20 years CO_2 injection, we expect seismic events at a scale of 2.4 in magnitude.

3.3.4.3 Injection Rate sensitivity

As mentioned before, the net injected amount of CO_2 in the system over the estimated duration of the CCS project is intrinsically linked to the mass injection rate of CO_2 into the system. In this section, we compare the results of varying injection rates of 100, 200 and, 400 tons/day to contextualize the importance of this quantity to project life and success. In Figure 3.19, we track the evolution of principle effective stresses (σ'_m and τ'_m) for these injection rates at a monitoring gridblock located in the fault damage zone. Note that a node represents points on cell face located on the interface but a gridblock in this case represents a cell sharing located next to the interface. As is evident from the plot in Figure 3.19, all three injection cases follow similar paths in terms of stress evolution, however, the end points (dots in the plot) reached by each over the project life of 20 years differ, this is because stress generation in the geological system is proportional to the total injection amount, thus the end point of 400 tons/day injection demonstrates the greatest change. In other words, the highest injection rates cause the greatest amount of slip following fault activation. The general curvature of this plot is dependent on how stresses evolve due to injection-induced pressurization until fault slip starts.

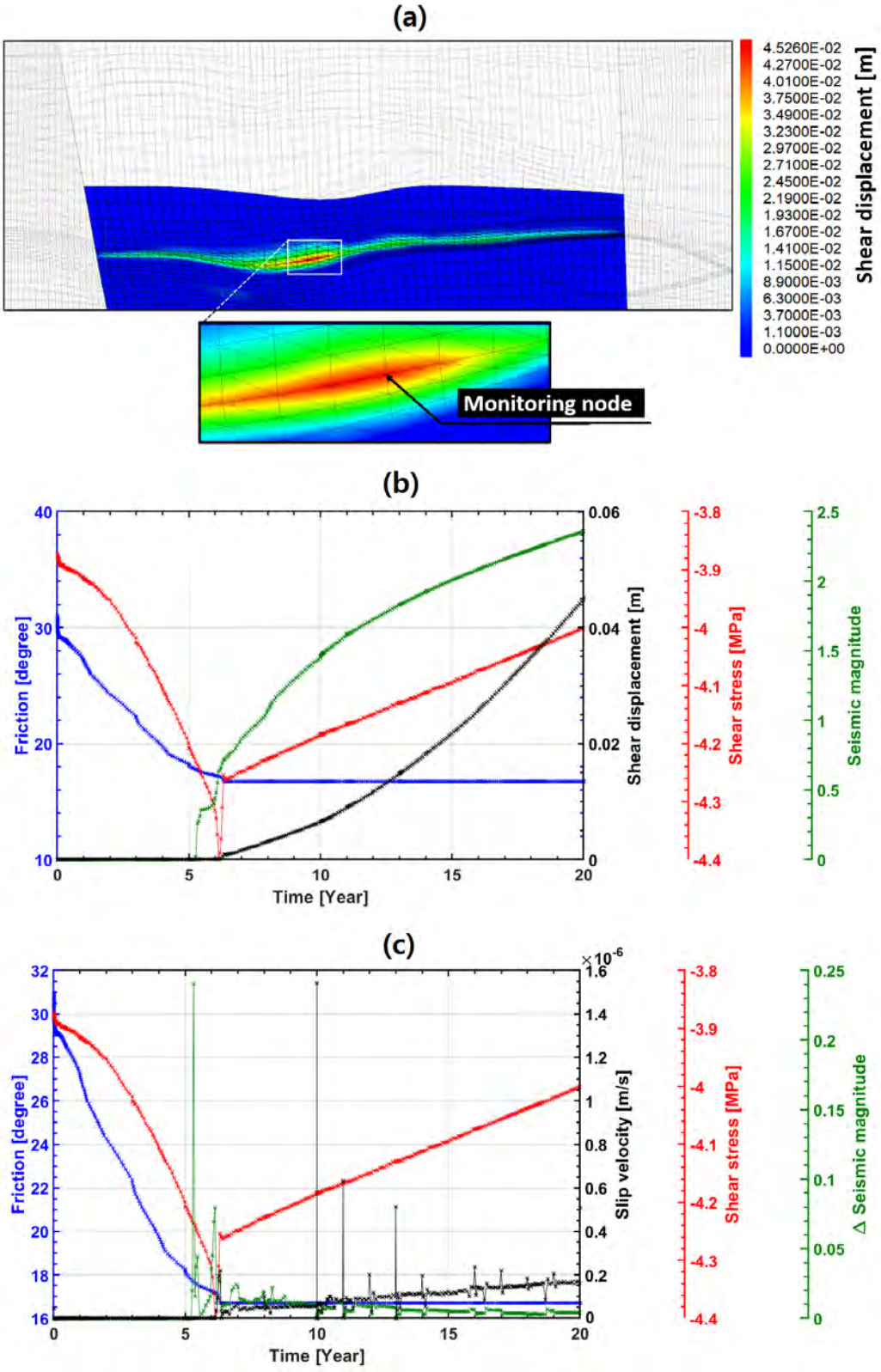

Figure 3.18: (a) Shear displacement and location of the monitoring point, (b) friction angle, shear displacement, shear stress evolution, and possible seismic magnitude scale with time, and (c) friction angle, shear slip velocity, shear stress evolution, and changes in seismic magnitude scale between the time steps on fault core after 20 years CO_2 injection with 200 tons/day

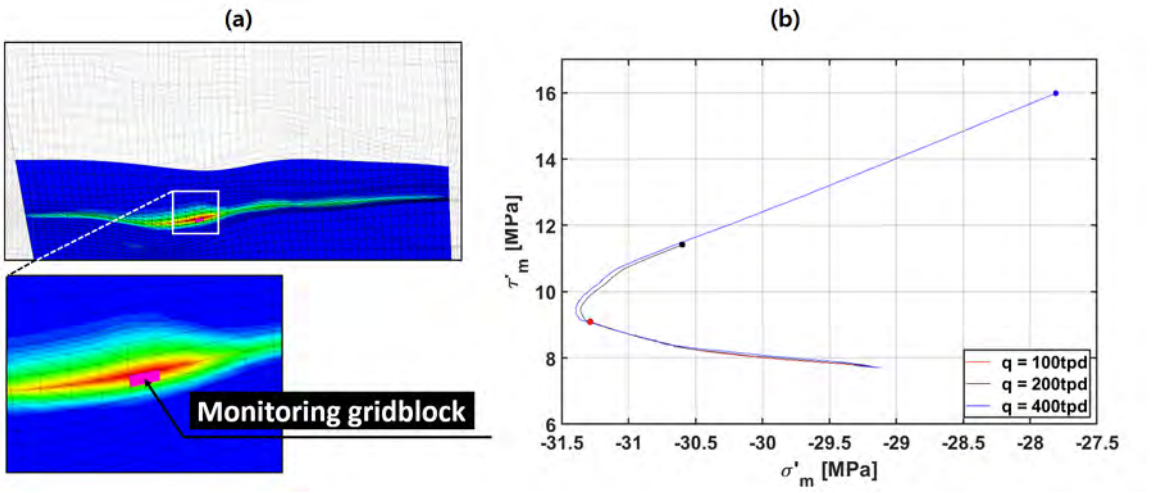

Figure 3.19: Stress evolution with time for 20 years CO_2 injection with 3 injection rate, 100 tons/day, 200 tons/day, and 400 tons/day at the monitoring gridblock

Figure 3.20, Figure 3.21, and Figure 3.22 show the fault slip status and the shear displacements (under a cutoff value of 5E-4 m representing the critical distance of slip weakening law) for injection rates of 100, 200 and, 400 tons/day, respectively. The red regions in these figures represent areas that the friction reaches its dynamic value. Both the area of fault slip and of shear displacement over critical distance becomes larger with an increase in the rate of injection and also over time for each injection case as the total amount of fluid injected into the system increases. Table 3.6 in the previous section listed the area of the fault in slip as well the magnitude of the estimated seismic moment at an injection rate of 200 tons/day after 20 years. Similarly, Table 3.7 and Table 3.8 lists the same for injection rates of 100 and 400 tons/day, respectively. As can be seen from the data in these tables as the injection rate increases from 100 to 400 tons/day the fault slip area also increases from 6% to 48% of the entire fault plane. A similar trend is also observed with increasing rates in the estimated magnitude of

the seismic moment from 1.46 to 3.11. This being in congruence with the results presented in Figure 3.19 which shows the evolution of effective stresses for each rate due to injection. As mentioned before, fault reactivation occurs in either aseismic- or seismic-slip modes, where the differentiation between each is based on whether the associated slip is capable of inducing micro-seismicity and occasional 'felt' seismic events (M_w > 3.0). For both injection rates of 100 and 200 tons/day the seismic magnitude always stays within the threshold for aseismic slip conditions, however, for an injection rate of 400 tons/day this threshold is crossed, and thus there is a very high likelihood for minor earthquakes occurring due to injection. At injection rates of 100, 200 and, 400 tons/day, the fault is expected to get activated at about 3, 5, and 9 years, respectively as can be seen in both Figure 3.23 and Figure 3.24. It is worth noting that the estimated magnitude of seismic events is based on the assumption that there is no flow along the fault even after the fault is reactivated. If there is a flow through the damage zones after reactivation of the fault, the results could be significantly different.

	Value	Unit	Ratio
Slip area	86,590	m^2	6.2%
M_w	1.45940		

Table 3.7: Area of the fault in slip behavior and the calculated value of magnitude scale of the seismic events after 20 years injection with 100 tons/day.

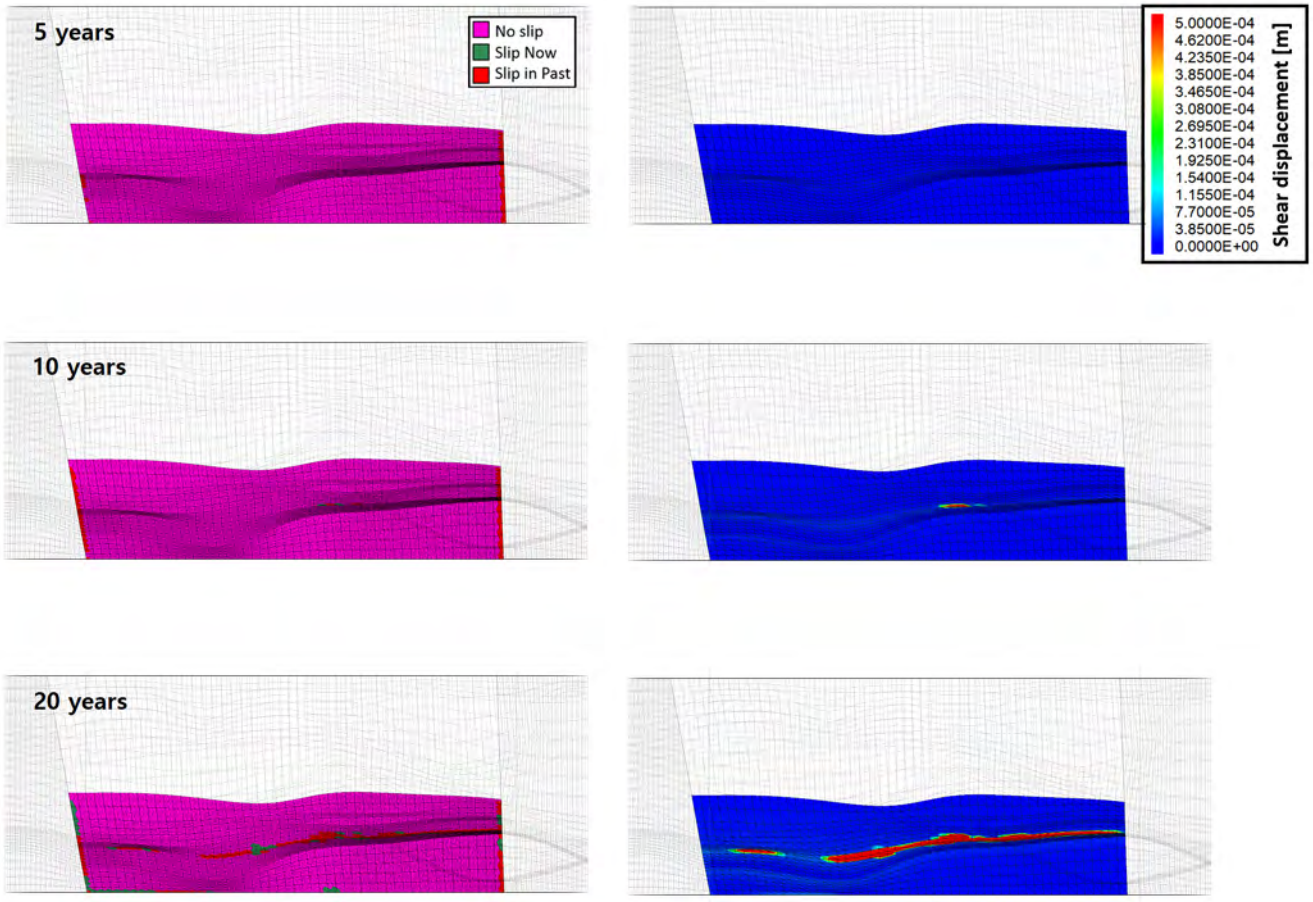

Figure 3.20: Slip status on fault core (1st column), shear displacement (2nd column) after 5 years (1st row), 10 years (2nd row), and 20 years (3rd row) of CO_2 injection with 100 tons/day

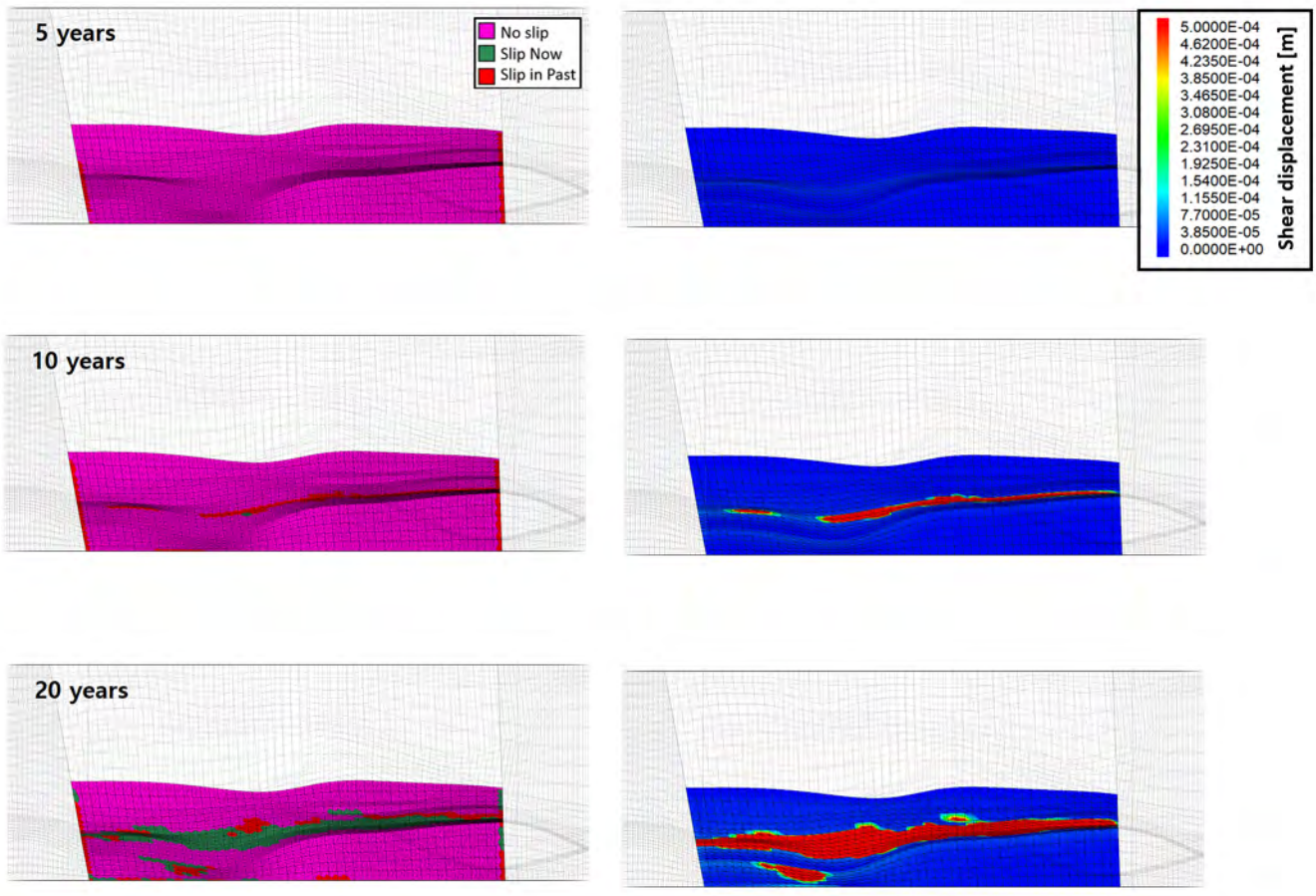

Figure 3.21: Slip status on fault core (1st column), shear displacement (2nd column) after 5 years (1st row), 10 years (2nd row), and 20 years (3rd row) of CO_2 injection with 200 tons/day

	Value	Unit	Ratio
Slip area	675,095	m^2	48.4%
M_w	3.11187		

Table 3.8: Area of the fault in slip behavior and the calculated value of magnitude scale of the seismic events after 20 years injection with 400 tons/day.

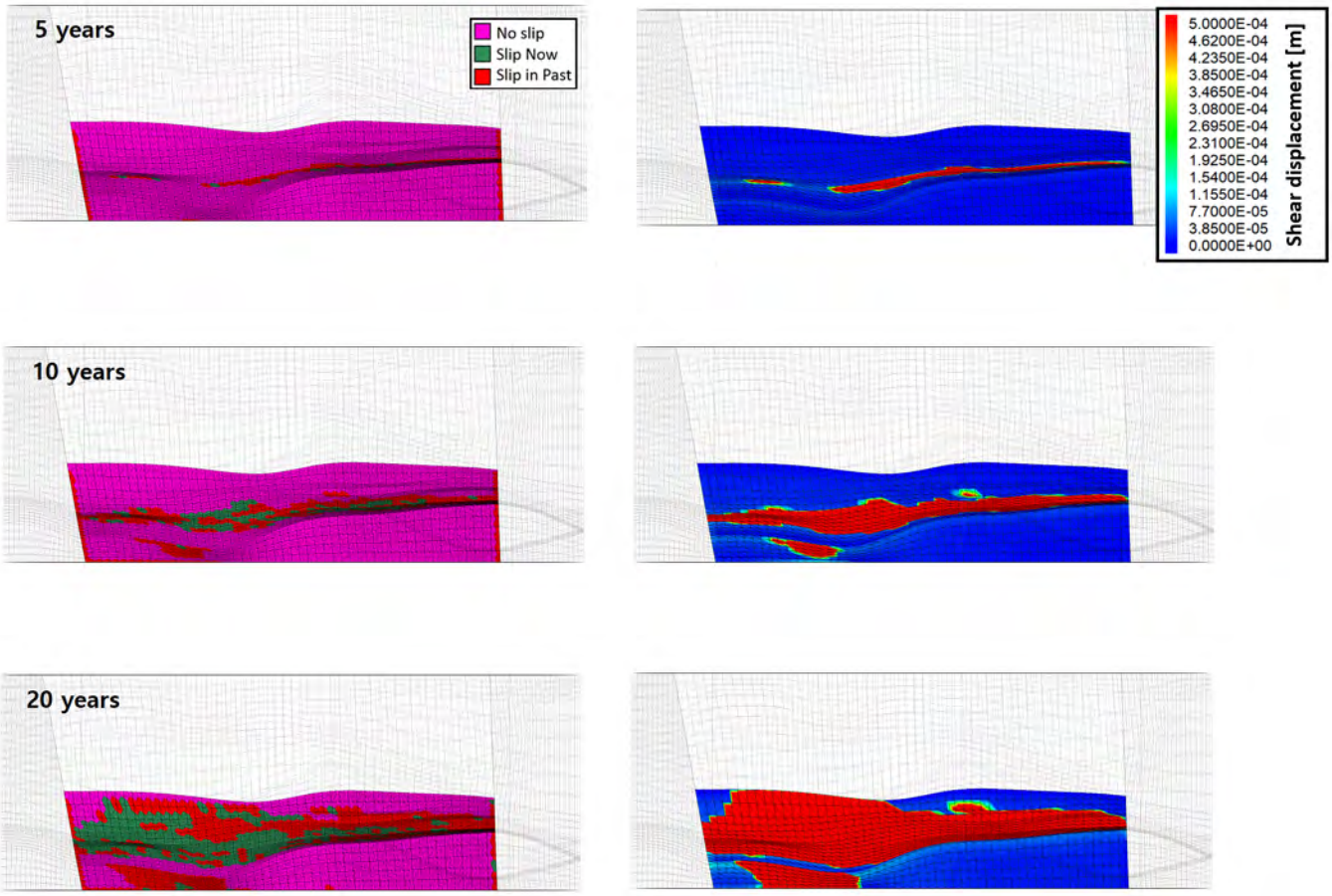

Figure 3.22: Slip status on fault core (1st column), shear displacement (2nd column) after 5 years (1st row), 10 years (2nd row), and 20 years (3rd row) of CO_2 injection with 400 tons/day

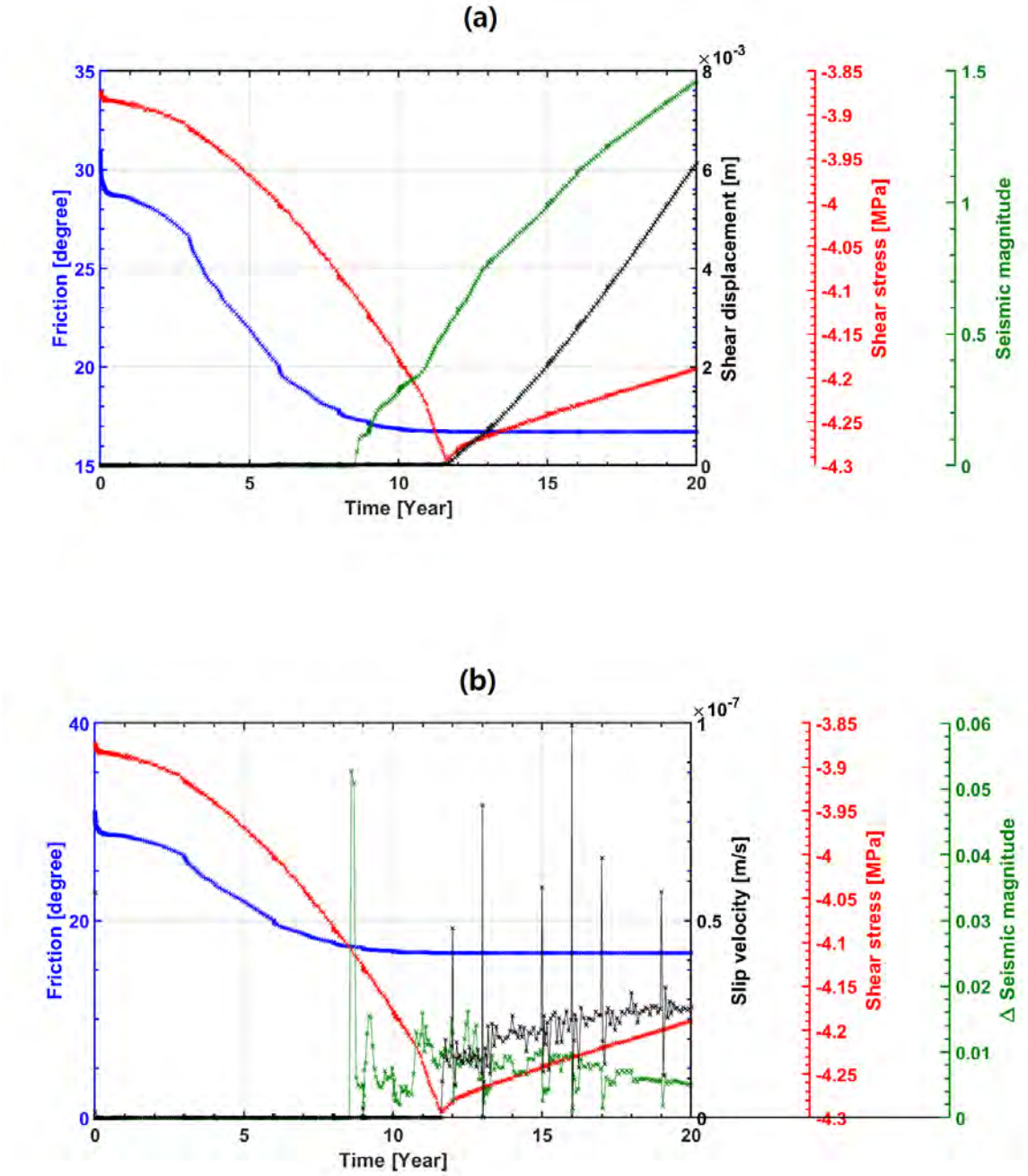

Figure 3.23: (a) Friction angle, shear displacement, shear stress evolution at the monitoring gridblock, and possible seismic magnitude scale with time and (b) friction angle, shear slip velocity, shear stress evolution, and changes in seismic magnitude scale between the time steps on fault core for 20 years CO_2 injection with 100 tons/day

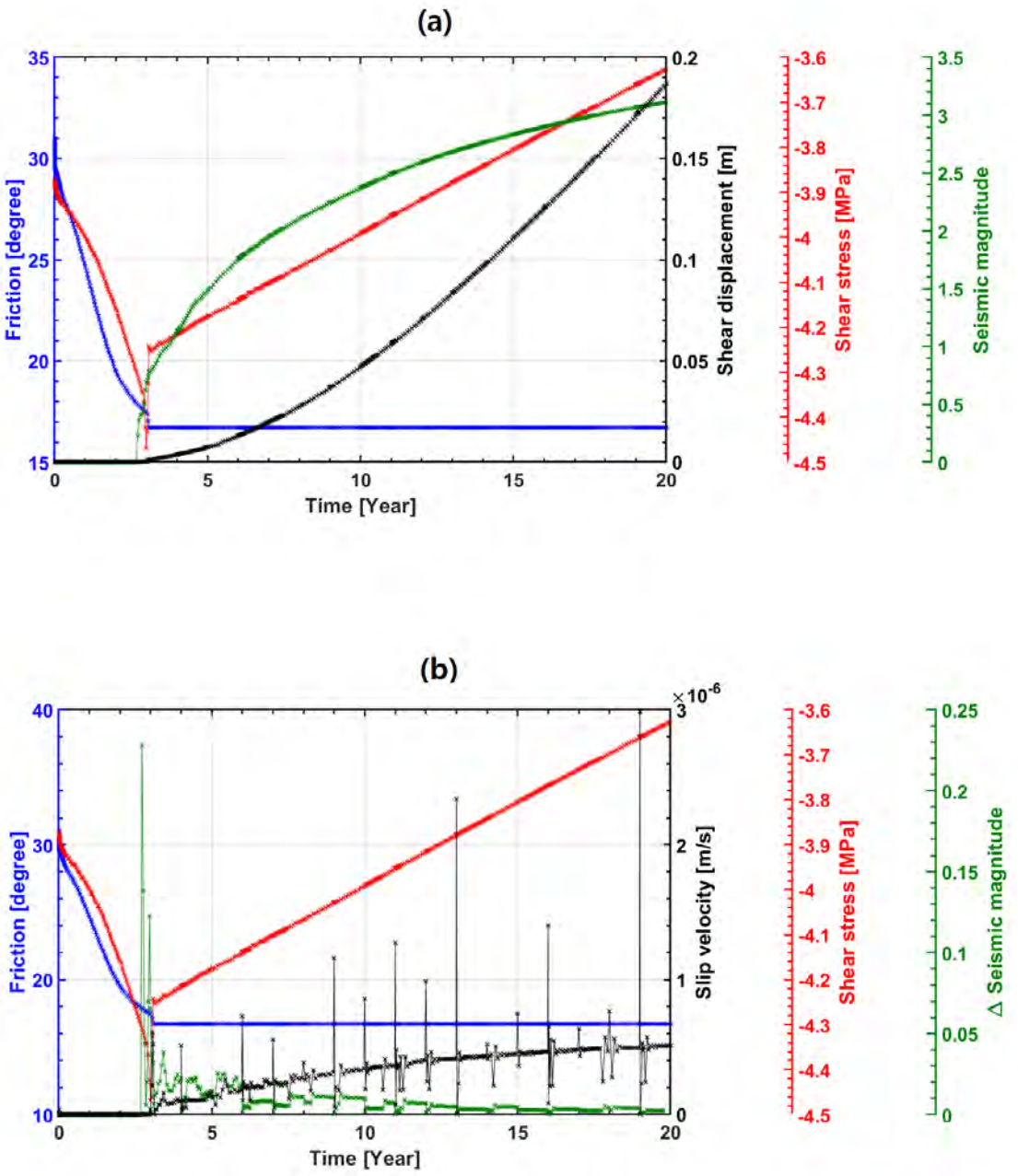

Figure 3.24: (a) Friction angle, shear displacement, shear stress evolution at the monitoring gridblock, and possible seismic magnitude scale with time and (b) friction angle, shear slip velocity, shear stress evolution, and changes in seismic magnitude scale between the time steps on fault core for 20 years CO_2 injection with 400 tons/day

3.4 Conclusion

The study provides a perspective on the injection rates that are feasible for the successful implementation of the pilot-scale CO_2 storage project that was initiated in the Janggi sedimentary basin located in Southeast Korea. The major portion of the study looked at the potential activation of the normal fault that was identified close to the injection well from geophysical surveys. To estimate the maximum sustainable injection pressure for geological CO_2 storage, we performed numerous numerical simulations and conducted fault-slip analyses using two-way coupled flow and geomechanics numerical approaches. Before conducting any detailed study, we validated the flow simulator with an existing well-known simulator. Then, we used well-known analytical solutions to see whether the coupling method is accurately applied (McNamee and Gibson's problem). To model the fault reactivation and slip behavior, we took two different approaches, Mohr-coulomb model and discontinuous surface with zero-thickness elements. With Mohr-coulomb failure mode, we assessed 3 different injection scenarios, 50, 100, and 200 tons/day. The results showed that the CO_2 injection at a rate less than 100 tons/day is most sustainable judging by the evolution of stress at gridblocks that were at the greatest risk of failing. At this storage site, CO_2 injection into the reservoir induced a significant amount of ground surface uplift occurred even before the reservoir pressure reached the maximum sustainable pressure that could initiate fault reactivation. The excessive surface uplift can cause damages to surface infrastructures and potentially lead to increased microseismic events with continuous injection. To study this further, we employed a discontinuous surface approach to simulate the fault behavior with interface elements. We observed similar results at an injection rate of 100, 200, and 400 tons/day of CO_2 using this approach. This

approach enables us to measure the estimated magnitude of seismic events and identify the a- and co- seismic events by plotting the slip velocity over time at the monitoring node. In view of potential risks and hazards of fault reactivation and slip, surface uplift can be used as an indicator in determining the total CO_2 injection duration because the surface uplift is related to the reservoir pressure and has a direct influence on the initiation of fault reactivation.

4. PREDICTING FLOW AND GEOMECHANICAL RESPONSES DURING CO_2 INJECTION IN GEOLOGICAL STORAGE USING DEEP-LEARNING BASED SURROGATE MODELS

The previous chapter has investigated the capability of our coupled flow and geomechanics simulator by using it to study a pilot-scale CO_2 storage project to aid the process of making inferences on injection scenarios that may or may not lead to fault activation and slip. The use of such a simulator for a variety of purposes including injection-induced pressurization of subsurface reservoirs is a very computationally intensive process. Simulations based on any range of possible model fidelities can take a long duration irrespective of the computing systems they are being run on.

Our goal in this section is to use a deep-learning-based surrogate model to treat coupled flow and geomechanical response with CO_2 injection in geological storage with different realizations of permeability, porosity distribution, and injection rate. We expect that the surrogate model will be used in the estimation of gas saturation and pressure distribution based on the surface displacement.

4.1 Convolutional Neural Network

The core idea behind developing a surrogate model is to use it as a proxy model that eliminates the need of making multiple time-intensive simulation runs for creating a forward model. The creation of the surrogate model is aided by using a deep-learning based procedure called 3D U-Net model (that uses deep convolution neural networks). Convolutional Neural

Networks (CNN) are a class of artificial neural networks specifically designed to work on pixelated data due to their ability to recognize and process visual imagery. These deep learning algorithms can take inputs (say an image), assign importance (i.e., weights and biases that can be learned) to aspects of interest (maybe objects, anomalies, etc.) in the input to differentiate or identify them. The basic idea is to replicate how neurons in the eye create the sensory perception of real-world surroundings. Though not apparent to us, there exists a complex hierarchical structure of neurons and their connections in our brain which makes it possible for us to recognize objects. Note that, in artificial neural networks, a neuron represents a mathematical function that can model the function of a biological neuron, typically by using a weighted average of the input, whose sum is passed on through some non-linear function (also called activation functions) to new layers. Analogous to biological sensory perception, CNN algorithms try to implement a workflow using numbers where it trains on umpteen number of pictures/input data to learn just how children learn to recognize facets of their surroundings by experience. Regular neural networks transform inputs by putting it through a series of hidden layers where every layer is made up of a collection of neurons and every layer is connected to the neurons from the layer before. However, in CNNs this flow changes, neurons in one layer do not connect to neurons in all layers but only to a small portion of it. For this, when CNNs are applied they employ progressive filters within layers to extract feature maps (called convolution operations) that essentially transform data. Once successive such operations are completed, we in a broad sense put in place a classification and output scheme to complete the process. It is this flow of operations that separates it from RNNs and other neural networks.

CNNs can interpret visual data or data that do not have a sequence; however, they may

often fail when the temporal dimension is added. The main difference between CNNs and methods like RNN is its ability to process data that come in sequences and each method is used for completely different purposes.

4.1.1 3D U-Net

Convolutional networks have often had the issue of training data set size and the size of considered networks. To address this issue in fully convolutional neural networks, U-net was developed. The input may be data with images with 2 spatial dimensions, 3D volumetric data (3 spatial dimensions), or videos (2 spatial and 1 temporal dimension). Originally invented for biomedical image segmentation (the term itself means locating areas of interest in an image), its architecture is so designed that it can work with fewer training images and is able to yield more precise segmentation. It consists of a contracting path where the input is progressively encoded to extract features and an expanding path where decoding is done using upsampling, this gives it the classical u-shaped architecture that is associated with its name. The contracting path or encoding path in a U-net involves the repetitive application of convolutions followed by a rectified linear unit (ReLU) and a max-pooling operation while reducing spatial information and increasing feature information, this increases contextual information or the receptive field while reducing the resolution. The expansive or decoding pathway applies upsampling using transposed convolutions to combine feature and spatial information i.e., it consists of a sequence of up-convolutions and concatenations with high-resolution features from the contracting path. Thus, it is from start to end a fully convolutional network. Now, for geological surrogate models since the sample is a 3D distribution of properties, implementation of the U-Net with 3D convolution is most appropriate. Thus, we have used 3D U-Net for our case.

Note that, the number of dimensions in which the kernel operates during convolutions is what defines the dimensional prefix of U-Nets.

4.1.2 Primer on U-Net based CNN architecture

We believe that the reader with an interest in the field of coupled flow geomechanics might not come with a background to understand the entire U-Net based Convolutional neural network workflow which we implemented to develop the surrogate model. In this section, we try to cover all the terms that are of importance in understanding the workflow. The idea is to make sure the often-repeated terms are aptly clear when referred to. We approach this problem by dealing with it from a standpoint of covering terminology of increasing complexity to make sure every concept is clear

- Convolution Layer:

  In this step, the input image/data/matrix is subject to the application of a filter (also called a kernel/feature extractor) to extract features within the input data. The two major components are:

  - An Input volume which is a 2D or 3D Matrix (maybe, $N_{in} \times N_{in} \times channels$) or a 4D tensor (maybe, $N_{in} \times N_{in} \times N_{in} \times channels$) etc. where N_{in} is the number of input features and $channels$ represent the class of inputs that are being fed.
  - A set of 'i' filters/feature extractors each having a size of $f \times f \times channels$, where dimensions in f may be added based on the spatial dimensions of the input. Note that, f is typically 3 or 5. The dimension in f is determined by the degrees of freedom in terms of the movement of the kernel along the input matrix and the

size of input data. So, for 3D convolution, there are 3 Dimensions in f. These filters are used to extract features of interest in the input volume.

- Kernel:

  The term kernel was used a lot of times in the definition of convolution, it is a matrix that moves over the input data, and which performs a dot product with a sub-region of input data. The kernel moves over the data with a particular stride and the input data itself may or may not have a pad based on the need to preserve matrix size. The term stride (s) refers to the amount by which the filter moves over the input matrix as it performs operations(dot product) in it. The term pad (p) refers to the layer of zeros added along the sides of the input matrix depending on whether the size of the input matrix needs to be maintained.

  A simple convolution operation with filter is shown in Figure 4.1 with a single channel 4×4 input using a 3×3 filter where the kernel moves with a stride of 1 and the input matrix has a padding of 1 to maintain the same size while the size of feature map or 0 which reduces matrix dimensions from w to $w - 2$. There is the key distinction that needs to be elaborated here, the term filter and kernel may be used interchangeably, in a general case which consists of a single channel of input. However, these terms are very different, each filter is a collection of kernels, with there being one kernel for every single input channel, and each kernel being unique. Each filter in a convolution layer produces one and only one output channel which is called a feature map (Figure 4.2). There might be multiple channels generated by the application of multiple filters to the

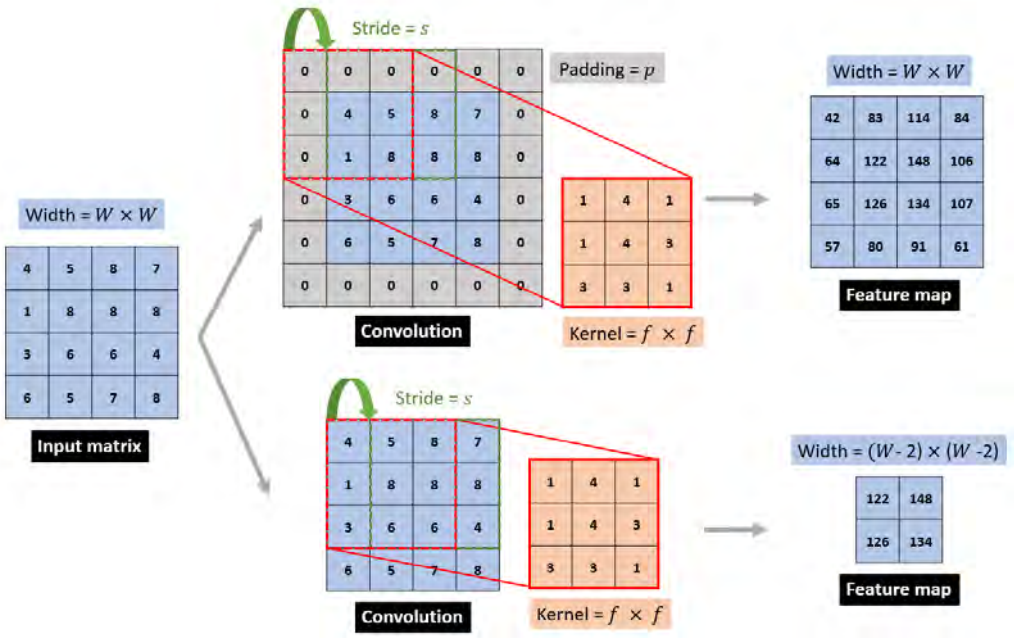

Figure 4.1: Convolution and its components, width (W), stride (s), padding (p), and kernel (f).

input volume in a convolution layer. The filter in itself is spatially small, but it extends through the full depth of the input volume. Also, there might be multiple convolution layers where each convolution acts upon pooled and rectified feature maps from the preceding layer, where the cumulative interaction of the prior convolutions accentuates the complex features within the original input volume due to filters being applied.

- Receptive Field:

  The receptive field is used to define the region in the input space that affects a particular unit of the network, i.e., it is a measure of the association on the output feature to an input. In this case, the term 'input region' does not only include the input of the entire framework of the network but also output from other units in the network. The receptive

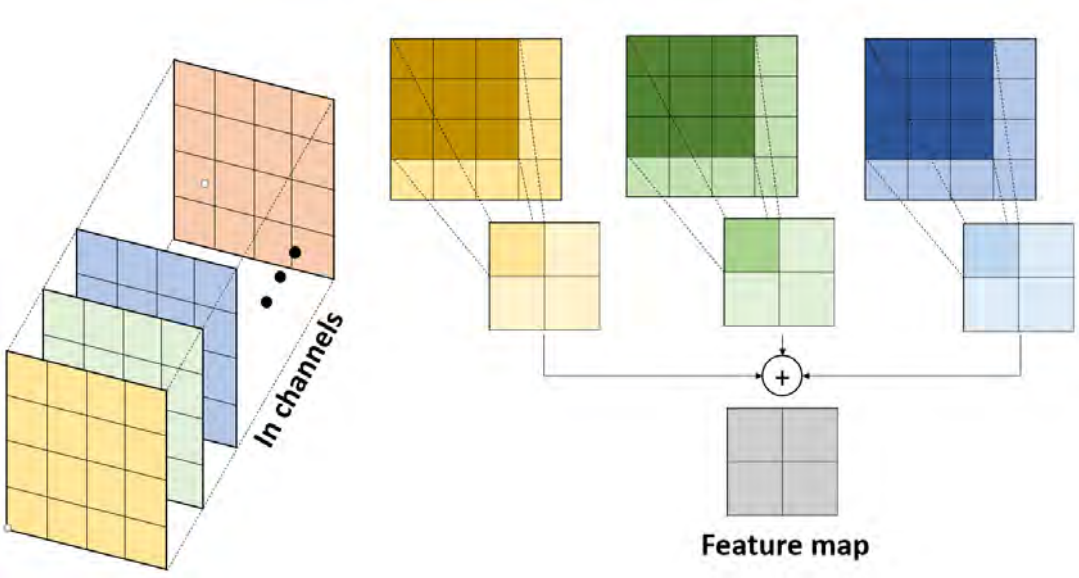

Figure 4.2: Schematic diagram for the concept of filter, kernel, and channel. The filter is a collection of kernels and each kernel of the filter moves over its receptive channels to produce each feature map. Each of the per-channel feature maps is summed to be the single channel.

field is controlled by the striding and padding during filter application.

- ReLU (Rectified Linear Units):

  Normally after each convolution layer, it is the convention to add non-linearity immediately afterward since the convolution layers just involve linear operations, i.e., the inputs are multiplied by weights and then summed together. The summed result in the feature map is called the activation of that node, this is then transformed using an activation function which further defines the specific output or the "activation" of that node. Nonlinear activation functions enable the learning of more complex structures in the data. Such an operation is also called a non-linear layer or activation layer. The ReLU activation is a piecewise linear function that involves applying a simple a function $f(x) = \max(0, x)$, to all the values of the output of the convolution layer, i.e., the

function converts all negative terms within convolution output to 0. Thus, it increases the non-linear properties of the model and the network without affecting the receptive field of the convolution layer.

- Max pooling operation:

  Max-pooling is aimed at reducing the size and down-sampling the feature map produced after the transformations done during convolution. Thus, it results in fewer parameters in the network. The idea is to only retain information which best describes the context of the input, i.e., as in this case, only the important features (max valued pixels) from each region are retained and information that is not important is discarded. Depending on stride and padding both convolution and the pooling operation reduce the size of the image. An example is shown in Figure 4.3 where, we basically, select in every 2×2 block of the input feature map, the maximum pixel value and thus obtain a pooled feature map. Note that, the size of the filter and strides are important parameters in this operation. The idea is to convert a high-resolution volume to a low-resolution volume which aids the process of fitting by providing an abstracted form of representation. This step helps prevent over-fitting, i.e., when the model is so tuned to the training examples that it is not able to generalize well when tested on validation and test sets. Thus, when convolution is applied again, the filters in the next layer see a larger context, i.e., as the network gets deeper, the size of the image reduces however the receptive field increases. Typically, in any CNN the size of the volume gradually decreases due to pooling, which lets the filters in the deeper layers work on a larger receptive field but the increase in the number of channels due to the filters used means that more complex features can be

extracted.

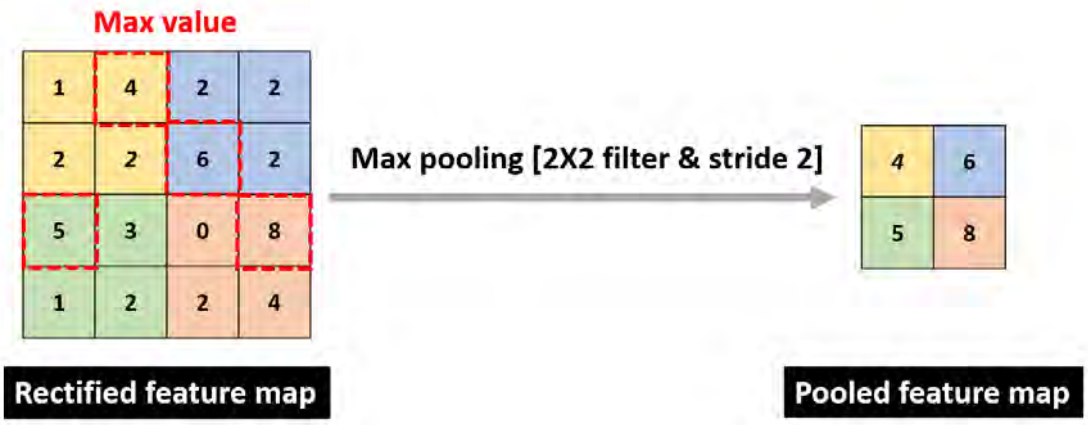

Figure 4.3: Example of max pooling operation with 4 $\times$ 4 feature map.

- Upsampling and Transposed Convolutions:

  The definitions covered in the previous bullet points are related to the encoding layers of a U-Net implemented in this part of the study. The combination of convolutional layers, ReLU and, max-pooling operations result in an output that is smaller than the original input volume as the process causes the loss of spatial information within the receptive field as features within an input volume are extracted. Thus, it is necessary to carry out a reverse operation that mirrors the encoder but upsamples or expands and restores the original size. In U-nets, this is done using a method called Transposed Convolution, which is also known as fractionally-strided convolution or deconvolution. In this case, instead of the many-to-one relationship implemented in the pooling layers a one-to-many relationship is implemented. As mentioned in Figure 4.1, a 3 $\times$ 3 kernel is applied on a 4 $\times$ 4 input to generate a 2 $\times$ 2 output without the padding. However,

during transposed convolutions while maintaining the relationship used during convolution a reverse operation is attempted. It must be noted that the actual weights in the deconvolution matrix are not necessarily the same as the ones used in convolution, the layout of the weights in the matrix is what is most important in this operation.

4.2 Methodology

4.2.1 Numerical Model Setup

We place the reservoir at the depth, -1000 m, and set the thickness of the reservoir, 200 m, which is similar to the geological CO_2 storage model that is used in the previous section. Apart from this, the size of the reservoir used is larger. Here, we also differentiate the geomechanics and reservoir domain to reduce the computational cost. The domain size of geomechanics is 8 km $\times$ 8 km $\times$ 1.5 km (40 $\times$ 40 $\times$ 27 = 43,200 grids) and the reservoir has a domain size of 8 km $\times$ 8 km $\times$ 0.2 km (40 $\times$ 40 $\times$ 12 = 19,200 grids). We make the grids become larger as we move towards the surface and bottom in the geomechanics model as can be seen in Figure 4.4. The thickness of the reservoir layer is Δz = 16.7 m. The initial pressures at the top and bottom of the domain are 11.45 MPa and 13.21 MPa, respectively, and the initial temperature is 45°C as can be seen in Table 4.1. The pressure is distributed linearly from top to bottom with a hydrostatic gradient while the temperature is constant over the domain.

The overall model is structured with 3 zones (reservoir, under-, and over-burden layers) to assign different geological parameters for each zone such as bulk and shear modulus. Poisson's ratio is kept the same (ν = 0.25) for all layers, Young's modulus is set o 3.78 GPa for the aquifer reservoir (same as, 20 GPa for the under-burden, and 1 GPa for the over-burden as

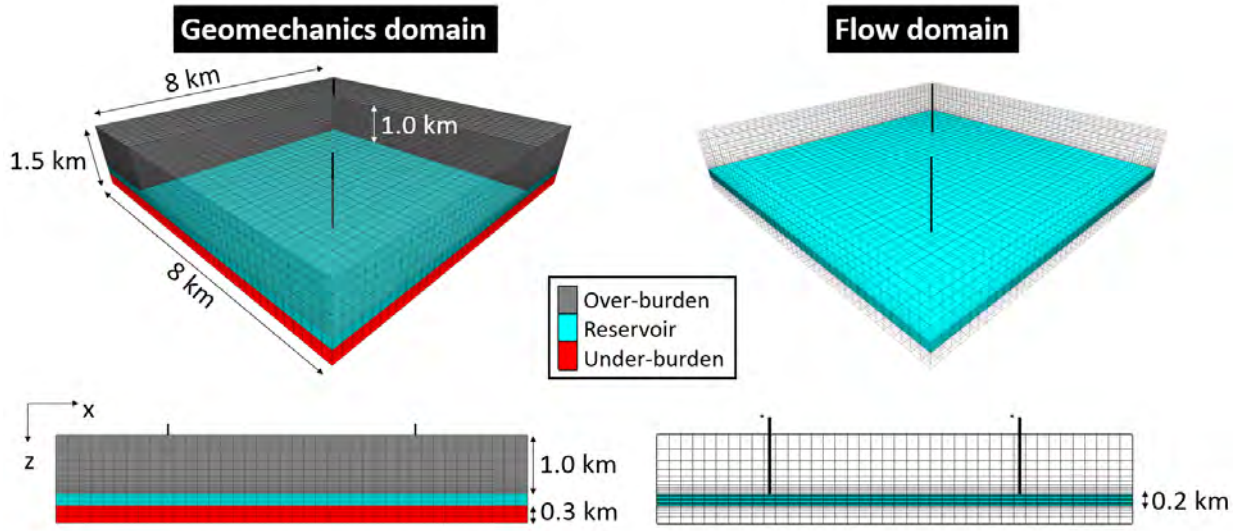

Figure 4.4: Dimension of (left) the geomechanics model based on 3 different types of zones, 43,200 grids and (right) representation of aquifer reservoir with injection well location, 19,200 grids.

Hydraulic properties	
Initial permeability	Gaussian random distribution
Initial porosity	Linearly related to $\log(k)$
Pore pressure at the surface	4.900E+05 Pa
Pore pressure gradient	-9.806E+03 Pa/m
Biot's coefficient	1.000E+00
Boundary condition	No flow
Gas density	O'Sullivan et al. (1983)
Gas viscosity	Pritchett et al. (1981)
Relative permeability	Corey et al.(1954)
Capillary pressure	van Genuchten-Mualem(1980)
Henry's constant coefficient	D' Amore and Truesdell(1988)

Table 4.1: Input parameters of hydraulic properties for numerical simulation

can be seen in Table 4.2. This ensures that the over-burden layers result in relatively greater displacement at the surface with the lower value of Young's modulus. For the initialization of pressure distribution due to overburden, we assign a pressure of about 0.46 MPa at a depth

of 50 m below sea level with a hydrostatic gradient. The stress distribution is also assigned with a gradient that also can be found in Table 4.2. Two injection wells are located diagonally opposite to each other with an assumption of full completion along the wellbore from the top (-1000 m) and bottom (1200 m) layer of the reservoir. We consider 3 different rates of CO_2 injection (1000, 2000, and 4000 tons/day). While we assigned in the previous chapter a homogeneous distribution of permeability (16.7 mD =1.670E-14 m^2) and porosity (12.6 %) over the reservoir domain, the aquifer reservoir hydraulic properties in this study is characterized by Random Gaussian function distribution. The porosity field is generated by using a linear relationship with $\log(permeability)$. Note that the over- and under-burden layers are assumed to be impermeable. For the boundary condition, we consider a no-flow boundary at all the sides of the domain while a roller boundary is assumed for the geomechanics model.

4.2.2 Surrogate Model

We generate 240 realizations with Random Gaussian distribution of permeability with a mean of 16.7 and a standard deviation of 10. All the cases are populated with the same parameters except the anisotropy range of variogram as shown in Table 4.3. Every 60 cases have a different value of anisotropy range from 500 to 3000 m as can be seen in Figure 4.5. Based solely on the anisotropy range, when the values for the same are lower, the grid by grid values of permeability show greater contrast in terms of its distribution in space. However, the histogram in Figure 4.6 clearly shows that notwithstanding the grid by grid distribution of permeability based on the anisotropy range, their values considering the entire sample population are still roughly similar.

Figure 4.7 shows the distribution of porosity corresponding to the permeability values

Mechanical properties			
Stress at the surface	x	-1.36E+06	Pa
	y	-9.90E+05	Pa
	z	-1.24E+06	Pa
	xy	-3.13E+05	Pa
Stress gradient	x	2.72E+04	Pa/m
	y	1.98E+04	Pa/m
	z	2.47E+04	Pa/m
	xy	6.26E+03	Pa/m
Lithology 1	Bulk modulus	1.33E+10	Pa
[Under-]	Shear modulus	8.00E+09	Pa
	Density	2.42E+03	Kg/m^3
Lithology 2	Bulk modulus	2.53E+09	Pa
[Reservoir]	Shear modulus	1.52E+09	Pa
	Density	2.32E+03	Kg/m^3
Lithology 3	Bulk modulus	0.67E+09	Pa
[Over-]	Shear modulus	0.40E+09	Pa
	Density	2.27E+03	Kg/m^3

Table 4.2: Input parameters of mechanical properties for numerical simulation

Properties		Value	Unit
Total sill		1	
Nugget		0.1	
Variogram type		Gaussian	
Anisotropy range	Major dir	1000	m
	Minor dir	1000	m
	Vertical dir	100	m
Azimuth		0	
Dip		0	
Data range	min	0.01	mD
	max	100	mD
Distribution		Lognormal	
	Mean	16.7	mD
	std	10	

Table 4.3: Input parameters of first 50 cases for petrophysical modeling of permeability with Gaussian random simulation

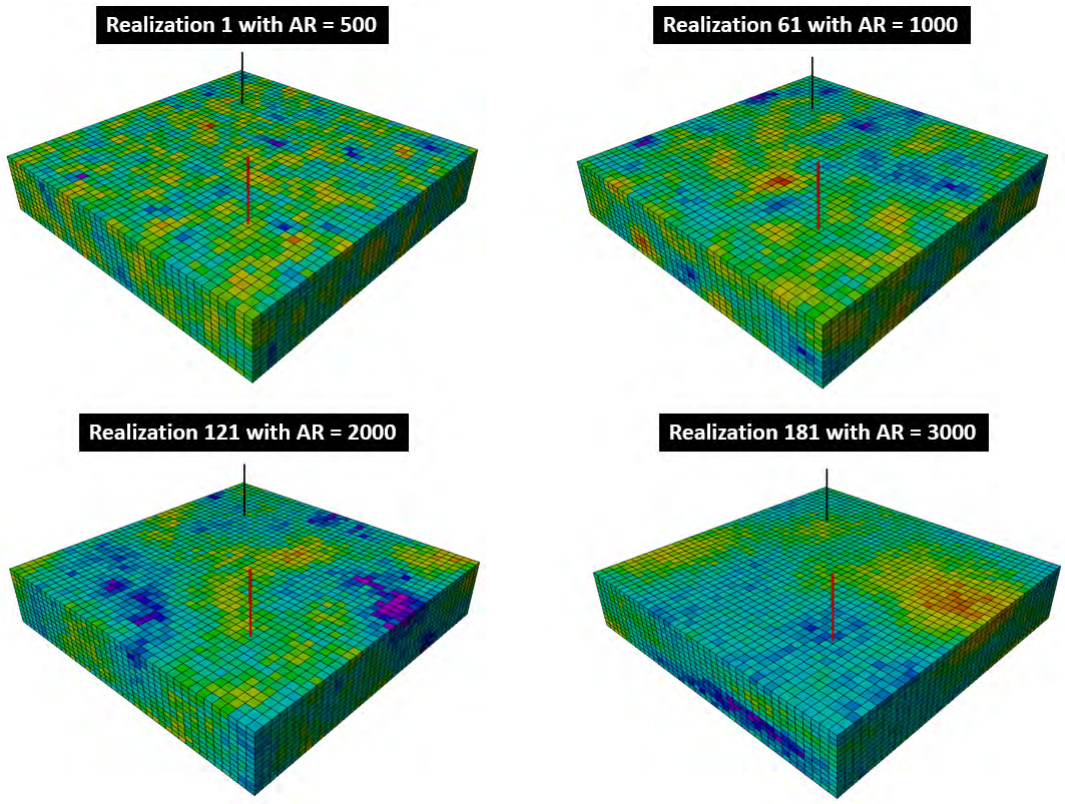

Figure 4.5: Gaussian Random log-permeability realizations over the reservoir. For visualization, the vertical direction is exaggerated by 7.5 times.

under an assumption of a semi-logarithmic relationship between these quantities. The exact relationship between permeability and porosity for the sample population of the domain is shown in Figure 4.8. The resulting porosity distribution has a mean of 0.25 and a standard deviation of 0.015. The spatial distribution of permeability and porosity are interdependent and so only one of these (permeability) is used as an input for developing our surrogate model. The output for pressure, gas saturation and surface displacement in the vertical direction with each permeability realization are recorded 34 time steps (3, 6, 9, 12, 15, 18, 21, 24, 30 ,36, 42, 48 , 54, 60 ,66, 72, 78, 84, 90, . . . ,174, 180 months). The results for the spatial distribution of pressure, gas saturation, and surface displacement after 15 years are shown in Figure 4.9.

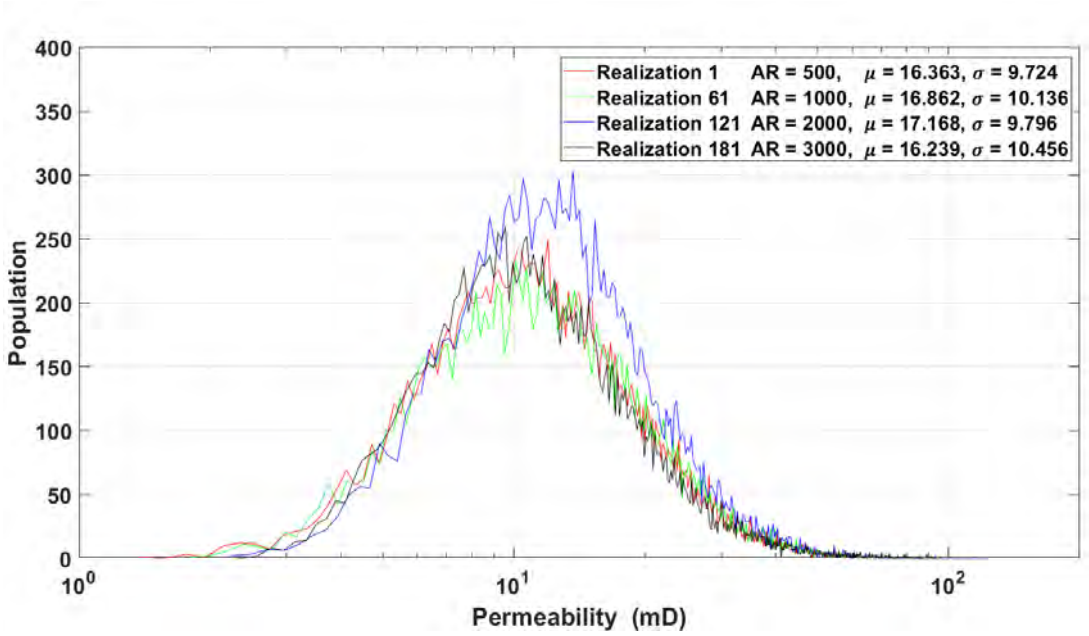

Figure 4.6: Histogram of permeability and its estimates (mean, μ and standard deviation, σ) of 4 sample representation cases shown in Figure 4.5.

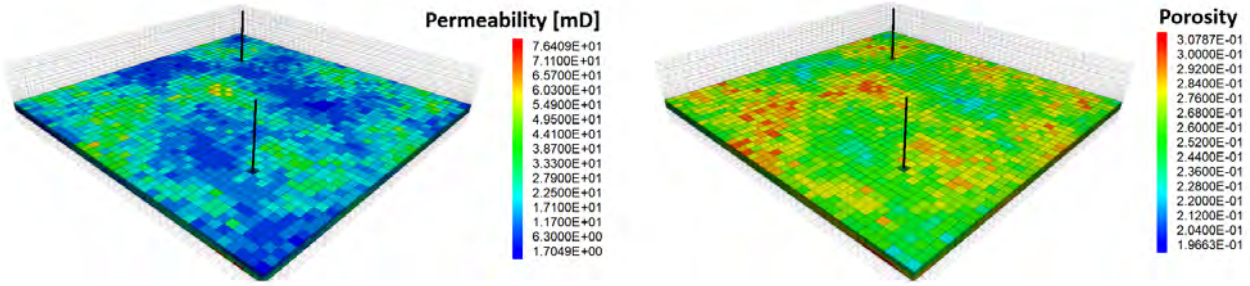

Figure 4.7: Example of permeability and porosity distribution (Input data set), which are correlated each other.

4.3 Model training with 3D U-Net Architecture

Before using a 3D U-Net, we need to re-sample the data to convert the unstructured grids to structured grids. The processes of re-sampling the data are done using the VTK format. Among all the input-output sets, the surface displacement are the only point data while the

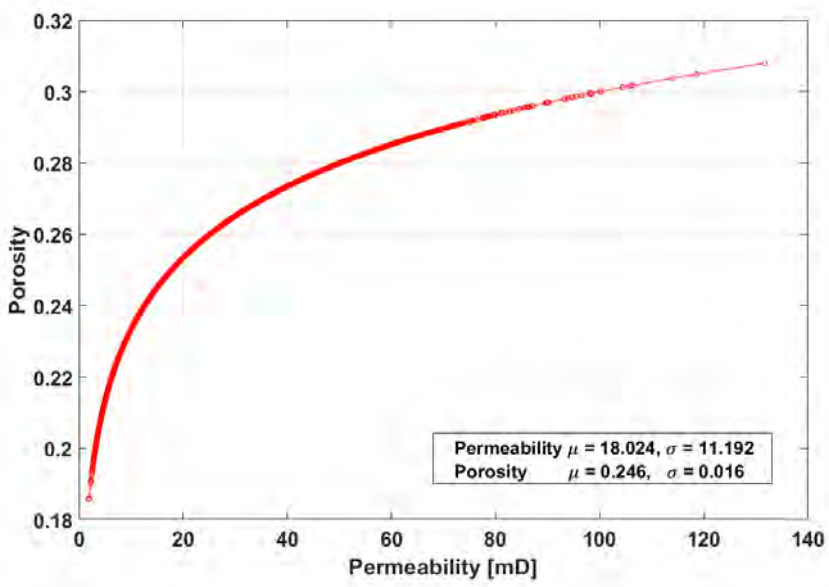

Figure 4.8: Relationship between porosity and permeability of the aquifer reservoir.

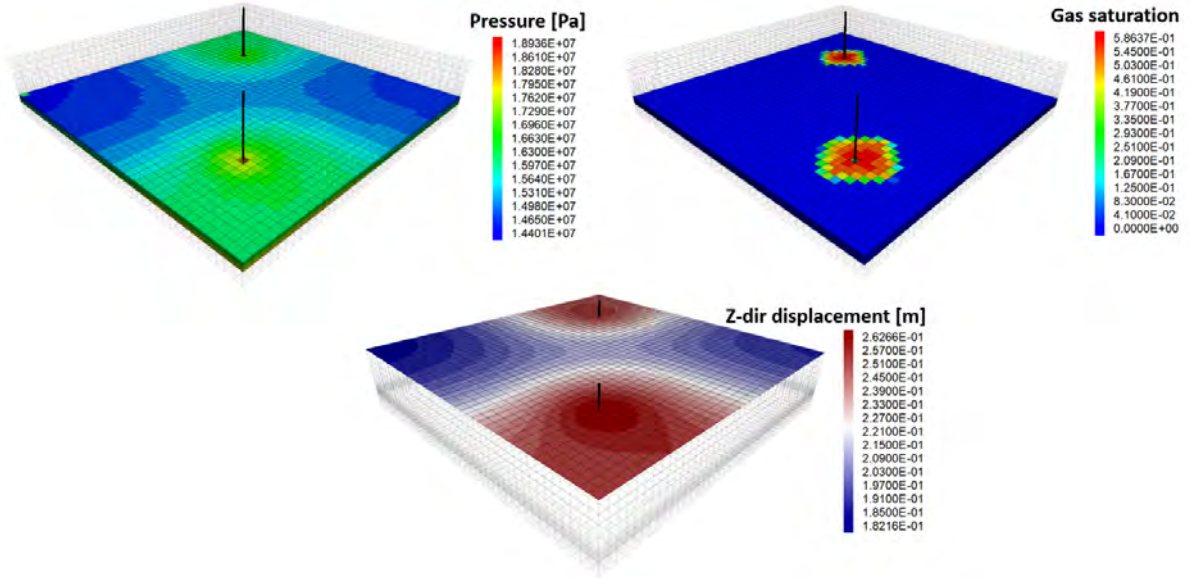

Figure 4.9: Example of output data, pressure, gas saturation, surface displacement after 15 years of CO_2 injection.

others are cell data. As mentioned, our model dimension is 40 $\times$ 40 $\times$ 27 grids. we expand the dimension to 128 $\times$ 128 $\times$ 128. After the conversion, we are ready to apply U-Net architecture to train the model with 3D spatial data of input and output.

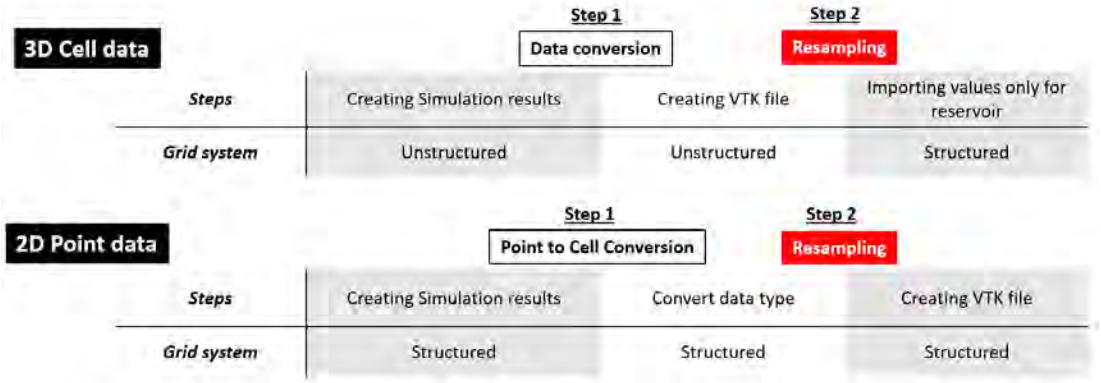

Figure 4.10: Data conversion process for cell data and point data using VTK format.

The implemented architecture can be summarized by the model shown in Figure 4.12. As mentioned before, our input deck consists of 3-Dimensional Spatial data of size (128 $\times$ 128 $\times$ 128) consisting of static properties like permeability or injection rate and so we have used a 3D U-Net convolutional network. The permeability distribution, injection rate influences the temporal distribution of output dynamic properties like saturation, pressure, and displacement. The idea is to learn the complex relationship between these properties using the network architecture that is implemented as the feature maps resulting from the network are used to reduce the error between the predicted dynamic property distribution at various times and the actual property distribution during training. For this, we apply a series of convolutions, normalizations, non-linearizations, max-pooling, and upsampling steps within U-Net. Now, each convolution operation applies a set of filters, wherein each filter applies on the entire input

volume in such a way that it combines and activates the input volume to produce a single output feature map based on the filter properties. Based on the number of filters applied we get an equivalent number of feature maps, which is the number on the top edge of each of the rectangle in the architecture shown in Figure 4.12.

The encoding layers are the ones on the left symmetric halve while the decoding layers are on the right symmetric halve. Each encoding layer consists of two convolution layers that preserve the spatial dimensions of the feature maps by appropriate padding and strides during feature extraction when a filter is applied. After the application of one layer of convolution the data is subject to batch normalization (this helps regularize the output of each layer by helping prevent vanishing gradients which in turn helps the learning process as it reduces the number of run/epochs needed in the network training) and non-linear activation using the ReLU methodology. The application of the non-linear activation function is the most important part of the U-Net architecture. Given all neural networks are trained using stochastic gradient descent (which is an iterative method for optimizing the objective function, in this case, the feature maps from the input volume, the Adam (Adaptative Moment Estimation) algorithm is used in the U-Net architecture in our case), the addition of multiple layers often causes the gradient to diminish significantly (vanishing gradients) when propagated backward. The use of the ReLU method (explained in the section providing the primer) enables the use of an activation function that though looks like a linear function, and implements a non-linear function which makes more complicated relationships in data to be learned.

There are in total five layers in the implemented U-Net. Operations at each horizontal level preserve the matrix dimensions at that level. In the encoding side, the size of the image grad-

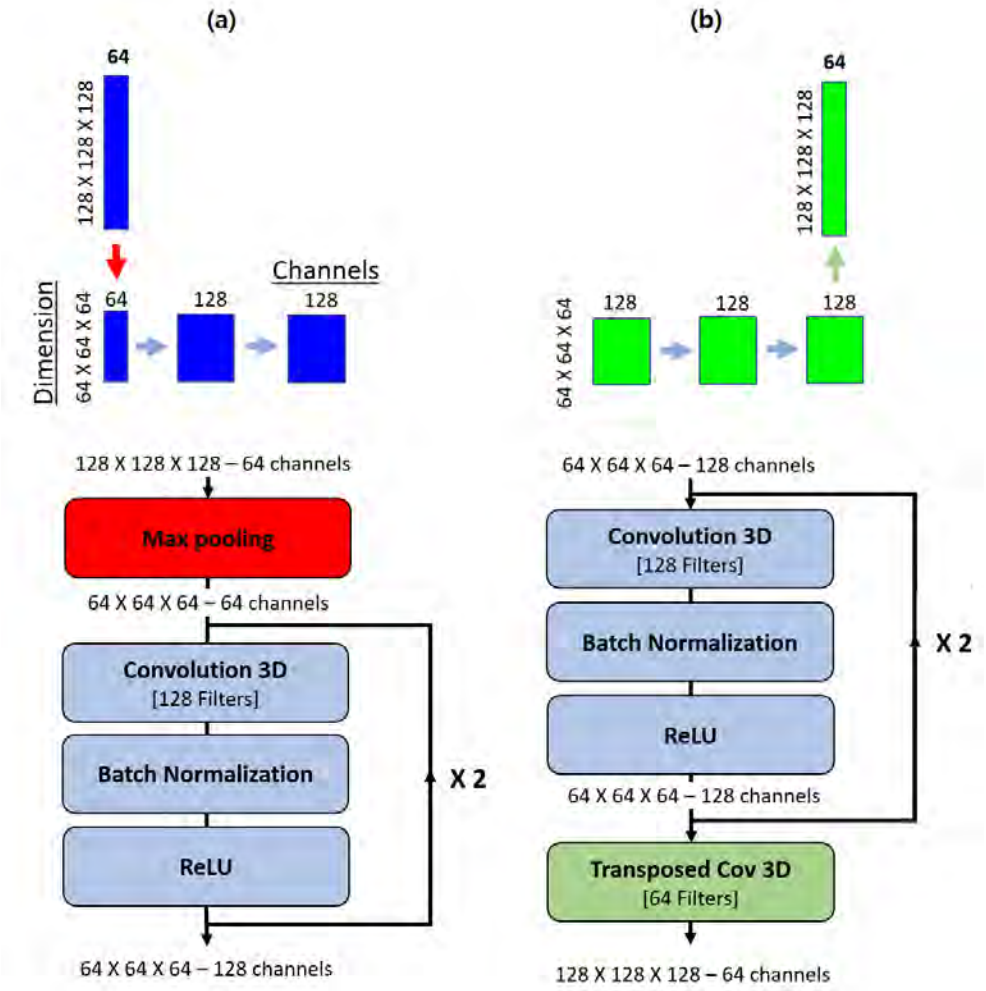

Figure 4.11: Illustration of sequence of convolution3D and transposed convolution operation at a layer.

ually decreases while its depth in terms of the number of feature maps gradually increases during max-pooling. All the mathematical operations performed on the encoding side help extract features within the input volume (Figure 4.11(a)) that are important, however during this process the spatial information of where these are present is lost. The task in the decoder side on the right half is to restore this (Figure 4.11(b)). The results of each operation with encoder and decoder are listed in Table 4.4. Decoding involves upsampling using transposed

convolutions for increasing feature map dimensions to their original size. An important part of the U-net architecture is how, during upsampling/decoding at each level, there is a step for skip connections where results from downsampling are concatenated with upsampled results. These are done to ensure that the spatial information lost during downsampling can be regained, the cropping portion of this operation is necessary only if the resolution of the feature maps is not similar. The entire architecture is designed to learn and optimize the appropriate weights at each layer to ensure low errors in predicted dynamic properties like pressure and saturation with input volumes like permeability distribution or injection rate during validation and model use after training is completed.

The entire learning/training process for the network is controlled by certain hyperparameters which help optimize how the input data is used to get the desire output. The aim is to find the right combination that aids the process of finding the maximum accuracy or the minimum loss for the function. As mentioned before, the Adam stochastic gradient-based optimization is utilized for finding or optimizing the internal model parameters that perform well against measures like mean squared error (MSE), mean absolute relative error (MARE), etc. The core idea is that the search for the optimal parameters proceeds alongside the learning process. In this study, the other optimized hyperparameters apart from the internal weights include:

- Batch Size,

  which indicates the number of input samples that are worked through or processed before internal model parameters are updated. During training, after runs are completed on every batch the predictions are compared against the expected values to get an error value following which some update algorithm is used to improve the model.

- Epoch,

  indicates the number of complete passes of the entire training data set made by the neural network. This indirectly means that it indicates the number of chances each instance of the input data will get to update the internal model parameters.

	Depth	Operation	Filter	Filter size	Stride	Output Dimension
	1	Conv3D × 2	64	3×3×3	1	(N,N,N)
	2	Maxpooling		2×2×2	2	(N/2,N/2,N/2)
		Conv3D × 2	128	3×3×3	1	(N/2,N/2,N/2)
Encoder	3	Maxpooling		2×2×2	2	(N/4,N/4,N/4)
		Conv3D × 2	256	3×3×3	1	(N/4,N/4,N/4)
	4	Maxpooling		2×2×2	2	(N/8,N/8,N/8)
		Conv3D × 2	512	3×3×3	1	(N/8,N/8,N/8)
	3	Transposed Cov3D	256	2×2×2	2	(N/4,N/4,N/4)
		Conv3D × 2	256	3×3×3	1	(N/4,N/4,N/4)
	2	Transposed Cov3D	128	2×2×2	2	(N/2,N/2,N/2)
Decoder		Conv3D × 2	128	3×3×3	1	(N/2,N/2,N/2)
	1	Transposed Cov3D	64	2×2×2	2	(N,N,N)
		Conv3D × 2	64	3×3×3	1	(N,N,N)
		Final Conv3D	1	1×1×1	1	(N,N,N)

Table 4.4: Details of 3D U-net architecture

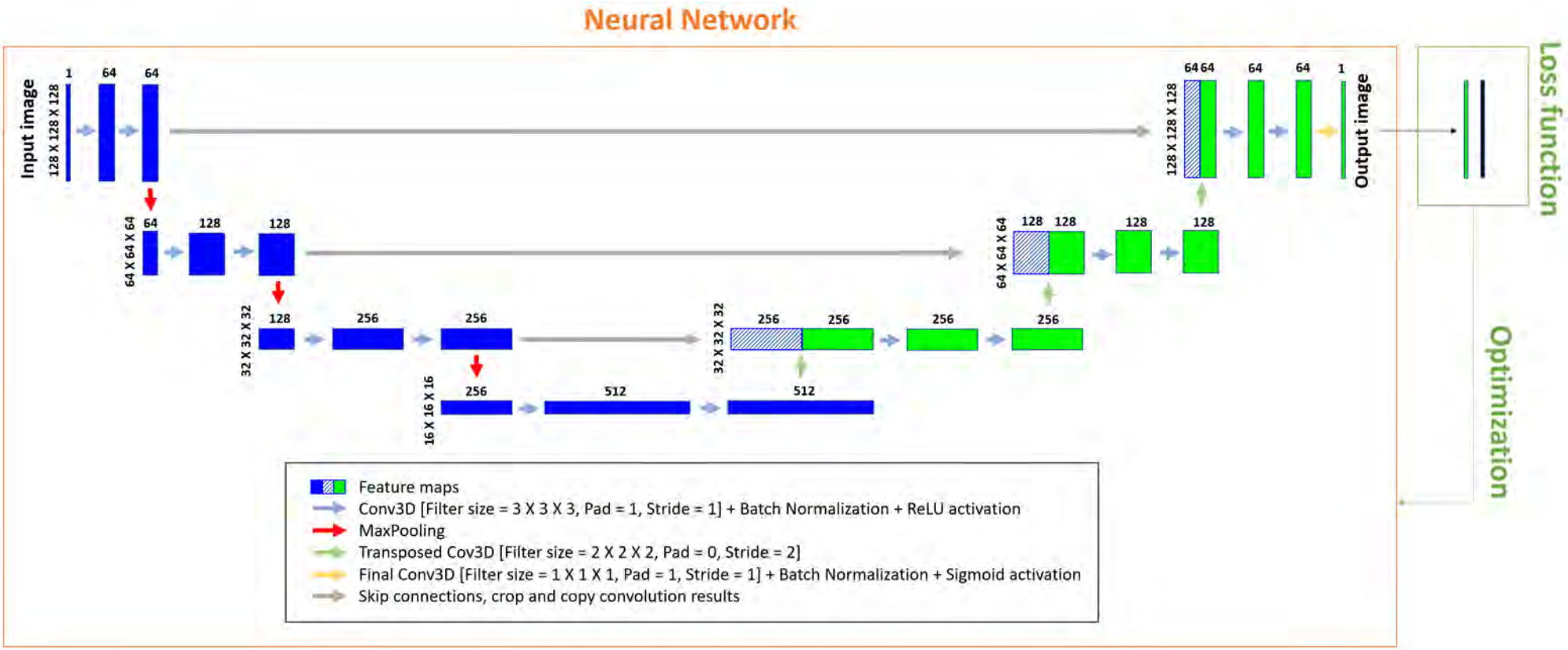

Figure 4.12: U-net architecture with the input size of 128 $\times$ 128 $\times$ 128. The 3D U-net is a network of encoder (contracting the input matrix to extract the feature, left side with blue boxes) and decoder (expanding the matrix to turn back to original size). Each box represents a multi-channel feature map. The arrows correspond to the different operations as listed in the legend. The dimension of the matrix in each operation (x, y, z) is denoted once on the left side of the first box because we maintain the size of the matrix for convolution layer. The number of channels is denoted on top of the box.

4.4 Result

A total of 240 realizations of the geological model is developed with random Gaussian distribution of permeability, of which 60 models correspond to a particular anisotropy range (4 values of 500 m, 1000 m, 2000 m, and 4000 m respectively). Three possible injection rates (1000, 2000, and 4000 tons/day of CO_2) are used for 20 cases each among the geo-models developed for every anisotropy range as can be seen in Figure 4.13. The distribution in dynamic properties (viz. pressure, gas saturation, and displacement) are generated for 34 possible timesteps for each of the anisotropy ranges with different injection rates. Therefore, among the three channels of inputs, i.e., permeability distribution, injection rate, and time, there are in total 8160 different combinations of the input parameters each of which generates a corresponding spatial distribution of the dynamic properties (pressure, gas saturation, and surface displacement).

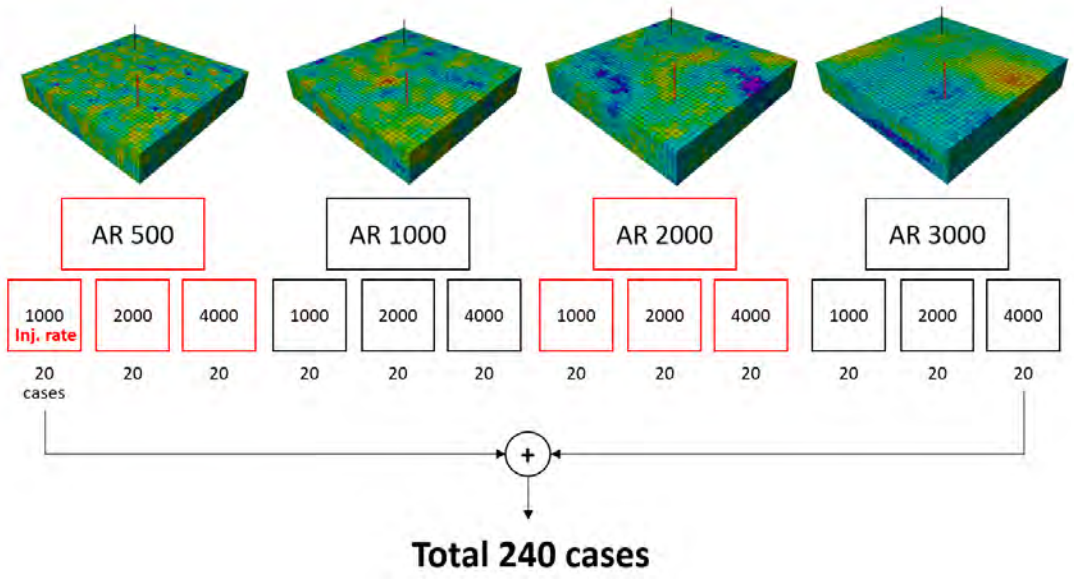

Figure 4.13: Total cases with 240 realization, 3 anisotropy range of Gaussian distribution, and 3 injection rates.

Of the total number of input property combinations, a random set consisting of 6528 (= 192 permeability realization $\times$ 34 time steps) cases are used for training the surrogate model, and 816 (= 24 permeability realization $\times$ 34 time steps) cases each are used for validation and testing the performance of the developed surrogate model. The realizations are divided into training, validation and testing set (an 80-10-10 percent division). It might be surmised that the total number of samples for training might be small, but it must be noted that generating the data for 15 years using each geo-model adds a time constraint in terms of simulation time that in itself justifies the cause for further research in surrogate model development. Hyperparameters like epoch and batch size are also constrained to values listed in Table 4.5 based on monitoring of training results recorded in terms of the evolution of the loss function of the developed surrogate model over epochs against actual values from simulation results.

Hyperparameters	
Epoch	200
Batch size	40
Optimization	Adam with 1e-4 learning rate
Loss function	Mean square error

Table 4.5: Hyperparameters used in this study

Figure 4.14, Figure 4.15, and Figure 4.17 compare the distribution of pressure, gas saturation, and surface displacement between the simulated and surrogate models for 3 selected test realizations of the geological models at 15 years. The distributions show the results for each of the predicted properties for the three injection scenarios that were considered. As is evident from the pressure distribution plot at 15 years in Figure 4.14, both in the surrogate model and simulation results, the pressure does go up around the injection well due to reservoir pressurization. However, there is some incongruence between the results from the surrogate model when compared to the actual simulation results, though the basic trend is the same. In the dis-

tribution generated from the surrogate model, we see that it can spatially resolve the regions where the pressure goes higher (i.e., in the vicinity of the injection wells) however the exact distribution does not show a very close match. This can be a remnant of training on a smaller data set.

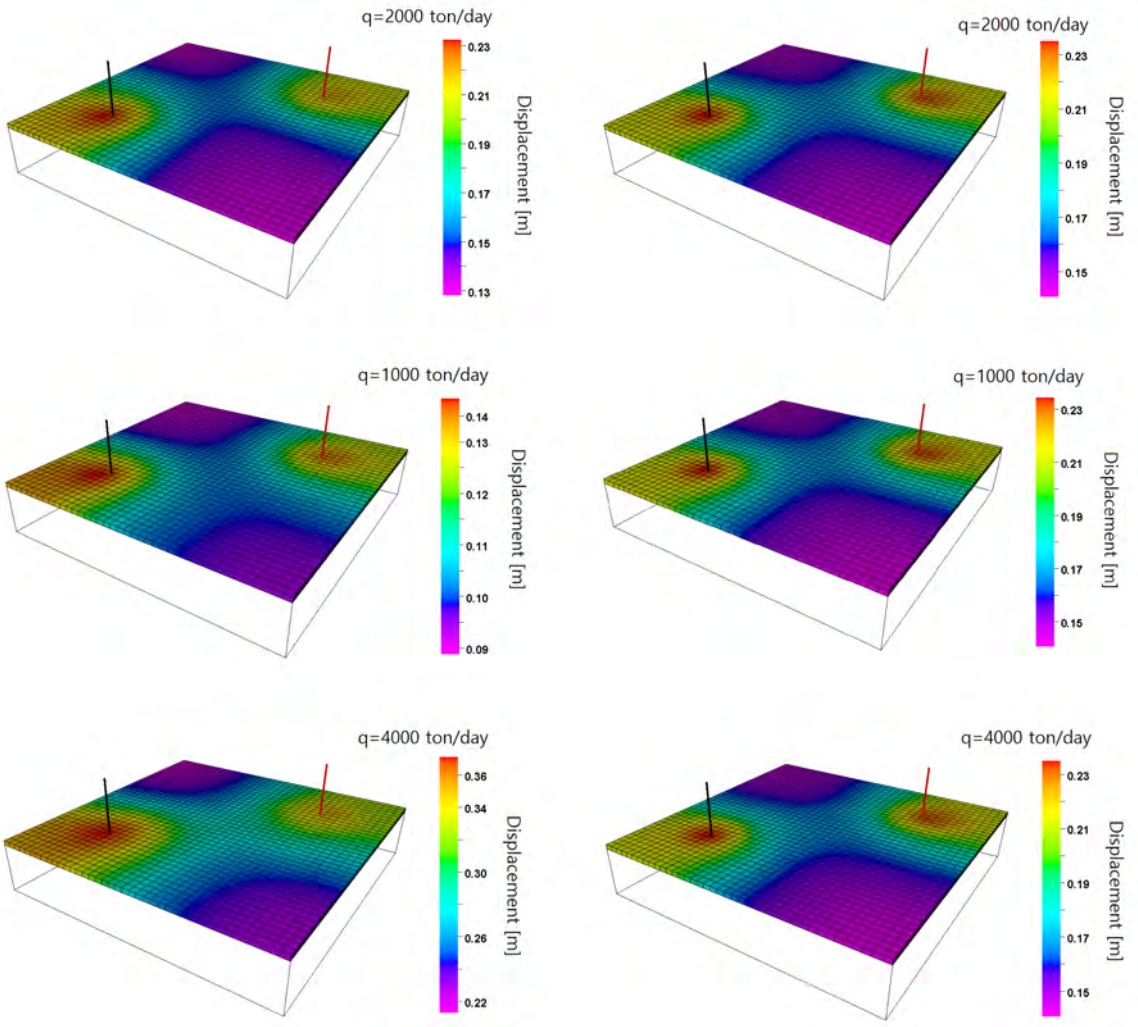

Figure 4.14: Pressure distribution from numerical simulation (first column) and 3D U-Net surrogate model (second column) for a test case after 15 years of CO_2 injection.

Looking at Figure 4.15, which shows the gas saturation distribution for three geo-models at 15 years we observe that slight variations exist in CO_2 saturation distributions around the

injection wells due to the variations in permeability distribution in space and different injection rates. It is evident though that since gas is lighter a distinct plume is moving upward as it fills up the storage region, which is replicated across both the simulation and surrogate model results. We can also see that if the injection rate is higher the size of the plume is larger both in the simulation and surrogate model results. However, the plume size from the simulation results is more sensitive to injection rate when compared to the surrogate model predictions.

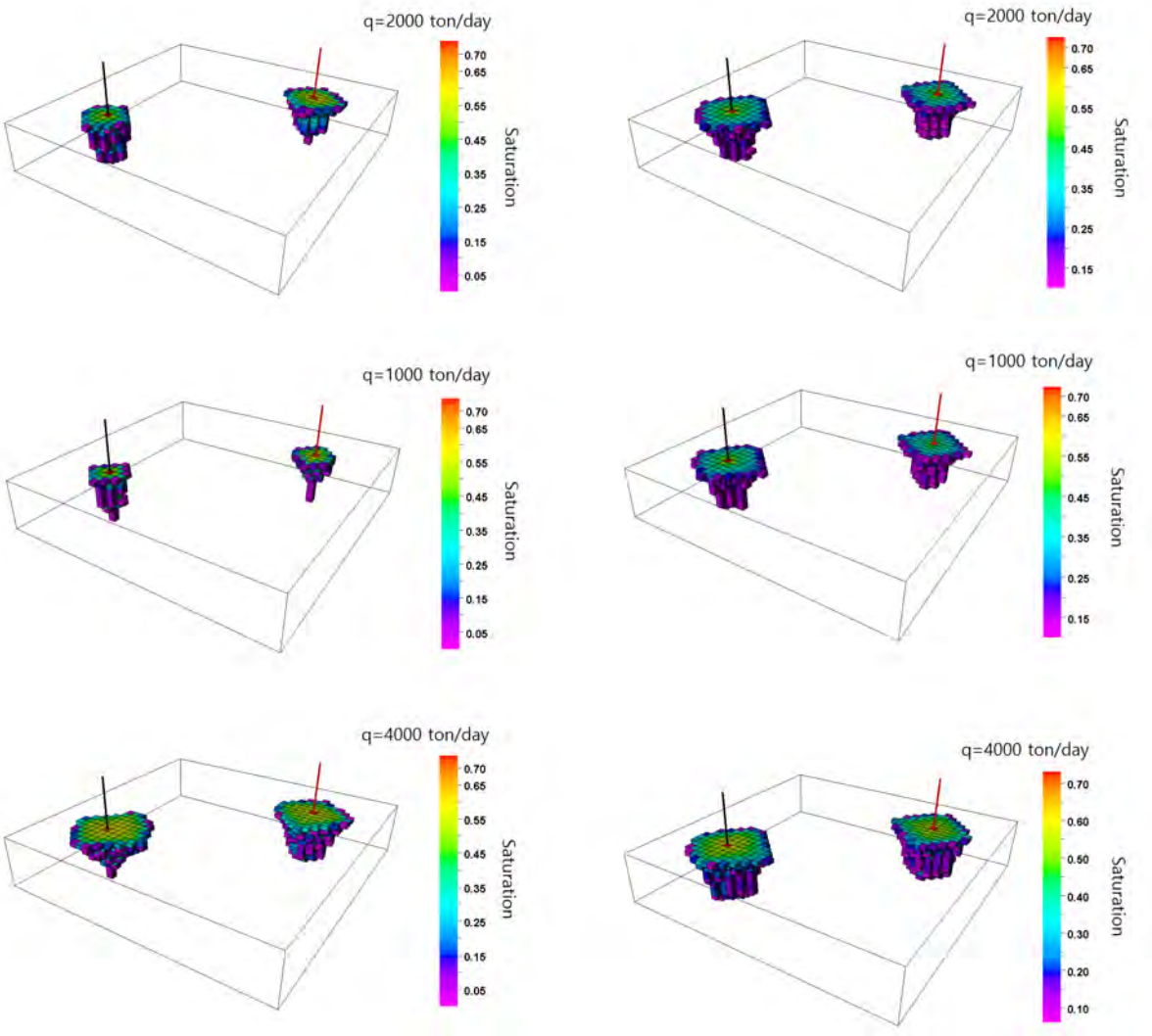

Figure 4.15: Gas saturation distribution from numerical simulation (first column) and 3D U-Net surrogate model (second column) for a test case after 15 years of CO_2 injection.

The surface displacements are also predicted using the surrogate model, the results of which are shown in Figure 4.17. Both the simulation results and surrogate model follow the general trend expected where the displacement is the greatest right over the injection well sites. We also observe in Figure 4.17 that the surrogate model results are similar across injection rates and look very identical to the displacement distribution at an injection rate of 2000 tons/day of CO_2. This has been evaluated further using the plots in Figure 4.16 where we observe that the surrogate model cannot resolve displacement on a temporal scale but the value itself closely matches the displacement at the median injection rate of 2000 tons/day. Similarly, we also observe that the match between the surrogate model predictions and simulation results are good (in terms of MSE) in 2000 tons/day scenario of CO_2 injection for all dynamic properties that have been predicted.

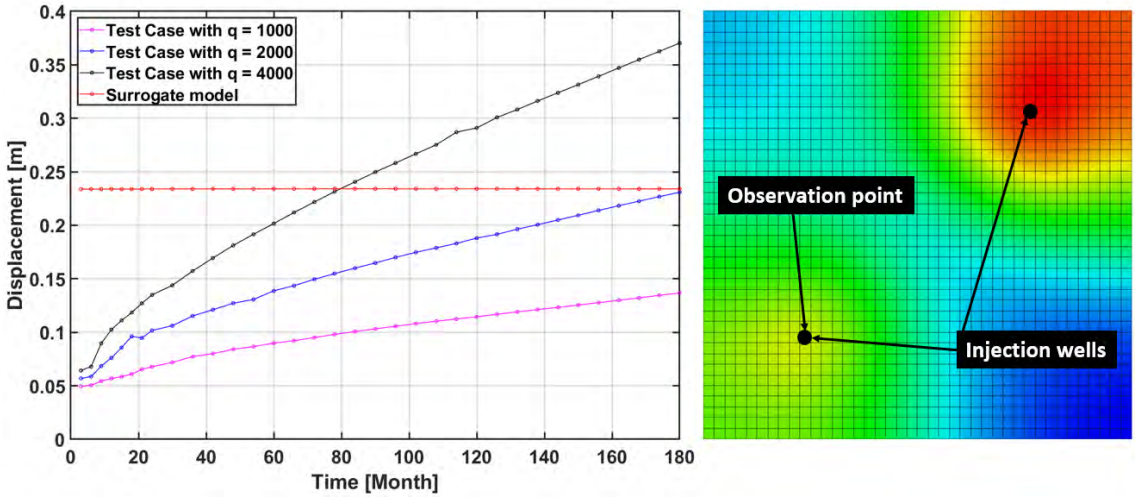

Figure 4.16: Vertical surface displacement from numerical simulation and 3D U-Net surrogate model at two observation locations for a test case for 15 years of CO_2 injection.

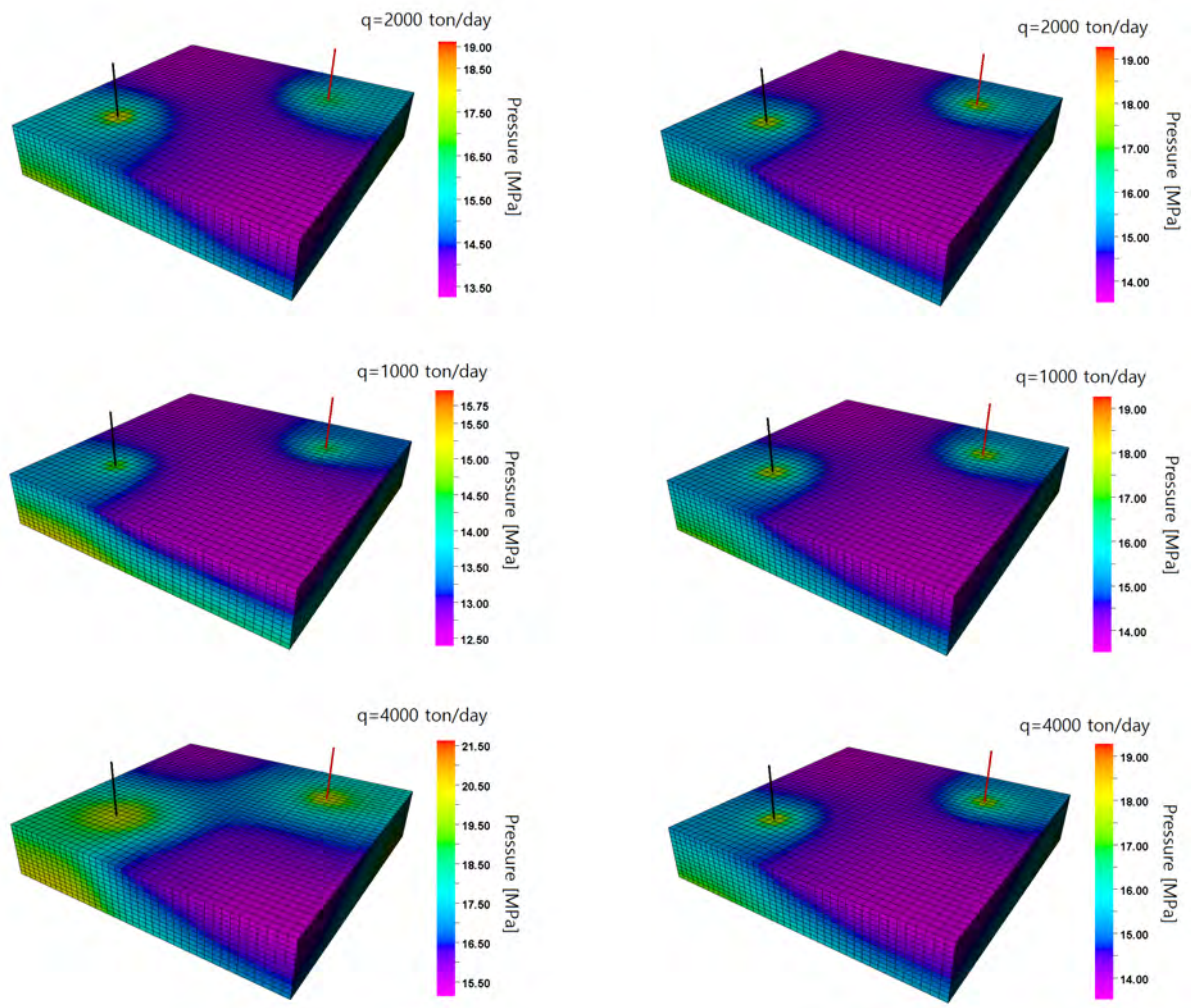

Figure 4.17: Vertical surface displacement from numerical simulation (first column) and 3D U-Net surrogate model (second column) for a test case after 15 years of CO_2 injection.

The evolution of the Loss function for pressure, saturation, and displacement over epochs during training and validation are shown in Figure 4.18, Figure 4.19, and Figure 4.20. The loss function in this case represents the evolution of the loss value from the Adaptive Moment Estimation (Adam) Optimizer over epochs for each output variable. The error is calculated using mean square error, i.e., it is expressed terms of the relative squared difference between the actual and the predicted values. It must be noted that there is a reasonable amount of variation between the simulation results and the surrogate model which can perhaps be attributed

to the smaller training data set size. The logic behind this is based on the understanding that on a temporal scale, there are only 240 realizations of each dynamic property at each time step which includes the variations brought about using different injection rates. This can be proved further when we look at MSE (shown in Figure 4.21) calculated against the simulation results over 24 realizations of the test set for all 3 dynamic properties that are predicted using the surrogate model at each time step. We see that the MSE of pressure and surface displacement consistently reduces till the last time step is reached while the saturation MSE shows a minor reduction. This is similar to the observation in the pressure and surface displacement compared in Figure 4.18 and Figure 4.20 where the match between the surrogate model predictions and simulation results are best at 15 years.

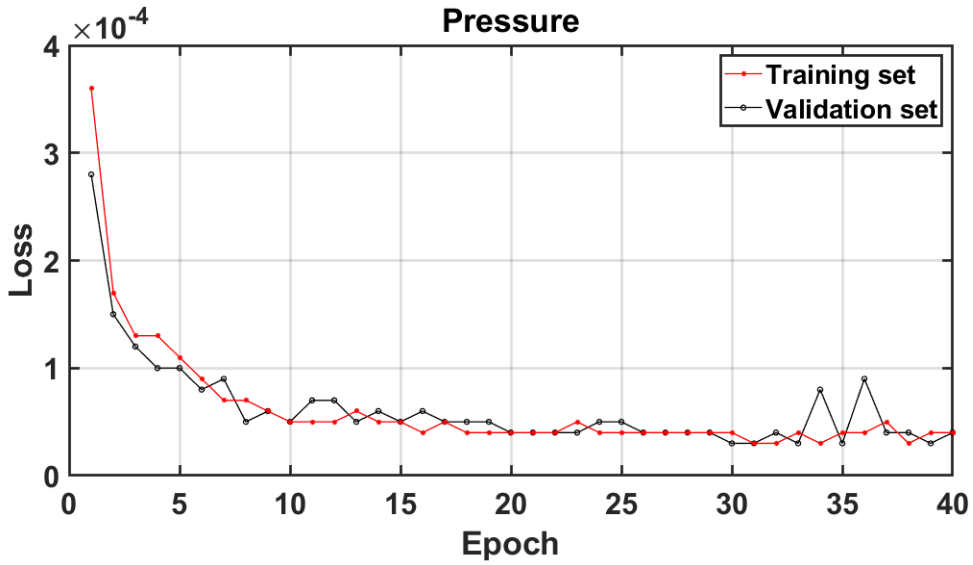

Figure 4.18: Loss value over epoch for pressure distribution.

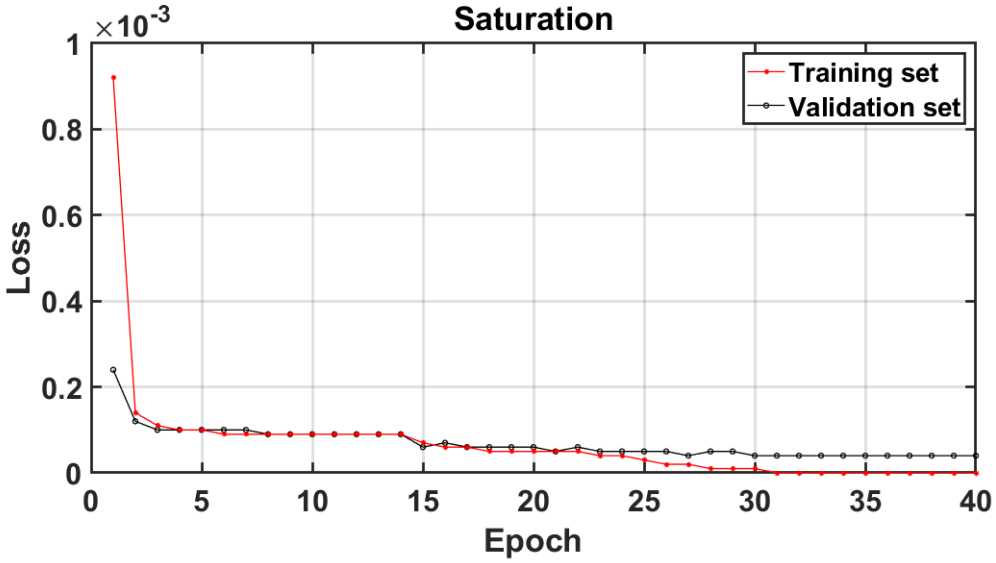

Figure 4.19: Loss value over epoch for gas saturation distribution.

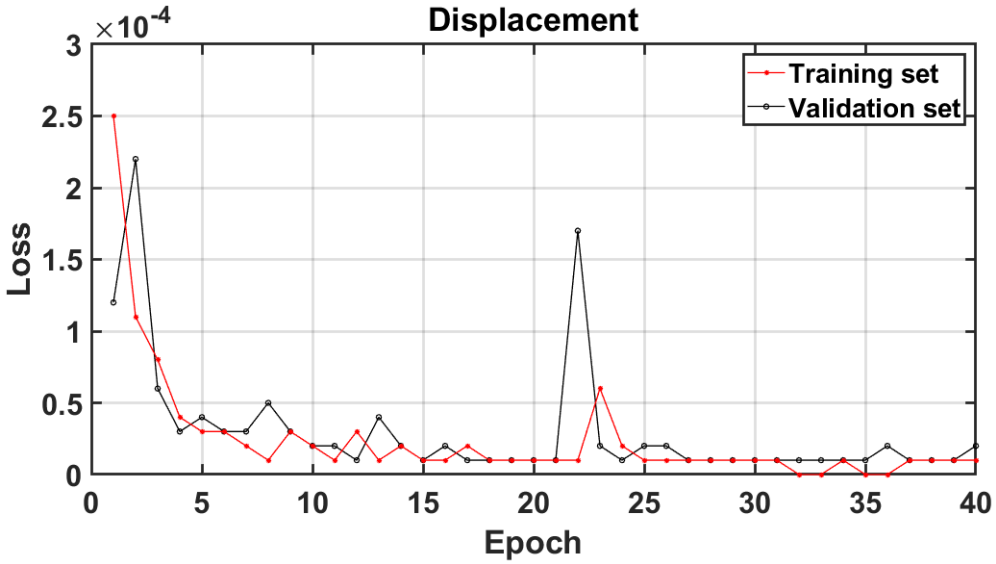

Figure 4.20: Loss value over epoch for surface displacement distribution.

Similarly, in Figure 4.22, we plot the MSE for 8 realizations of the test set for all 3 dynamic properties considering all the time steps at each injection rate. Here we see that the MSE

reduces as the injection rate increases. This indicates that our surrogate model can predict surface displacement and pressure distribution more accurately at higher injection rates. The results presented in Figure 4.18, Figure 4.19, and Figure 4.20 show that the loss values are small enough for the training and validation set to justify saying that the surrogate model was successfully built with the data set it was trained on (as the loss values are below the order of 10-4 for all three predicted variables). However, the loss values of the test set show a relatively higher value as shown in Figure 4.21 and Figure 4.22 which means that the surrogate model has been overfitted to the training and validation sets. Considering that the current criterion is maintained (three input channels consisting of injection rate, time, and permeability) we believe that the issue of overfitting can be mitigated using a larger data set involving more simulation results for each geo-model at every time step and for every injection rate. Another possible approach to dealing with this issue can be reducing architecture complexity in terms of the convolution layers and the depth of the U-Net architecture. However, we do not expect this approach to address the overfitting issue significantly for the current model setup that we use.

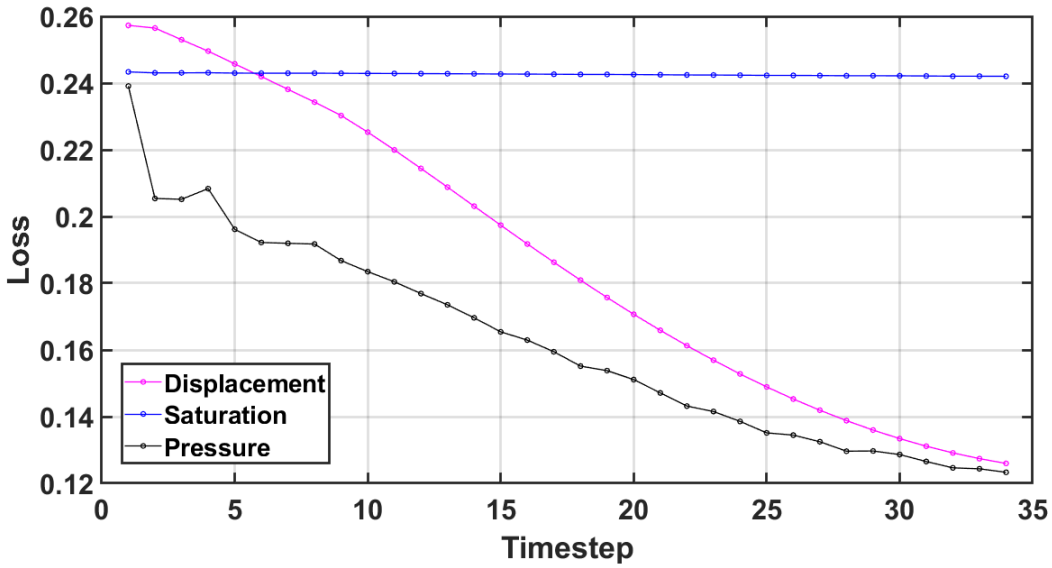

Figure 4.21: Loss value at each timestep for 3 output variables.

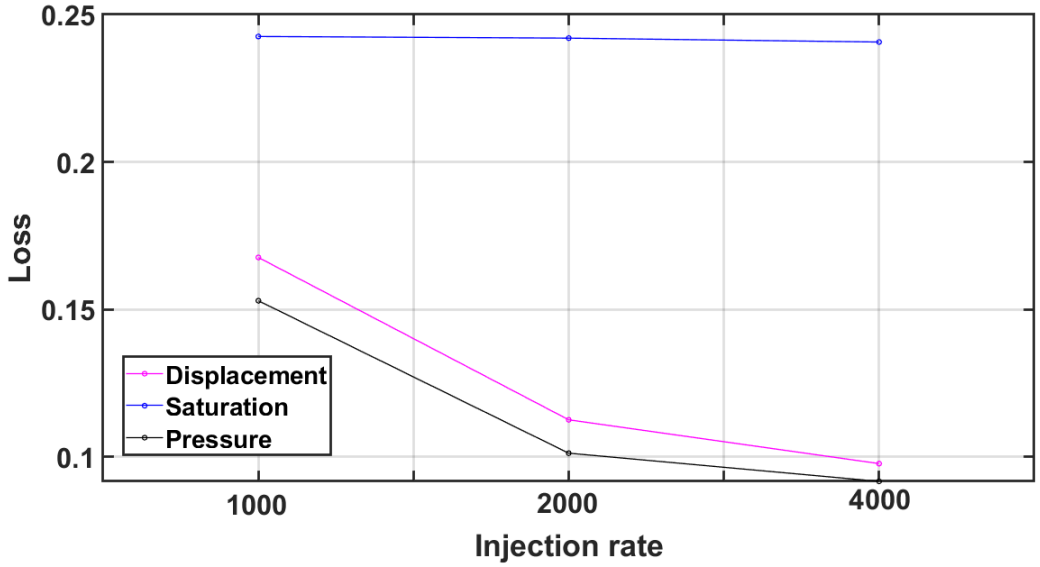

Figure 4.22: Loss value at each injection rate for 3 output variables.

4.5 Conclusion

We prove that flow and geomechanical properties can be predicted with significant accuracy using deep learning algorithms. A workflow for predicting surface displacement in the vertical direction, pressure, and saturation fields during a CO_2 storage operation on a temporal scale is shown using a Convolutional Neural Network-based Deep Learning Algorithm called U-Net. Simulation results with Random Gaussian permeability distributions and Injection rates were used to develop this surrogate model. The results have shown reasonable accuracy and indicate that studies involving more complicated model setups need to be attempted in the future.

5. WELLBORE STABILITY ANALYSIS INDUCED BY PRODUCTION FROM MARINE GAS HYDRATE DEPOSITS

In this chapter, we explain and study the use of a simulator created for modeling potential wellbore instability of gas hydrate-bearing sediments induced by depressurization during gas production. Specifically, we focus on the region located in the vicinity of the wellbore to identify slip phenomena using mechanical properties that define the discontinuous interface between the casing and the formation. The developed simulator is applied in studying the described phenomena in two existing fields located in the Ulleung Basin of South Korea, as well as on hydrate deposits located in the Prudhoe Bay–Kuparuk River area of Alaska, United States. Compared to studies conducted on this issue before, our approach is more rigorous with various possible bonding scenarios considering slip phenomena and wellbore failure. We believe that the findings presented in this study can contribute practically to design considerations that need to be kept handy during the implementation of Hydrate drilling projects, be it during any phase from drilling to production.

5.1 Geological description

5.1.1 Ulleung Basin (UBGH2-6) in South Korea

The Ulleung Basin is located at the southwestern region of the Korean East Sea shown in Figure 5.1. It is situated at water depths of about 1500 to 2300 m. The basin was formed by crustal extension during the Late Oligocene and Early Miocene periods and takes a bowl-like shape. The basin is marked by broad gentle slopes in the south and east sides, narrow and steep slopes in the west sides, there exist numerous ridges and troughs along the northern boundary [115]. The sediment thickness in the basin ranges from 5 km at its central region [116] to about 10 km at its southern part. Seismic analysis of the stratigraphy suggests that there are four distinct subdivisions within the sediments located in this basin ranging from

early Miocene to Quaternary eras [117]. In 2007, the first Ulleung Basin Gas Hydrate Drilling Expedition (UBGH1) was completed. A second expedition (UBGH2) was conducted in 2010 to perform studies that helped select potential sites that posed no issues relating to the potential leakage of gas-hydrates into the circumferential environment in the vicinity of the zones of interest. Under UBGH2, 13 sites were developed and analyzed for geological, geophysical, petrophysical, hydraulic, thermal, geomechanical, and geochemical properties using logging data and laboratory experiments [118] [119] [4]. The thickness, 100 m, of gas hydrate-bearing reservoirs have been identified during the expedition in lithologies consisting mainly of fractured mud, thin-bedded turbidite sand layers in the basin [120]. Conditions of formation of natural gas hydrates have been favored by the presence of high sedimentation rates, high geothermal heat flow, High TOC sediments and residual hydrocarbon gases in the area [121]. One of the sites investigated during the second expedition, UBGH2-6 (shown in Figure 5.1) was identified as a feasible pilot site for the production test according to the seismic survey and laboratory data of the core samples. This site contains fine-grained sediments which exhibit high compressibility, high porosity, and low permeability [119].

5.1.2 Prudhoe Bay area on the North Slope (PBU-L106) in Alaska, USA.

The PBU-L106 site is located on the North Slope of Alaska [5] [57] [55], as shown in Figure 5.2. The geology, hydraulic, geomechanical, and geochemistry of the gas hydrate deposits in the North Slope of Alaska were studied and described with analysis of downhole log data from substantial a number of wells in the area of interest [122]. According to a number of publications, Unit C in the PBU-L106 site consists of two layers of hydrate-bearing sediments named Hydrate C1 (deeper layer) and Hydrate C2 (shallow layer) surrounded by impermeable shale layers at the top and bottom boundaries.

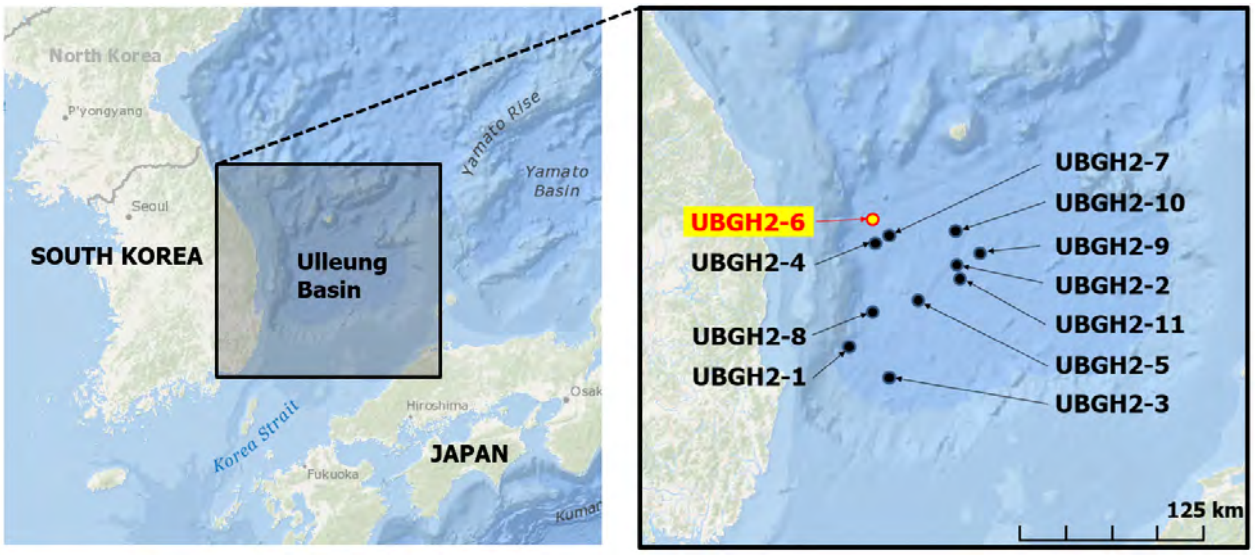

Figure 5.1: Regional map of the East Sea of South Korea and its surrounding region. Including the Ulleung Basin Gas Hydrate Drilling Expedition (UBGH) area, the left figure is expanded to show the detailed map of drill sites of UBGH2 [3] [4]

.

5.2 Numerical modeling

We use an axisymmetric simulation domain for both projects, considering methane production with a vertical well. In this study, we consider the exact formulation of 3D axisymmetric geomechanics to obtain accurate results using roller boundary conditions. To put the domain in context, we consider a cylindrical coordinate system for stress and momentum balance to calculate deformation and stress near the wellbore accurately. From numerical results presented in this section, we conclude that there exists little subsidence at the surface due to production but significant vertical displacement above and below the hydrate zones while producing using depressurization. Thus, careful consideration for wellbore stability is required to account for dissociation-induced volumetric changes in methane hydrate formations during real field operations.

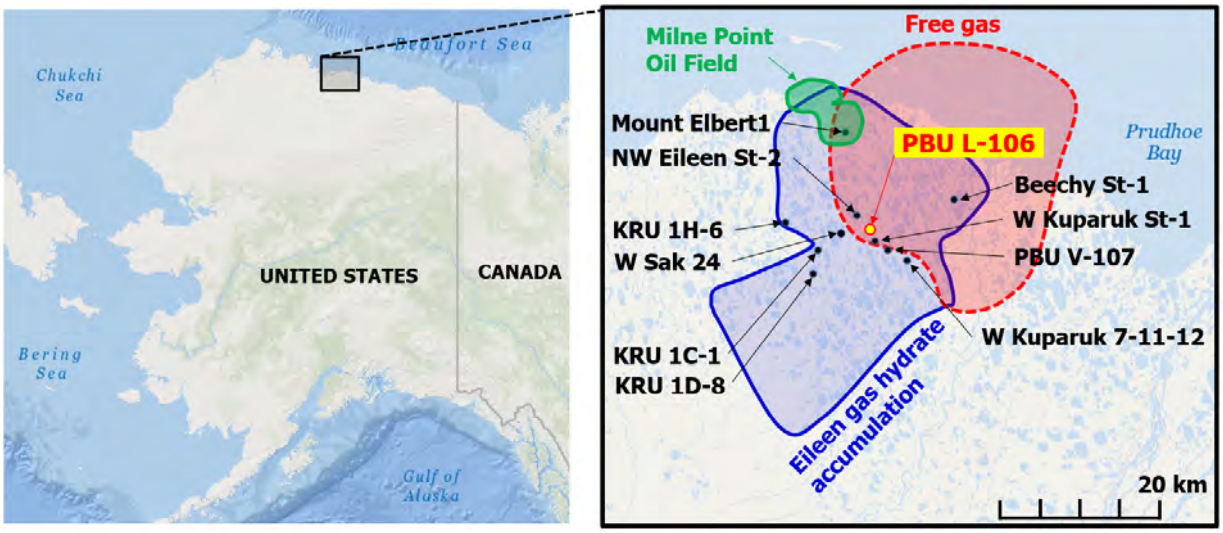

Figure 5.2: Regional map of the Eileen gas hydrate accumulation overlying in the Prudhoe Bay–Kuparuk River area and Milne Point oil fields in Alaska [5] [6]. The map also shows the locations of the gas-hydrate-bearing units including the PBU L-106 site.

5.2.1 Ulleung Basin (UBGH2-6) in South Korea

We have built a very up-to-date model, integrating data from all possible sources, and called it the 2017 Model for this study. The simulation domain used as mentioned before is axisymmetric. Compared to the 2014 Model, the 2017 Model contains more gas hydrate layers and different hydrate saturations within the layers identified as reservoirs as shown in Figure 5.3. We use a simulator of coupled flow and geomechanics (TOUGH+Hydrate-FLAC3D) for this study. The aim of the study is to perform an in-depth mechanical analysis near the wellbore/along the pipe. Various cases were tested with realistic interface properties to simulate different possible scenarios to assess potential impacts on the wellbore and pipe. The data gleaned from these analyses can provide valuable insights for field testing in the future.

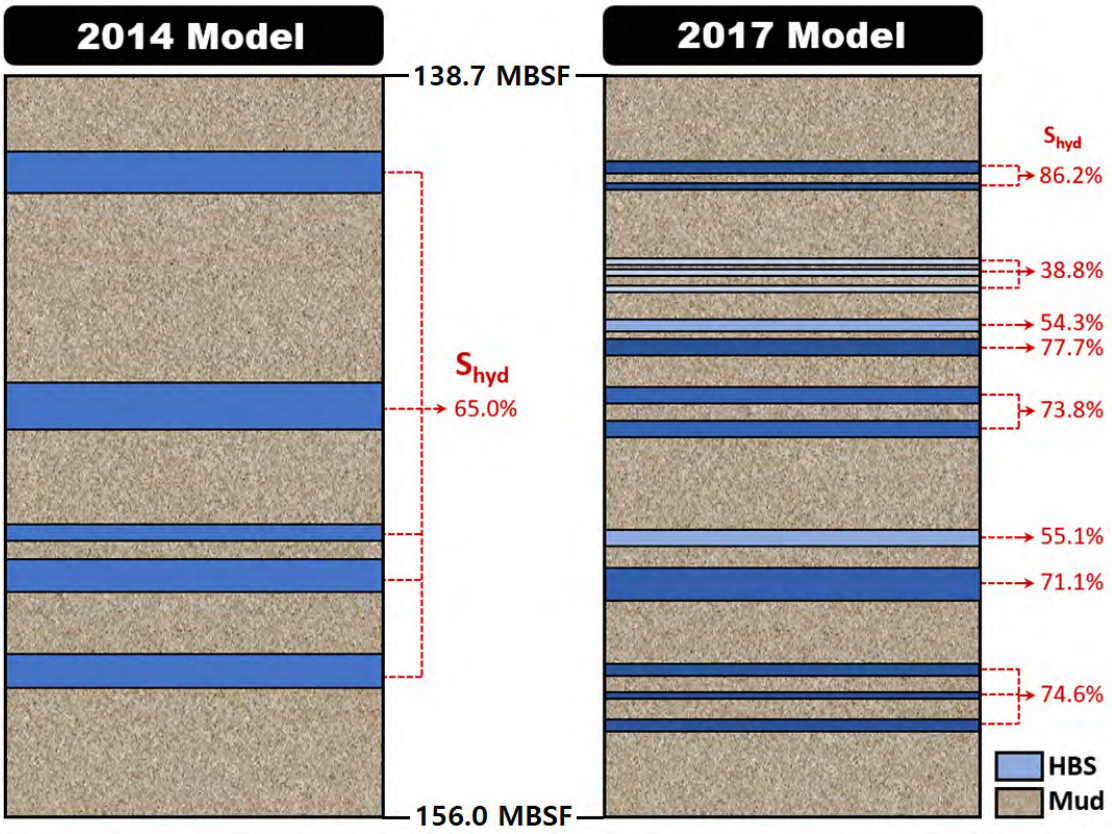

Figure 5.3: Schematic diagram of hydrate-bearing sediments and mud layers of UBGH2-6, (Left) 2014 Model (Right) 2017 Model.

5.2.1.1 Model description

As shown in Figure 4.4, we consider two different domains for geomechanics (left) and flow (right), where the flow domain is included in the geomechanics domain to reduce computational cost. The benefit of using such an approach has been shown in the previous chapter on CO_2 storage as well. The total domain size of the 2017 Model is 300 m by 200 m for numerical simulation in the radial and vertical directions, taking axisymmetric geomechanics simulation, respectively. The domain consists of non-uniform gridblocks (216 blocks and 30 blocks including the pipe element) and includes 173 layers. In addition, smaller gridblocks have been created near the wellbore and in the gas hydrate zone to make sure that smaller-scale changes that occur here are observed and are not easily attenuated due to larger block

size. The thickness of the hydrate layer is Δz = 0.1 m. The initial pressures at the top and bottom of the domain are 22.90 MPa and 24.57 MPa, respectively, and the initial temperature is 15°C. The pressure is distributed linearly from top to bottom of the domain while the temperature is maintained constant. The initial hydrate saturation in the hydrate zones varies layer by layer from 33.8% to 86.2% as can be seen in Figure 5.4(b). The initial total vertical stress starts from -23.1MPa at the top layer because it represents the seafloor, distributed with the gradients of -25.0 kPa/m along the depth. In this study, we assume the vertical and horizontal stresses are the same. Note that, the compression stress is negative. We produce gas by depressurization, by applying a constant bottom-hole pressure of 9 MPa. In addition, we assume a full completion from 138.7 MBSF to 156.0 MBSF rather than a partial completion scenario, targeting only the hydrate-bearing zones. We use the main properties of flow and geomechanics simulation listed in Table 5.1.

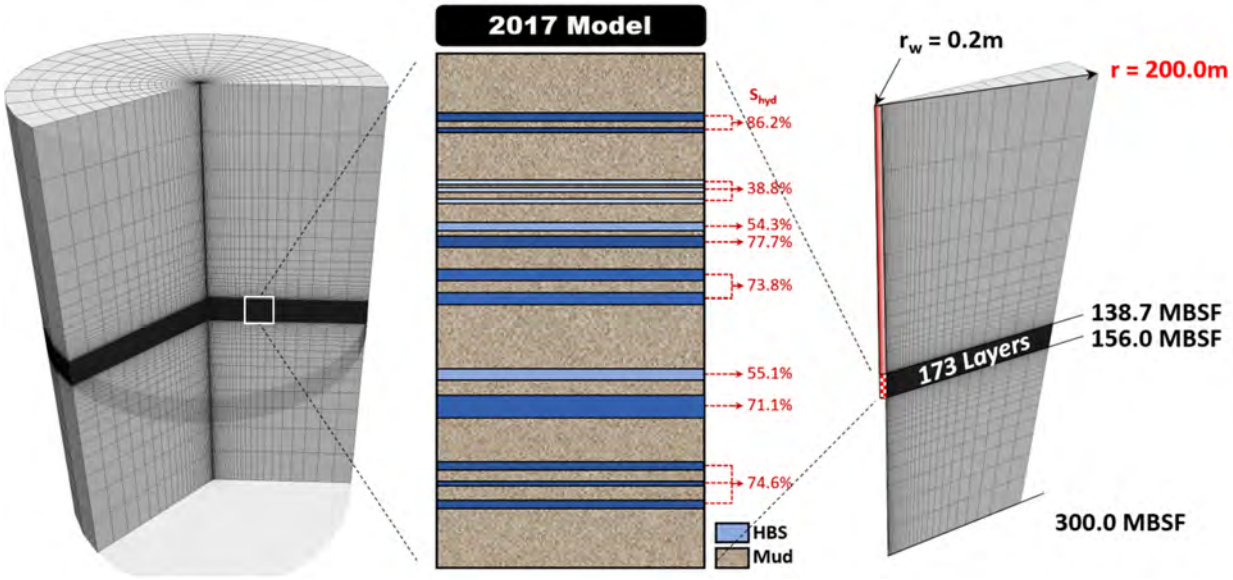

Figure 5.4: (Left) Simulation domain for geomechanics, (Middle) geological information of UBGH2-6, and (Right) discretized domain for flow.

Property	Overburden	Hydrate layer	Mud-Interlayer	Underburden	Unit
Drained bulk modulus, S_H=0%	15.55	27	20	22	MPa
Drained shear modulus, S_H=0%	5.185	16	6.667	7.407	MPa
Drained bulk modulus, S_H=100%	285	933.33	285	285	MPa
Drained shear modulus, S_H=100%	99.75	560	99.75	99.75	MPa
Permeability, S_H=0%	0.02	500	0.14	0.02	mD
Initial porosity	0.76	0.45	0.67	0.0	

Table 5.1: Material properties of UBGH2-6 site for flow and geomechanics.

5.2.1.2 Simulation results

After running a two-way coupling numerical simulation without interface elements, we use the yielded results to perform a sensitivity analysis of wellbore cement fracturing by changing interface properties. This is done to investigate the impact of the interface on wellbore stability. Figure 5.5 shows distributions of pressure, temperature, gas, and hydrate saturation. The pressure tends to decrease mostly with production. However, there are some layers that exhibit substantial pressure increases due to the compaction and undrained conditions, these layers are located just above and below gas hydrate layers in the zones characterized by mud lithologies. Compared to the 2014 Model (Moridis et al. 2013), in the 2017 model, dissociation of gas hydrates occurs at the layers that have low hydrate saturation at the initial time, this results in a much larger production of gas and water, as can be seen in Figure 5.6. Figure 5.7 shows distributions of vertical displacement, volumetric strain, radial effective stress, and vertical effective stress after 14 days. Significant vertical displacement can be seen locally near the hydrate-bearing zones even after 14 days of production, where the vertical displacement ranges between -1.0 m to 0.8 m. The vertical displacement at the sea bottom is about 0.1 m, which is an important deliverable because it is possible to have risky situations even though

the small amount of uplift phenomena is observed on the sea bottom.

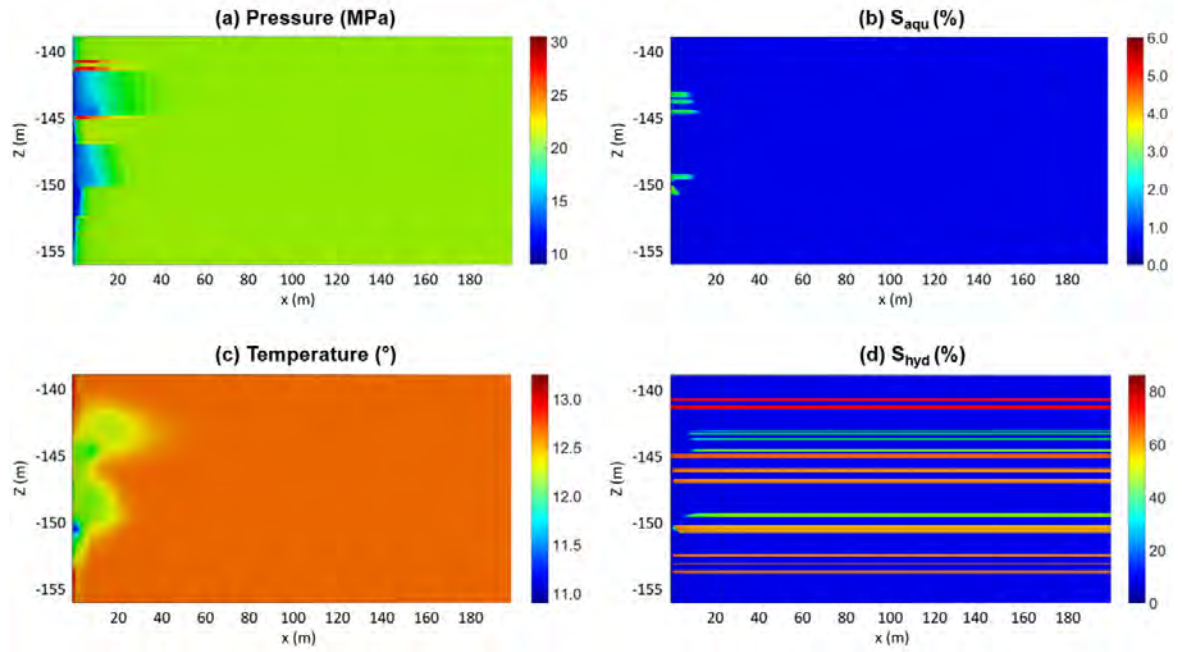

Figure 5.5: Distributions of (a) pressure, (b) gas saturation, (c) temperature, and (d) hydrate saturation after 14-day production.

We take 5 test cases with different realistic interface mechanical properties shown in Table 5.2 to conduct the wellbore stability analysis. The interface elements are implemented between the pipe and the reservoir formation (Figure 5.8), where we assume that it is possible to have shear and normal-slip depending on the initial bonding force. Figure 5.9 shows the normal failure along the vertical well by using the Mohr–Coulomb failure model for all 5 cases. It is worth noting that all the cases show shear failure and displacement in the vertical direction for each case is shown in Figure 5.10. Case 1 is based on the properties from the laboratory test, the reference case [53]. For uncertainty analysis, we vary the normal stiffness, shear stiffness, tensile strength, and cohesion values. For all the 5 cases, we find that the vertical stress in the pipe ranges from -150 MPa to 120 MPa shown in Figure 5.11. This implies

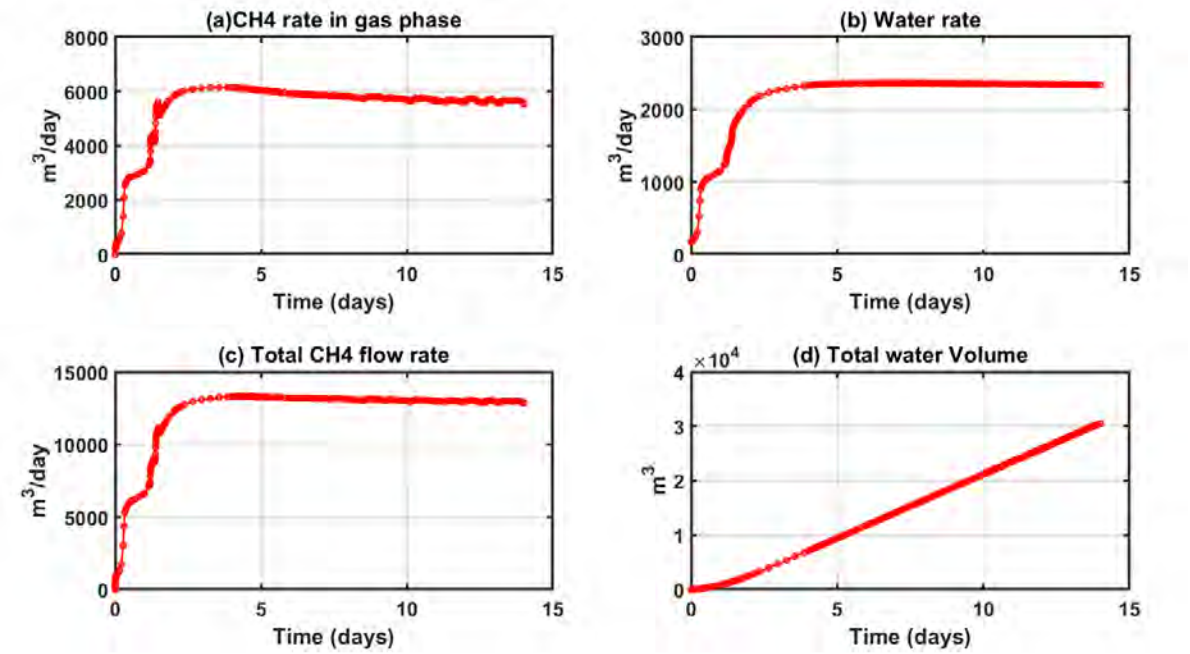

Figure 5.6: (a) Methane gas flow rate, (b) water flow rate, (c) Total methane flow rate, and (d) cumulative production of water after 14-day production.

that it is safe within the ranges of the current scenario to use 9 5/8" production casing. The strength of intact casing is normally 758 MPa (C-95/T-95/P-110 Grade). We use a 454.8 MPa for yield strength because the casing is perforated by 60%.

Property	Case 1		Case 2		Case 3		Case 4		Case 5	
Normal stiffness	57.41	MPa	5.741	MPa	57.41	MPa	57.41	MPa	57.41	MPa
Shear stiffness	26.11	MPa	26.11	MPa	2.611	MPa	26.11	MPa	26.11	MPa
Tensile stress	1.74	MPa	1.74	MPa	1.74	MPa	3.48	MPa	1.74	MPa
Cohesion	17.39	MPa	17.39	MPa	17.39	MPa	17.39	MPa	1.739	MPa
Friction angle	30	°	30	°	30	°	30	°	30	°

Table 5.2: Interface properties of 5 cases for wellbore stability of UBGH2-6 site.

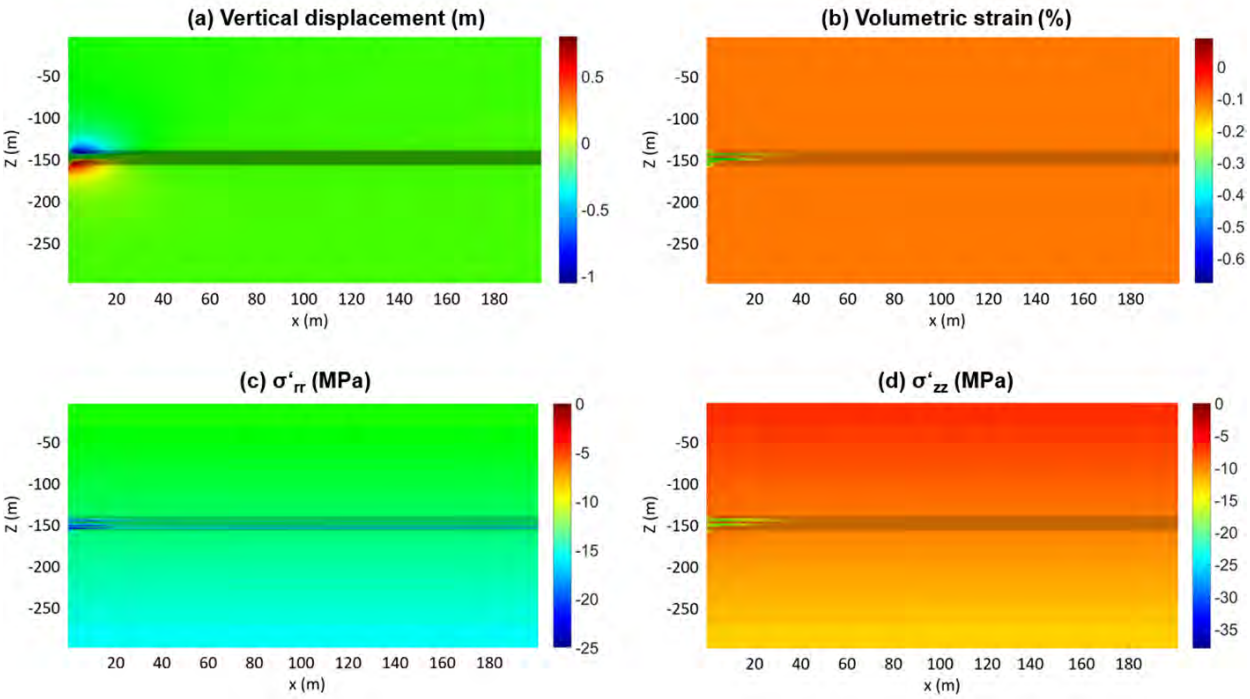

Figure 5.7: Distributions of (a) vertical displacement, (b) volumetric strain, (c) radial effective stress, and (d) vertical effective stress after 14-day production.

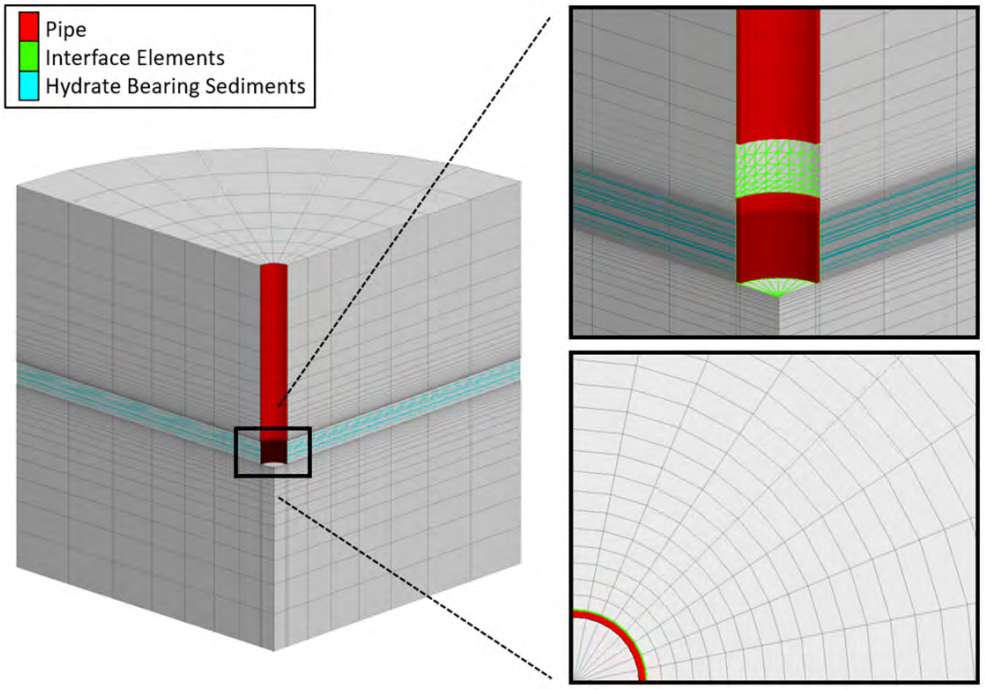

Figure 5.8: Description of simulation domain with pipe and interface elements.

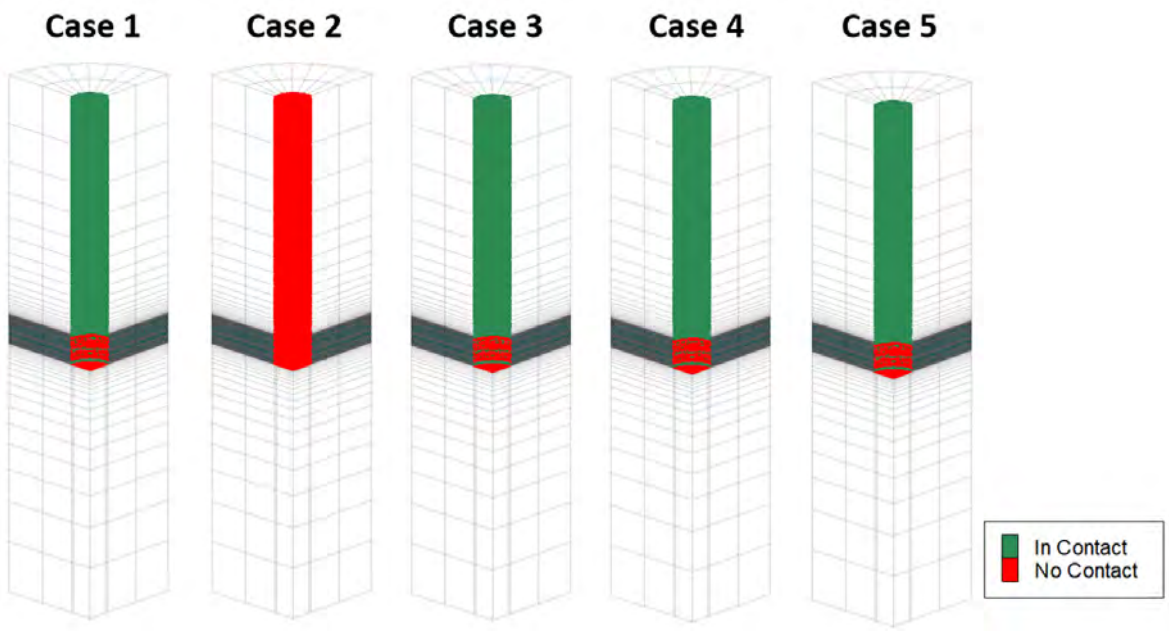

Figure 5.9: Normal Slip on the interface elements between the pipe and the formation after 25-day production.

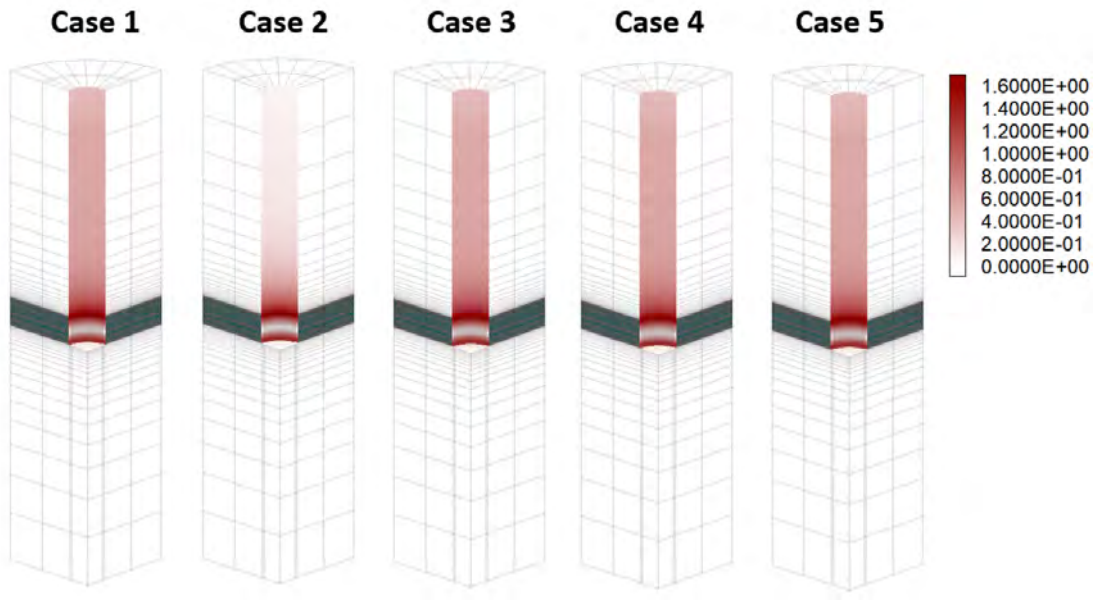

Figure 5.10: Shear slip displacement (m) along the interface elements for 5 test cases after 25-day production.

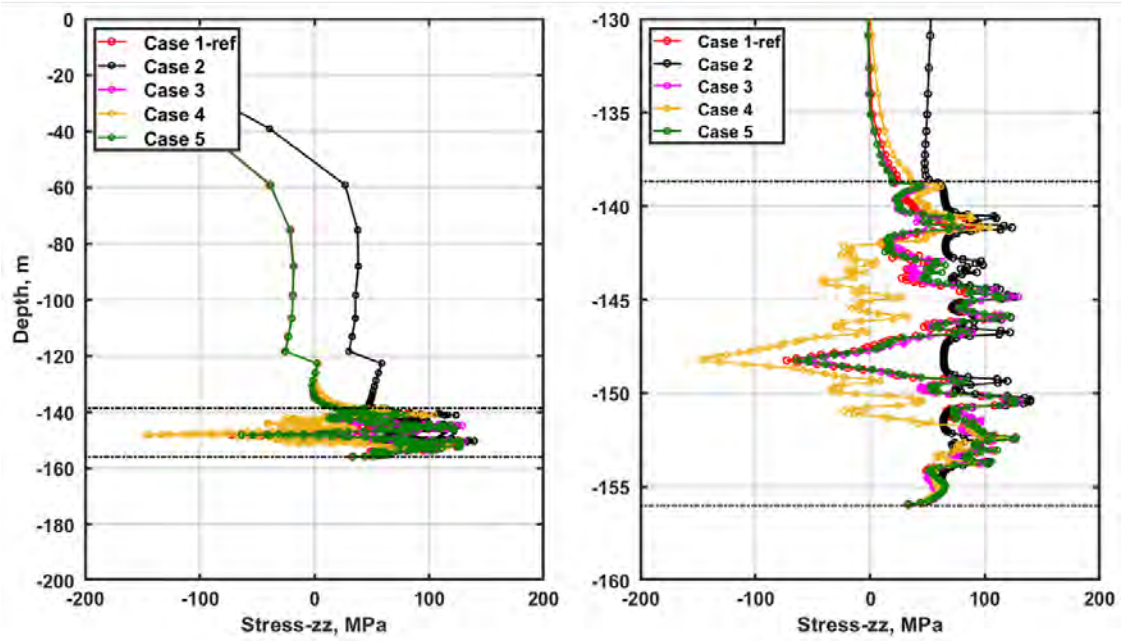

Figure 5.11: Vertical stress distribution along the vertical direction at the pipe.

5.2.2 Prudhoe Bay area on the North Slope (PBU-L106) in Alaska, USA.

There is a lot of published work [57] [123] on investigations relating to the flow performance and geomechanical response of vertical well production at Unit C of PBU-L106 site under constant pressure conditions with the depressurization method [124] [14]. We also employ a similar approach with different interface properties between the formation and the wellbore. This study has been done using a simulator capable of considering coupled flow and geomechanics (TOUGH+Hydrate-FLAC3D). From the numerical results presented below, we are able to observe a full range of different total stresses that are acting on the pipe element under different bonding scenarios between pipe and formation. These results allow us to design the pipe and casing properly.

5.2.2.1 Model description

The PBU-L-106 site is located on the North Slope of Alaska. The geology of the gas hydrate deposits in the North Slope of Alaska has been described in [57] and [124]. We slightly modify the simulation domain to have a smaller size for ease of flow simulation, specifically, a size of 500 m by 105.2 m, while for the geomechanics domain, a size of 1000 m by 800 m in r-direction and in z-direction, respectively is used. The grid sizes become smaller heading towards the wellbore and hydrate-bearing sediments as can be seen in Figure 5.12. We create 4270 gridblocks (i.e., 61 $\times$ 70 in radial r and vertical z directions, respectively) for the flow part and 182,528 gridblocks (i.e., 62 $\times$ 32 $\times$ 92 in radial r, azimuthal θ, and vertical z directions), this number includes the blocks representing the pipe.

Liquid water and hydrate saturation in Hydrate C1 and Hydrate C2 layer are 0.25 and 0.75 with porosity of 0.4, respectively. The interbedded shale layers contain only water with a porosity of 0.05. For this case, we assume that there is no capillary effect. Initial pressure distributes from 7.3 MPa (top layer of C2) to 7.7 MPa (bottom layer of C1). The initial total stresses are distributed from the surface (0 MPa) with the vertical gradient of -19.62 kPa/m and horizontal gradient of -15 kPa/m. Other properties are illustrated in Table 5.3.

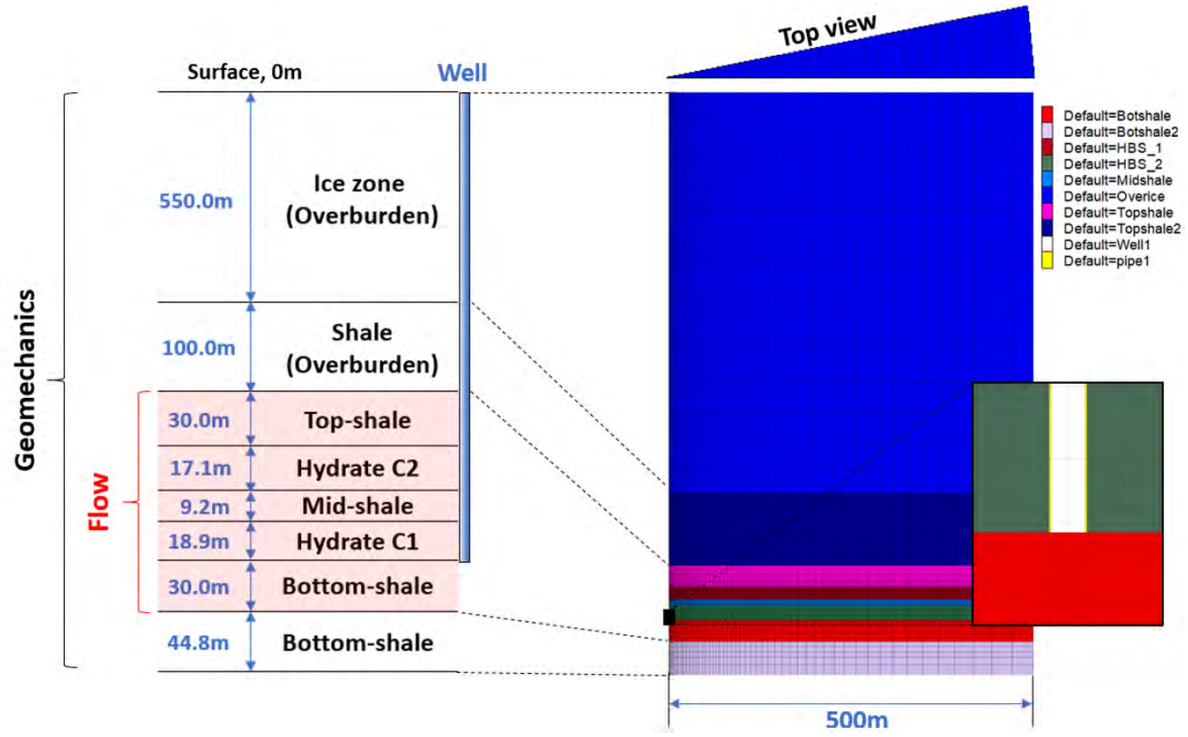

Figure 5.12: (Left) geological information of PBU-L106, (Right) discretized domain for flow and geomechanics.

Property	Overburden	Hydrate layer	Mud-Interlayer	Underburden	Unit
Drained bulk modulus, S_H=0%	95	95	95	95	MPa
Drained shear modulus, S_H=0%	87	87	87	87	MPa
Drained bulk modulus, S_H=100%	N/A	670	285	N/A	MPa
Drained shear modulus, S_H=100%	N/A	612	99.75	N/A	MPa
Permeability, S_H=0%	0	1.00E-12	5.00E-15	0	m^2
Initial porosity	0.05	0.4	0.05	0.05	

Table 5.3: Material properties of PBU-L106 site for flow and geomechanics.

5.2.2.2 *Simulation results*

Figure 5.13 shows distributions of pressure, water saturation, temperature, and hydrate saturation after 1-year of production. Despite of the depressurization, there is no dissociation of gas hydrates while there is an increase in hydrate saturation because of the pore size reduction shown in Figure 5.13. As shown in Figure 5.14, vertical displacement can be observed near the well and above the hydrate zone after 1 year because of the depletion, where the vertical displacement ranges up to -0.02m. Figure 5.14 also shows the distribution of volumetric strain, radial effective stress, and vertical effective stress. We identify significant compaction near the wellbore.

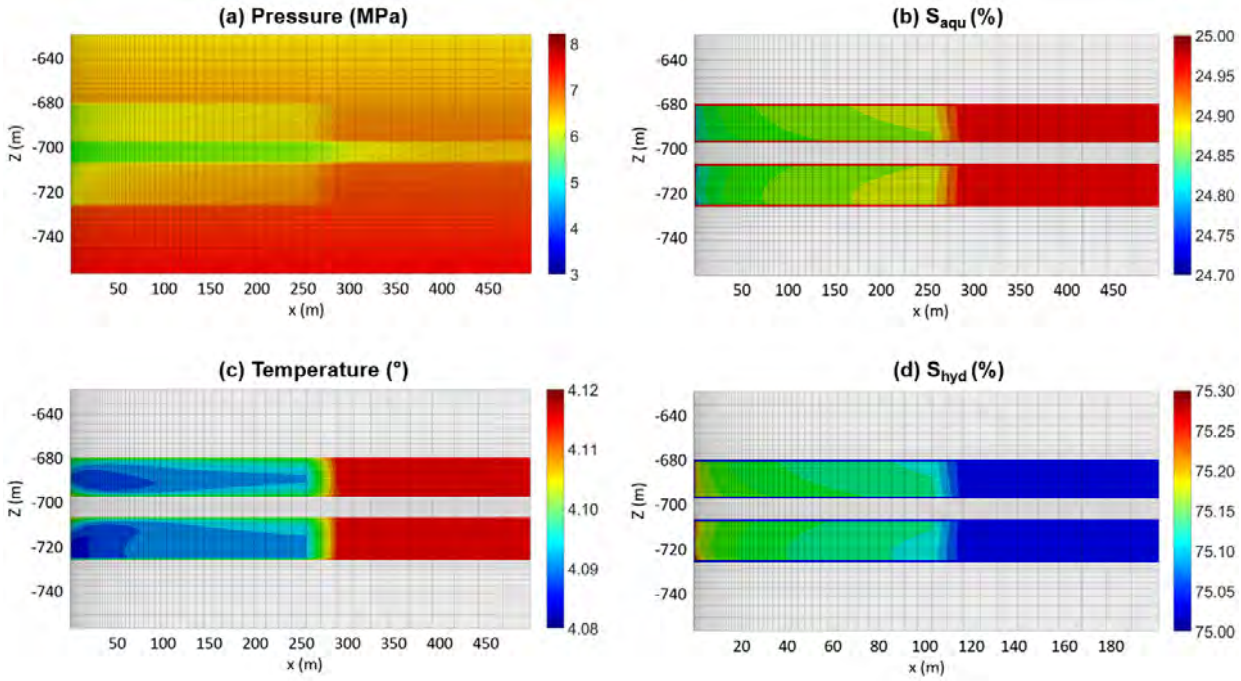

Figure 5.13: Distributions of (a) pressure, (b) gas saturation, (c) temperature, and (d) hydrate saturation after 1-year production.

As mentioned in the previous section, we study wellbore stability by taking the same 5 different cases. These cases have been shown in Table 5.2, each considers different proper-

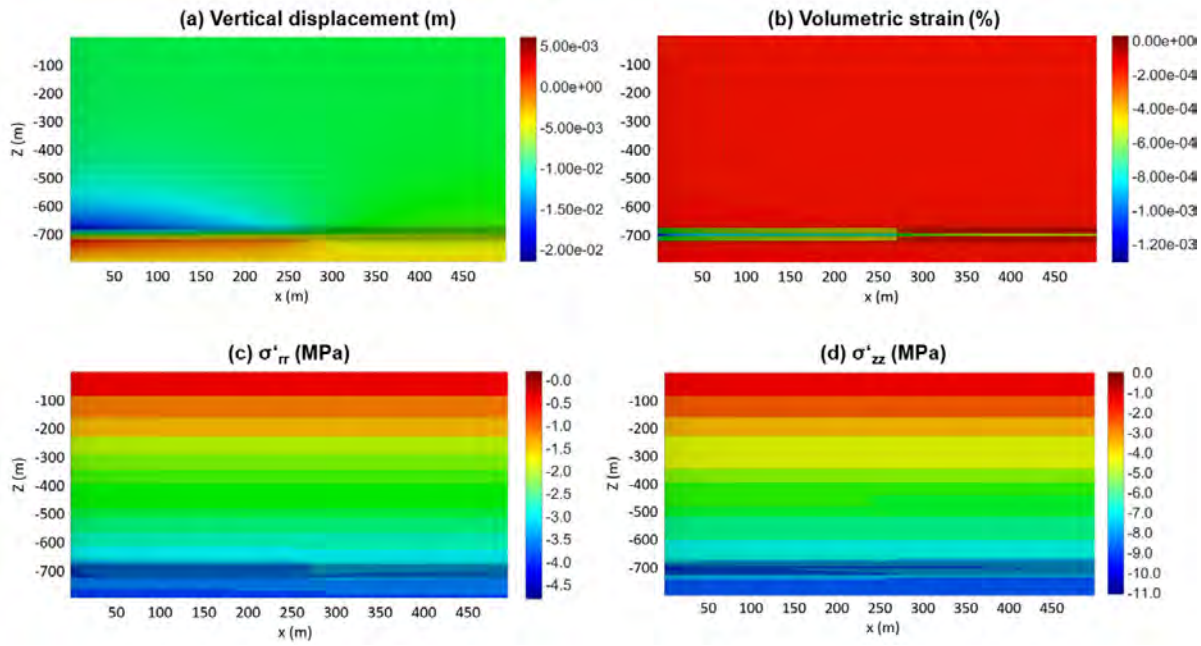

Figure 5.14: Distributions of (a) vertical displacement, (b) volumetric strain, (c) radial effective stress, and (d) vertical effective stress after 1-year production.

ties in terms of the interface elements to understand the impact of pressure depletion. The interface elements are located between the pipe and the formation as shown in Figure 5.15. We have a completely 3-dimensional domain for numerical simulation in geomechanics. This allows us to investigate the shear/normal slip status and displacement shown in Figure 5.16 and Figure 5.17, respectively. A single figure has been used to represent all 5 cases in terms of the slip status of the domain since they show almost similar trends in shear and normal slip. In Figure 5.18, we compare the vertical stress along the pipe for all 5 cases, results in these plots clearly reflect that under these states, the range of changes in vertical stress along the casing is not significant. To see more noticeable changes in vertical stress between these cases, a scheme that brings about more aggressive changes in this value should be used. However, such a methodology may not be very realistic given the values used in the studies that have been elaborated previously use more reliable values derived from laboratory tests. In conclusion, we can surmise that in the range of conditions possible within this system wellbore stability

should not be a major concern and it should be possible to start production with a properly planned well program. A major reason for the inference is that for all possible cases the stress changes are within the range of yield strength of 9 5/8" casing (perforated P-110 Grade pipe, 454.8 MPa).

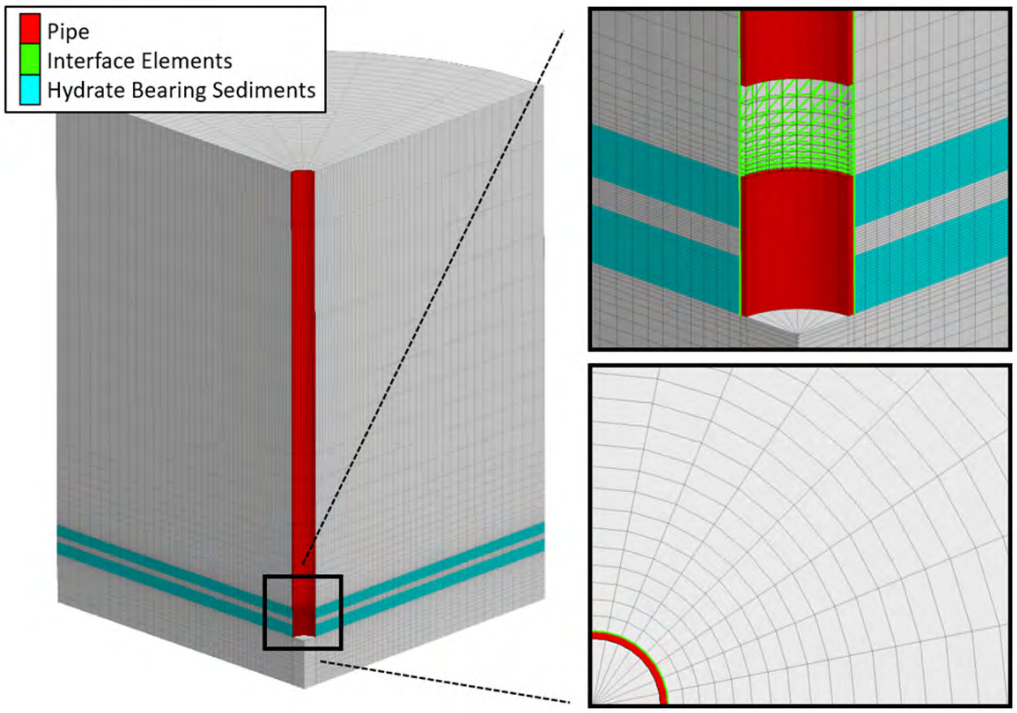

Figure 5.15: Description of simulation domain with pipe and interface elements.

5.3 Conclusion

The main purpose of this study is to evaluate the wellbore stability under depressurization-induced production from hydrate-bearing sediments while monitoring the effective stress along the wellbore by implementing discontinuous surfaces. The interface elements enable simulations of shear slip and normal detachment depending on shear and normal forces respectively, which are directly induced by dissociation of the hydrate layers. In this study, the effects of interface properties between the formation and wellbore are investigated. The shear and normal

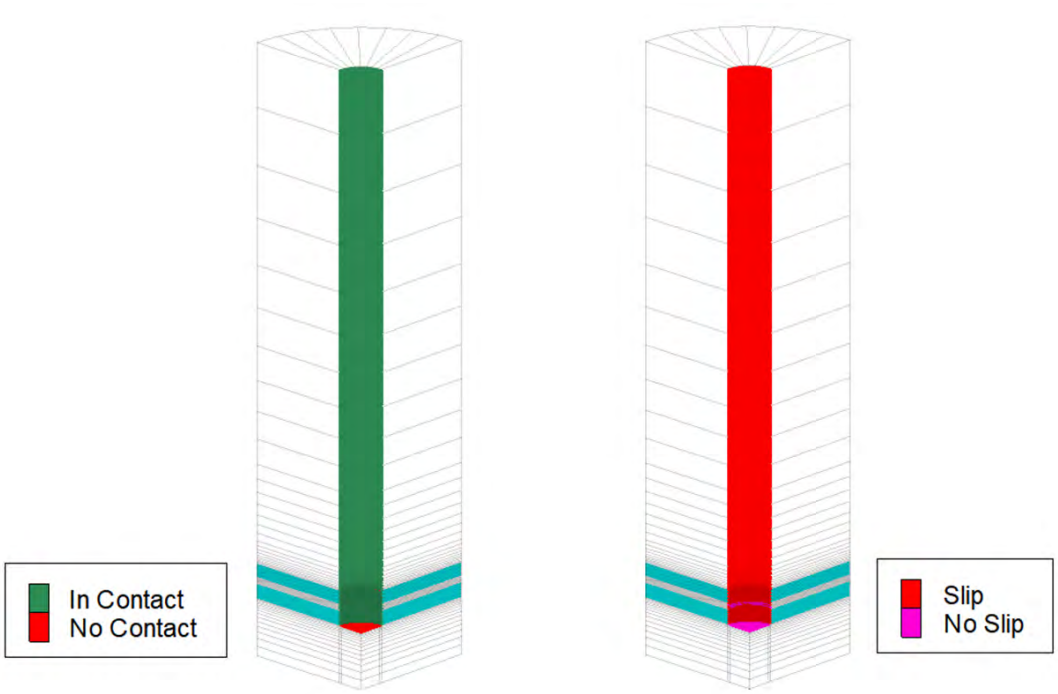

Figure 5.16: Slip status on interface elements between pipe and formation after 1-year production.

stiffness, tensile stress, cohesion, and friction angle between the interfaces are major factors that can be considered as the factors of sensitivity analysis. Among all the parameters, the shear stiffness has the greatest impact on stability as it affects subsidence and heaving around the zones of interest. The normal stiffness has a lesser influence on the development of the axial stress along the production pipe. An interesting insight from the study is how the regions with the greatest displacement are those right above and below the hydrate-bearing zones and not the zones in physical contact with the hydrate-bearing layers. In the two-way coupled flow geomechanics simulation process for modeling the methane production from hydrate-bearing sediments, two of the mechanical properties, shear, and bulk modulus, are associated with hydrate saturation. When dissociation begins and methane starts being produced, the bulk and shear moduli become smaller because the hydrate exists as a solid material in place. In other words, the structure of the solid skeleton becomes more fragile to have a greater value of dis-

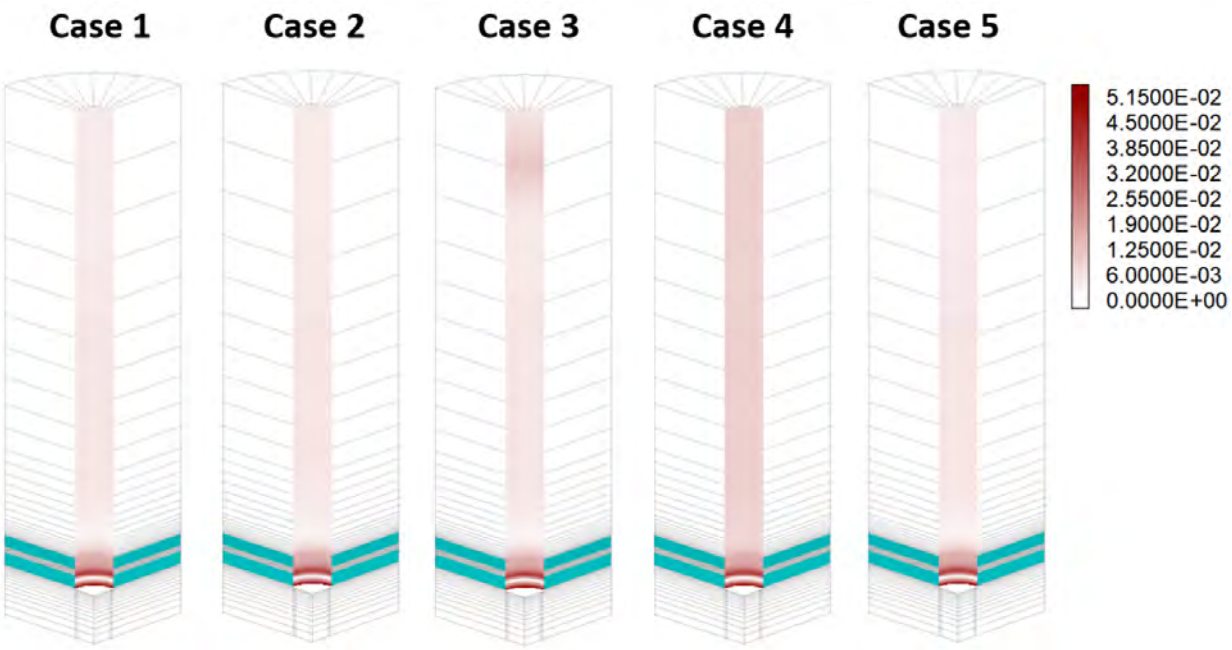

Figure 5.17: shear slip displacement along the interface elements with different properties after 1-year production.

placement. As the effective stresses along the production pipe increase, slippage occurs due to shear failure and the axial stress on the pipe reaches its maximum value after this failure. The possibility of mechanical failure is therefore a major concern that should be evaluated in detail for methane production from hydrate-bearing sediments. The axial failure of the pipe with the development of axial stress is the first failure criterion of concern that can engender various risky situations leading to pipe failure, induced by the frictional forces that draw or push the pipe. The next consideration for failure is the slippage and normal detachment between the formation and the wellbore. Both cases might cause the leakage of the methane gas to the surface or potential contamination of the nearby groundwater.

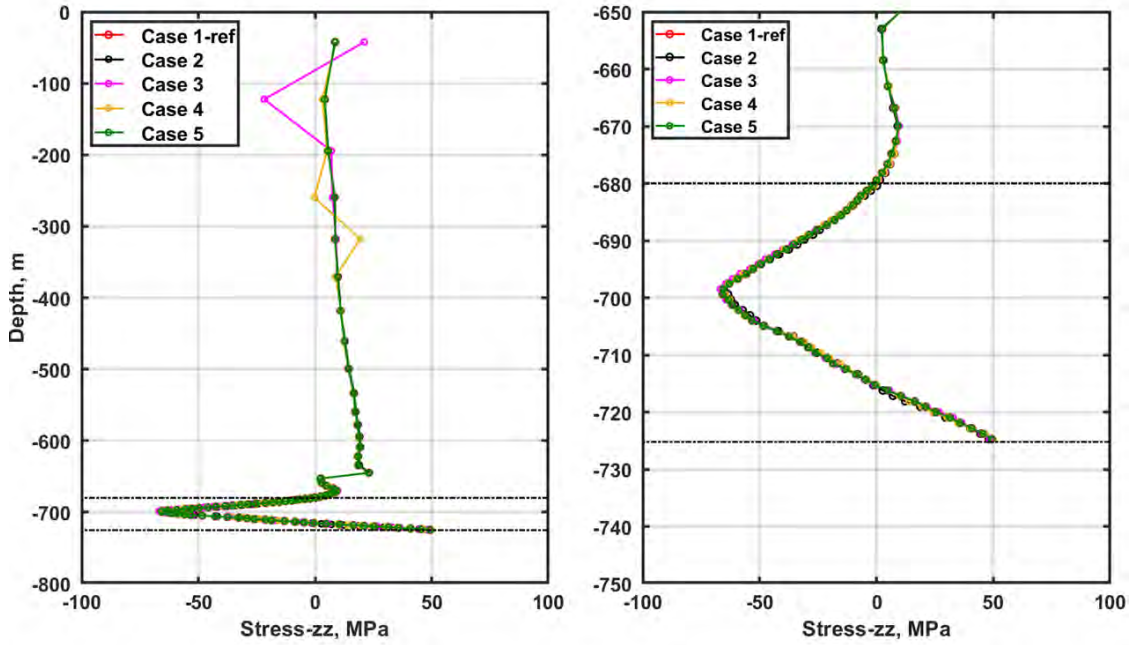

Figure 5.18: Total vertical stress distribution along the vertical direction at the pipe after 1-year production.

6. ALL-WAY COUPLED MULTIPHASE FLOW AND GEOMECHANICS IN A BI-WING HYDRAULICALLY FRACTURE SYSTEM.

We investigate the effects of coupled multiphase flow and geomechanics in the hydraulically fractured reservoirs numerically. We account for poromechanics of flow within a discrete fracture for rigorous simulation, considering both fluid compressibility and fracture volume change. We newly propose a numerically stable sequential method for all-way coupled geomechanics and flow for the discrete fractured systems. The stabilization term is dynamic, depending on the fracture length, and the numerical results support good stability and convergence of the proposed sequential method for hydraulic fracturing simulation. From numerical experiments, we identify at the fracture tip the vacuum area where pressure is below the initial reservoir pressure as well as the dry zone where gas saturation is high. The existence of the vacuum area is fundamentally due to different time scales between flow and geomechanics, which can be considered as the Mandel-Cryer effect in the fractured systems. The dry zone is not necessarily identical to the vacuum area. The reservoir gas can be introduced into the fracture substantially when the reservoir is highly permeable. The vacuum area and the dry zone can be prominent in naturally or previously hydraulically fractured reservoirs. We study the system responses of fracture propagation by varying parameters of flow and geomechanics. The hydraulic fracture propagates slowly when reservoir permeability or fracture toughness is high, when Young's modulus is low, or when the initial total stress is higher than the initial reservoir pressure.

6.1 Vacuum area, dry zone, and fluid lag

Injection into the fracture including hydraulic fracturing induces the instantaneous opening at the fracture tip due to the nature of quasi-static geomechanics, which accordingly results in pressure drop at the fracture tip instantaneously because of fluid compressibility and the

undrained condition (Figure 6.1). These different time scales between geomechanics and fluid flow might induce the significant vacuum area near the fracture tip followed by the dry zone and fluid lag, particularly in the case of injection into natural fractures and/or pre-existing hydraulic fractures. In other words, when the fracture begins to open, reservoir gas can possibly be invaded into the fracture tip from the reservoir due to the pressure gradient induced by the pressure drop at the tip while the fracture conductivity is still low because the fracture aperture at the fracture tip is small. This physical behavior is opposite to the leak-off of the injected fluid into the reservoir. Furthermore, the existence of the dry (gas) zone affects relative permeability, and thus the flow of the injected fluid becomes slow. On the other hand, the gas volume within the fracture might become larger, which might subsequently cause more fluid-lag. This invaded gas can also affect the residual saturation of gas and water and their relative permeability, which can trap the injected water within the fracture when the water is withdrawn.

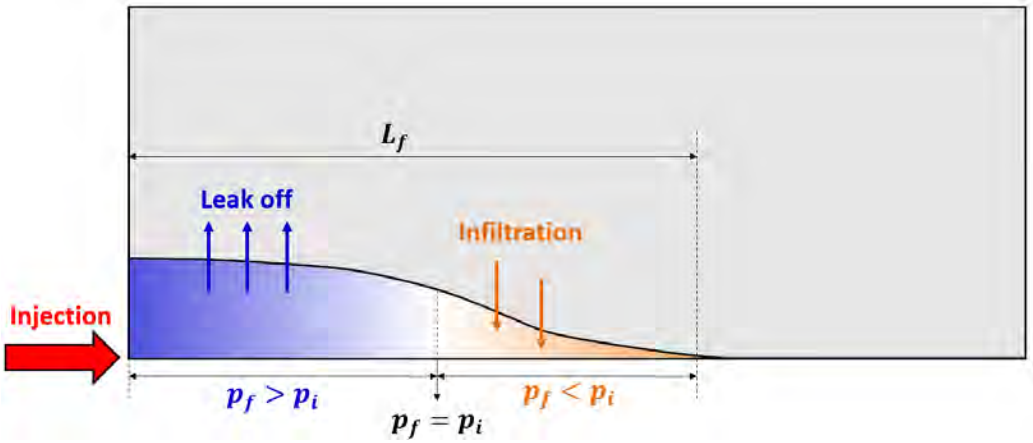

Figure 6.1: Flow behavior near the fracture tip. p_f and p_i are the fluid pressure and initial fluid pressure within the fracture, respectively.

6.2 Model description

We describe a reference case problem of the numerical experiments as follows. We consider the 2D plane strain geomechanics domain (the upper and right quadrant of Figure 2.3), discretized with 30×3 gridblocks in the x and y directions, respectively, as illustrated in Figure 6.2. Gridblock sizes in the x direction are Δx = 1.0 m from the 1st to 10th gridblock, Δx = 10.0 m from the 11th to 20th gridblock, and Δx = 100.0 m from the 21st to 30th gridblock, respectively. Gridblock sizes in the y direction are uniform (i.e., Δy = 5 m). The traction of 10 MPa is applied at the top of the domain while no horizontal displacement is imposed to the left and right sides. At the bottom, we take no vertical displacement boundary condition except the fractured boundary area where the traction is determined by the fluid pressure within the fracture. The initial total stresses in the x and y directions are both 10 MPa. Also, initially, we have a pre-existing small fracture at the left-bottom corner, the length of which is 1.0 m for the reference case. The reservoir takes Young's modulus (E) of 25 GPa and Poisson's ratio (ν) of 0.25, respectively.

The Biot coefficient b is 1.0. The fracture toughness is 1.0 MPa·$\sqrt{m}$ unless otherwise noted. The domain for the multiphase flow problem is different from that of the geomechanics problem (Figure 6.2). It is discretized with 10×4 gridblocks in the x and y directions, respectively. The gridblock sizes in the x mesh in the y direction refined near the fracture, which has Δy = 10^{-4} m, 4 × 10^{-4} m, 9.5 × 10^{-3} m, 4.99 m from the fracture. Thus, the lengths of the flow domain in the x and y directions are L_x = 10 m and L_y = 5 m, respectively. We take no-flow boundary condition at all the boundaries. Initial gas pressure and water saturation are p_g = 10 MPa and S_w = 0.3, except S_w = 1.0 for single phase flow of water. We take gas pressure and water saturation as primary variables. Gas and water generally represent the non-wetting and wetting fluid phases, respectively and thus they do not strictly follow the specific properties of gas and water. The density viscosity of water are $\rho_{w,0}$ = 1000 kg m^{-1} and μ_w = 10.0 cp (10^{-2} Pa·s), respectively. The density viscosity of gas are $\rho_{g,0}$ = 100 kg

m^{-1} and μ_g = 0.01 cp. The reservoir permeability is k_p = 0.005 mD, unless otherwise noted, and the initial porosity is ϕ_0 = 0.1. The relative permeability of water and gas are $k_{r,w}$ = (S_w - $S_{r,w}$)^4 and $k_{r,g}$ = (S_g - $S_{r,g}$)$^{1.5}$, where the irreducible saturation of water and gas are $S_{r,w}$ = 0.19 and $S_{r,g}$ = 0.15, respectively. The compressibility of water and gas are c_w = 4.0$\times 10^{-10}$ Pa^{-1} (almost incompressible) and c_w = 4.0 $\times 10^{-8} Pa^{-1}$ (highly compressible), respectively. The water is injected at the bottom-left corner, where the rate is Q_w = 0.01 kg/s. The time step size is uniformly Δt = 1.0 s. We neglect gravity and capillarity.

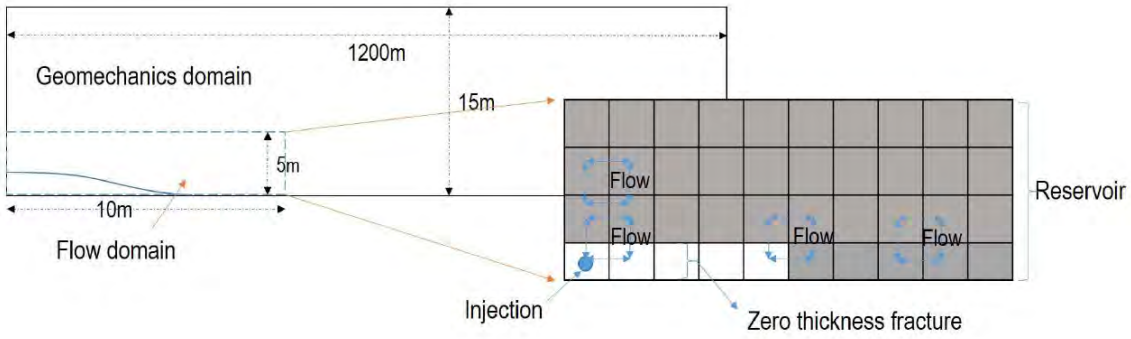

Figure 6.2: Domain for the numerical experiments. The fracture gridblocks increase dynamically as fracturing occurs.

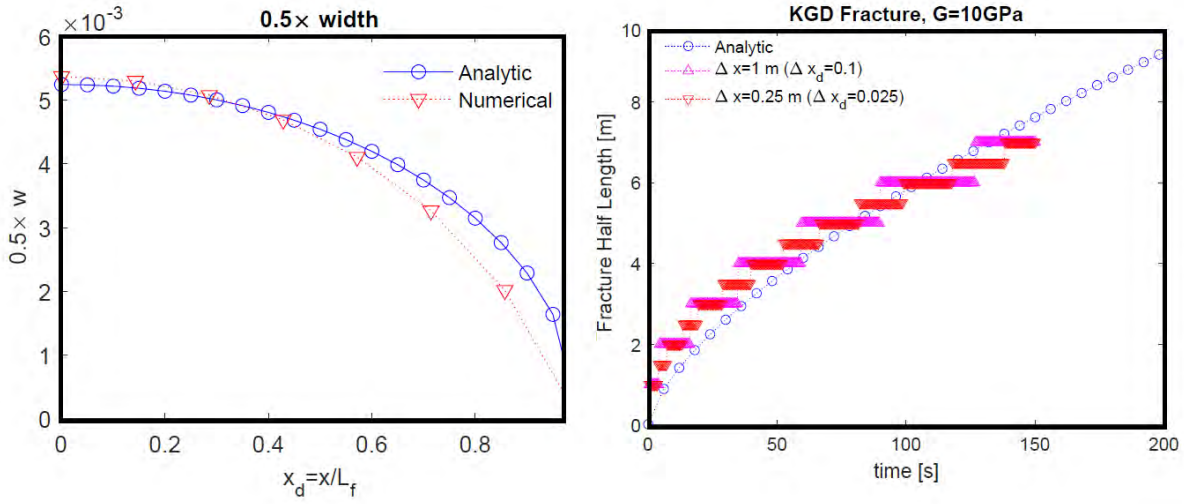

Figure 6.3: (Left) Static fracture opening. (Right) Fracture propagation within an impermeable reservoir under the plane strain geomechanics.

6.3 Validation

We consider two cases for verification where analytic solutions are available: The opening of a static fracture (Sneddon's solution) [125] and propagation of a hydraulic fracture (KGD fracture) [126], where single phase flow of water with an impermeable reservoir is considered. Figure 6.3 shows the comparison between numerical results and the analytical solutions for the two cases. The left figure shows the fracture opening for a given constant net pressure of 10 MPa over the fracture in order to verify the geomechanics-only simulator. The right figure shows the fracture propagation to validate the coupled flow-geomechanics simulator for hydraulic fracturing, where K_{IC} = 15 MPa$\cdot\sqrt{m}$, a toughness-dominated system. The stepwise evolution of the fracture propagation is due to space discretization. We identify that the numerical results are in good agreement with the analytical solutions. The solution from the refined fracture mesh with Δx = 0.25 m still shows a converged solution, matching the analytical solution (the right figure).

6.4 Numerical simulation

6.4.1 Static fracture opening

We investigate physical responses on the fracture opening of a static (stationary) fracture, the length of which is L_f = 10m. This process represents restimulation of natural fractures or existing hydraulic fractures by injection of water. Figure 6.4 shows pressure behavior as well as the corresponding fracture opening at the different monitoring points for single phase flow, where water is fully saturated. While pressure at the injection point is above the initial reservoir pressure, the pressures at the two other monitoring points away from the injection decrease below the initial pressure at the early time when the apertures at the points begin to open. At the onset of fracture opening, the flow system is still in the undrained condition while the fracture volume increases. As a result, pressure decreases due to fluid compressibility at the early time. At the late time, the injected fluid flows into the opened fracture, which eventually increases the pressure. We emphasize that this physical behavior is fundamentally due to different time scales between fluid flow and geomechanics, same as the Mandel-Cryer effect observed in the multi-dimensional poromechanics problems although the pressure hump is opposite, which can only be accurately captured by rigorous all-way coupled simulation that accounts for both fluid compressibility and fracture volume change. We identify the same physical behavior in multiphase flow, where gas and water coexist. In Figure 6.5, the pressure away from the injection point decreases below the initial reservoir pressure at the early time when the fracture opens. Accordingly, shown in the right of Figure 6.5, water saturation in the area far from the injection point decreases due to gas infiltration induced by the pressure gradient between the fracture and the reservoir as well as the high mobility of reservoir gas. The degree of pressure drop at the early time might possibly affect reservoir thermodynamic properties mutually such as compressibility and phase behavior in a multi-component hydrocarbon system. For example, the oil phase can be changed to the gas phase when the pressure drops below the bubble point even for an oil reservoir.

Figure 6.6 shows the evolution of pressure and water saturation at the reservoir. Pressure near the fracture behaves similar to that at the fracture while it does not change away from the fracture due to a short period of injection. We identify pressure drop at the onset of fracturing opening near the fracture, too. On the other hand, the response of water saturation is slower than that of pressure. The leak-off of water to the reservoir formation is only found very next to the fracture while water saturations away from the fracture are unchanged. The non-uniform behaviors of pressure and saturation are due to different time scales among geomechanics, pressure diffusivity, and saturation propagation. In other words, the geomechanics system responds immediately, the pressure diffusion follows next, and the saturation field changes slowly.

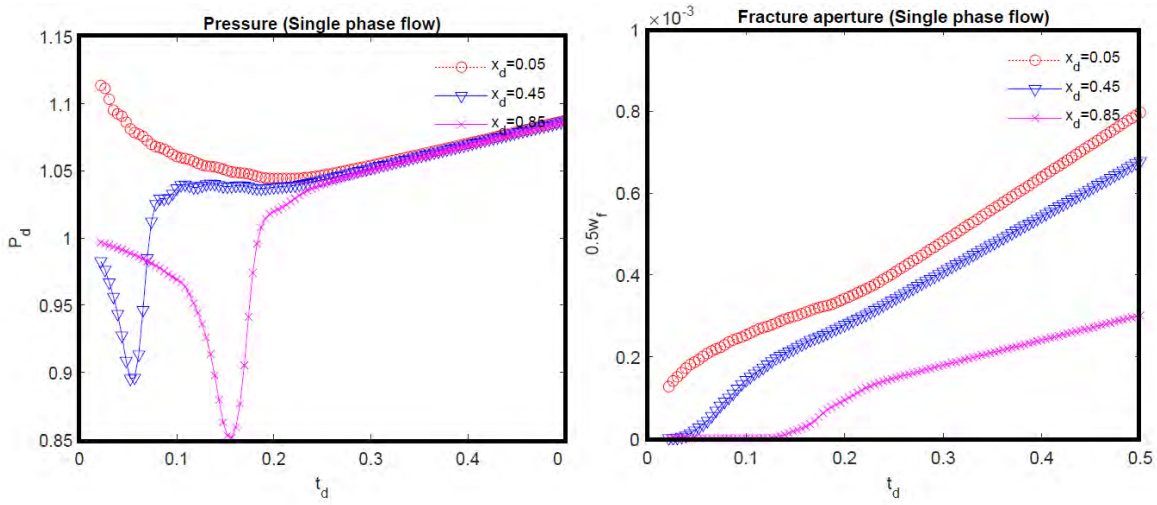

Figure 6.4: Evolution of pressure (left) and the aperture (right) at different monitoring points within the fracture in the case of single phase flow. $t_d = Q_w \times t/M_i$, where M_i is a total amount of fluid mass in the reservoir at the initial time.

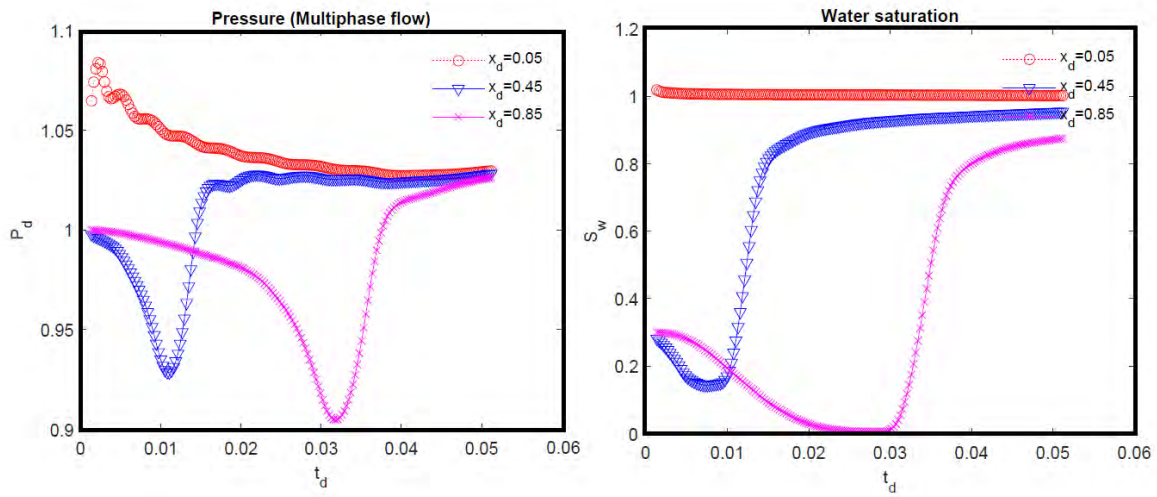

Figure 6.5: Evolution of pressure (left) and water saturation (right) at different monitoring points within the fracture in the case of multiphase flow.

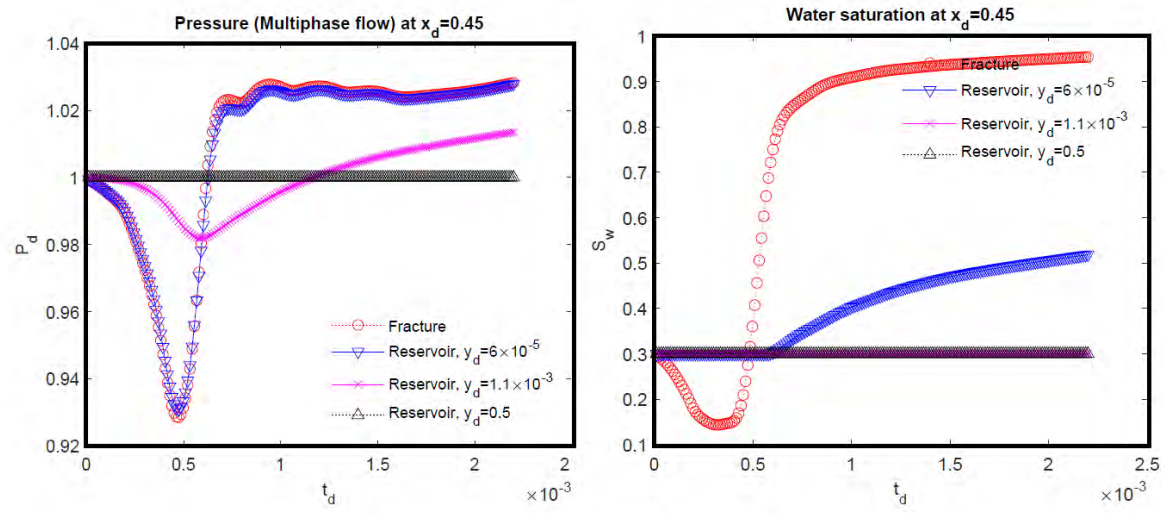

Figure 6.6: Evolution of pressure (left) and water saturation (right) in the reservoir. $y_d = y/L_y$.

6.4.2 Stability of the sequential implicit method

We investigate stability behavior of the sequential method, taking single phase flow of water with an impermeable reservoir and considering two static fractures (L_f = 1 m and L_f = 10 m). Estimation of K_{dr}^{fr} becomes a critical role for numerical stability of the sequential method. As aforementioned, K_{dr}^{fr} of the flow problem is not constant even in the linear elastic problems, being dependent on length of the fracture. Figure 6.7 shows evolution of pressure during iteration for for the two different sizes of the static fractures. The pressure solution is stable for L_f = 1 m when K_{dr}^{fr} = 3.33 MPa. But it becomes unstable for the same K_{dr}^{fr} when L_f = 10 m. These results show that it is necessary to consider the fracture length to determine an appropriate K_{dr}^{fr} for stability of the sequential method. The numerical results in Figure 6.8 support estimation of $\bar{K}_{dr}^{fr}$ in Equation 2.21, providing numerical stability for both L_f = 1 m and L_f = 10 m. One might introduce a multiplier β^c with $\bar{K}_{dr}^{fr}$ to accelerate the rate of convergence (i.e.,$K_{dr}^{fr} = \beta^c \bar{K}_{dr}^{fr}$). For both fracture lengths, convergence becomes faster when β^c = 2. But it becomes unstable when β^c = 10. Also, β^c = 5 causes slight oscillation although it yields fast convergence.

We will study in-depth stability analysis and an optimal choice of β^c (or K_{dr}^{fr}) for convergence in the future. In this study, we take K_{dr}^{fr} = $\bar{K}_{dr}^{fr}$ with a fixed number of iterations, 20. This iteration number provides sufficient accuracy comparable to the fully implicit method. We can also identify validity of K_{dr}^{fr} = $\bar{K}_{dr}^{fr}$ from the right of Figure 6.3, which provides numerical stability of the KGD fracture propagation.

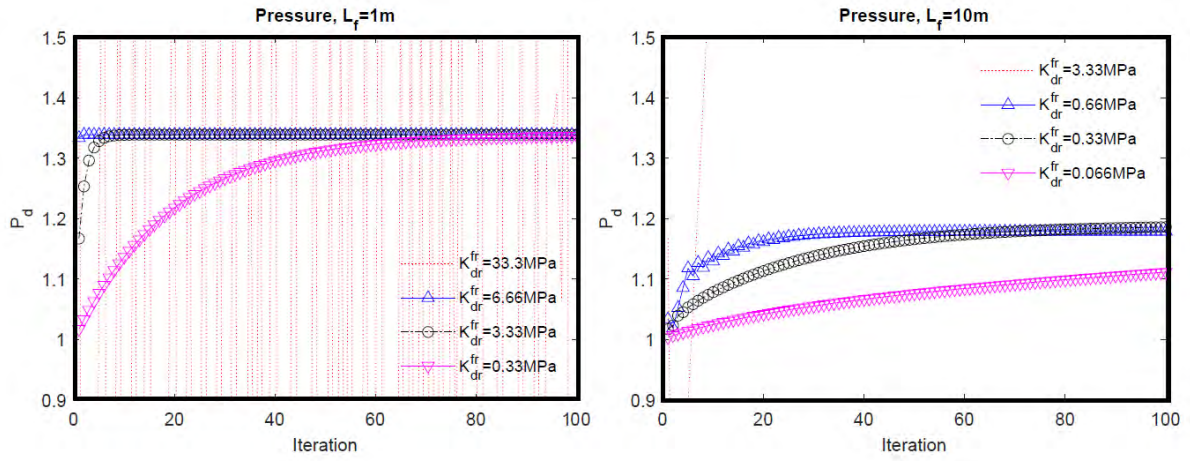

Figure 6.7: Evolution of pressure during iteration with various constant K_{dr}. (Left) L_f = 1 m. (Right) L_f = 10 m.

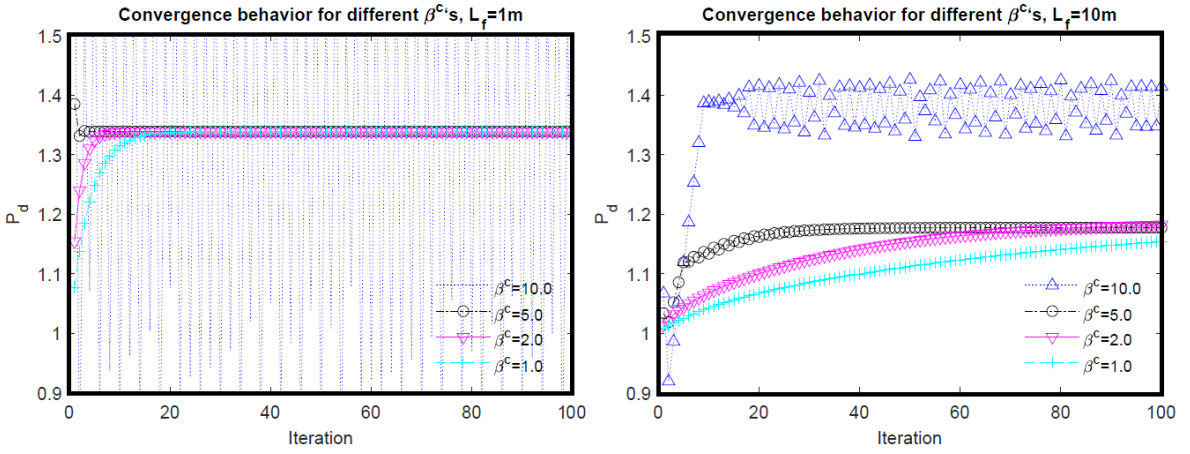

Figure 6.8: Evolution of pressure during iteration with various constant β^c. (Left) L_f = 1 m. (Right) L_f = 10 m.

6.4.3 Hydraulic fracture propagation

We investigate physical responses of coupled flow and geomechanics during hydraulic fracturing processes, varying several parameters such as far-field total stress (Case 1), reservoir

permeability (Case 2), Young's modulus, and reservoir toughness of the reservoir (Case 3).

- Reference case: We find from the numerical results shown in Figure 6.9(a) that pressure drops every time when the fracturing occurs. The pressure fluctuation is noticeable at the early time due to small fracture volume, but it quickly disappears afterward as the fracture volume increases [127] [82] [71]. As observed previously in the static fracture case, the pressure next to the injection point drops below the initial pressure at the very early time (Figure 6.9(b)), and it becomes recovered rapidly. We can identify this pressure behavior from Figure 6.10, where the pressure at the fracture tip at the early time is lower than the initial pressure. We also find that water saturation at the fracture tip is also lower than the initial water saturation (Figure 6.9(c) and Figure 6.10). These responses of pressure and water saturation can support the argument of the vacuum area and the dry zone, fundamentally the Mandel-Cryer effect during hydraulic fracturing processes. We refine the gridblocks in the x direction in order to test convergence behavior for fracture propagation by taking a smaller size of the gridblocks, Δx_d = 0.025 (Δx = 0.25 m), and then compare the numerical results of the reference case with those from the refined mesh. From Figure 6.11, we identify convergence of both pressure and fracture propagation when the refined mesh is employed, as shown in Dean and Schmidt [128]. We also identify from Figure 6.12 that both pressure distributions from the refined mesh at the early and late times match those from the reference case, still showing the vacuum area near the fracture tip.

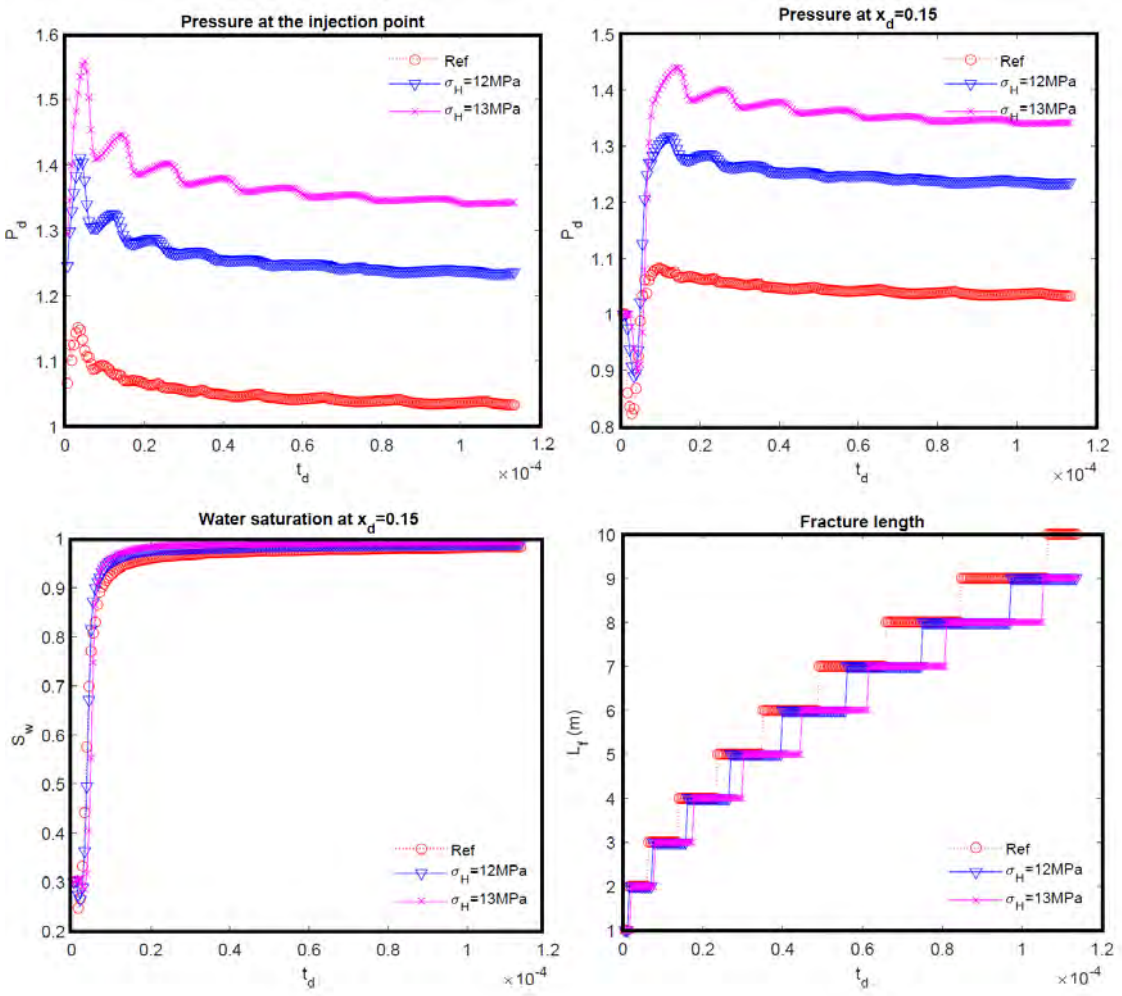

Figure 6.9: Results of the reference case (Ref) and different σ_H case (Case 1). (a) Pressure at the injection point. (b) Pressure at $x_d = 0.15$. (c) Water saturation at $x_d = 0.15$. (d) Fracture half length. σ_H is the side burden, far-field total stress. $x_d = x/L_x$.

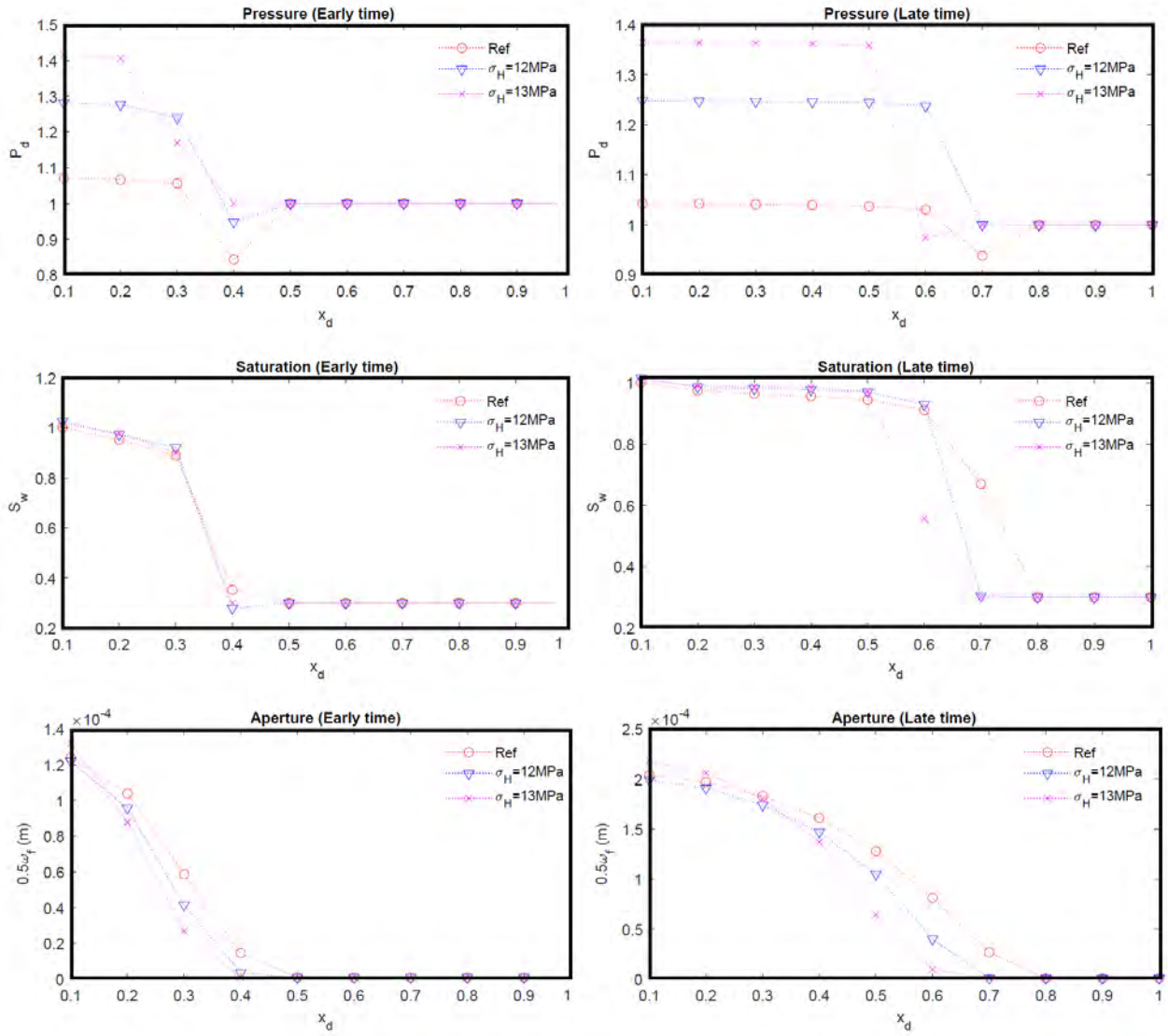

Figure 6.10: Distribution of flow and geomechanics variables at the early and late times (t_d = 1.62×10^{-5} and t_d = 5.41×10^{-5}, respectively) for the reference case and Case 1. x_d = x/L_x.

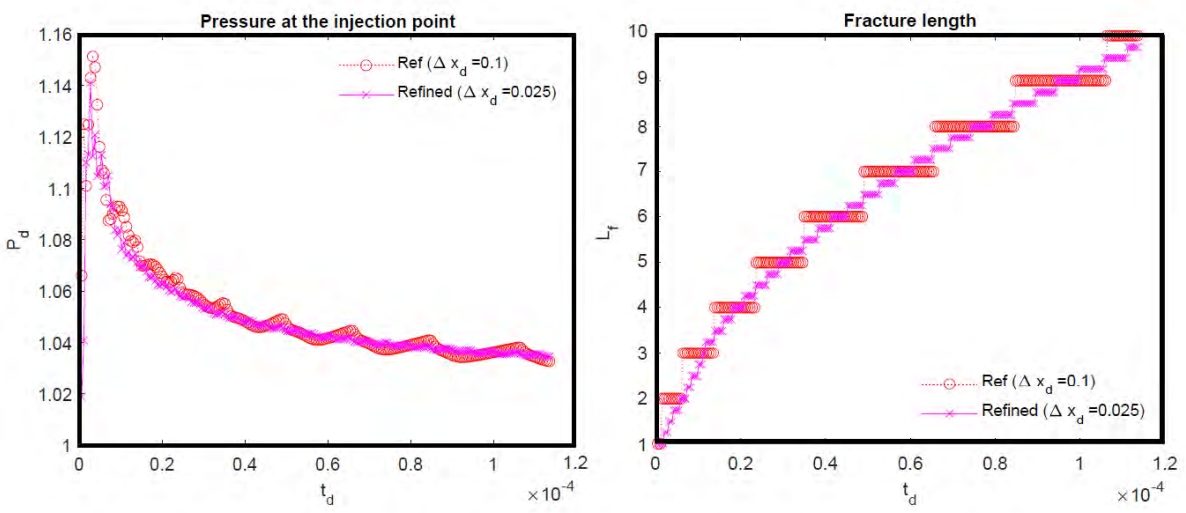

Figure 6.11: (Left) Convergence of pressure and (Right) fracture propagation.

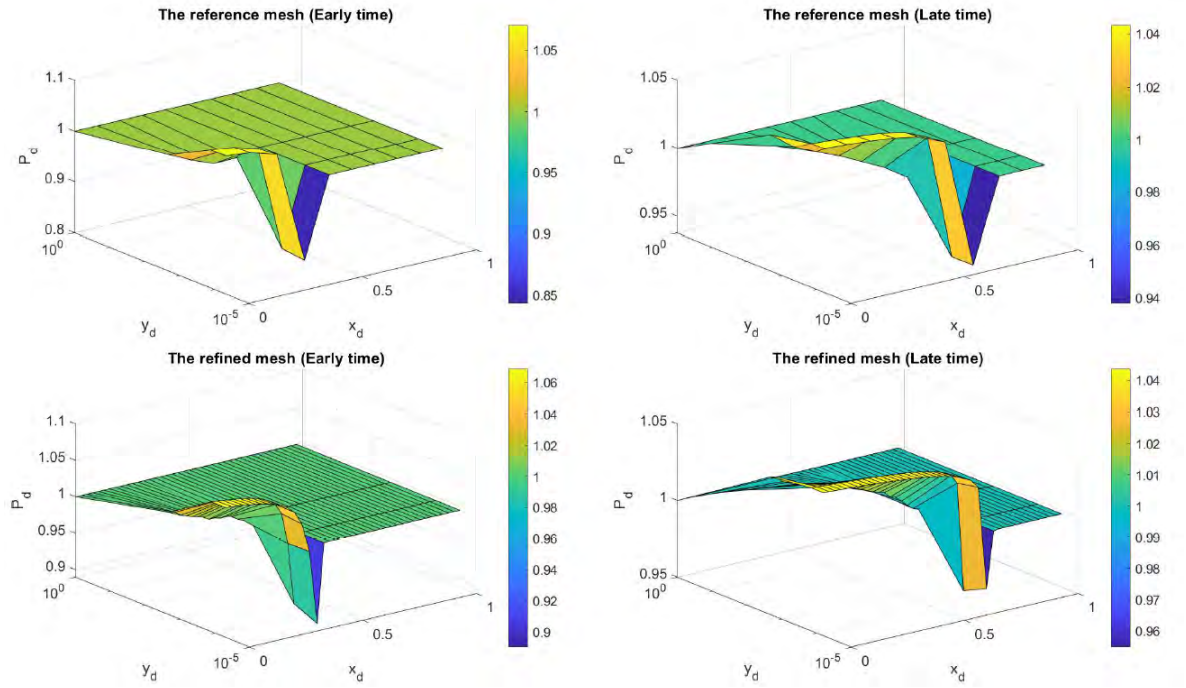

Figure 6.12: Pressure distribution with the reference (top) and refined meshes (bottom) at the early (left) and late (right) times. We take the logarithmic scale in the y direction for visualization.

- Case 1-initial total stress: When the far-field total stress (σ_H) is greater than the initial pressure, hydraulic fracture propagation becomes slower than that of the reference case (Figure 6.9(d) and Figure 6.10) because the stress intensity factor at the fracture tip increases more slowly as well as because the fracture opening becomes smaller, which causes low permeability.

- Case 2-reservoir permeability: Figure 6.13 shows evolution of pressure and water saturation at xd = 0.15 when we additionally consider higher and lower permeabilities than the reference permeability (i.e., k_p =0.5 mD and k_p = 5.0 $\times$ 10^{-6} mD, respectively). Figure 6.14 shows distributions of the pressure and the fracture aperture. We find that the hydraulic fracture propagates slowly due to the leak off of the water into the reservoir in the case of high reservoir permeability, which causes slow pressurization of the fracture whereas the fracture propagates fast when the permeability is low. We also find that the pressure decreases below the initial pressure more substantially for the low permeability case when the fracture tip begins to open because the area at the fracture tip keeps more undrained condition (Figure 6.13(left) and Figure 6.14). In this case, even though the pressure drop causes a larger pressure gradient between the reservoir and the fracture tip, we cannot find gas influx into the reservoir because of the low reservoir permeability (Figure 6.13 (right)). On the other hand, in the case of high permeability, water saturation decreases substantially at the fracture tip when fracture opens, which implies gas infiltration from the reservoir. It is found from Figure 6.13 and Figure 6.14 that the low reservoir permeability causes more pressure drop and faster fracture propagation due to no leak-off to the reservoir formation. We find from Figure 6.15 that the responses of pressure and saturation are similar to those shown in the static fracture case. Reservoir pressure near the hydraulic fracture decreases at the onset of the fracture opening. Afterward reservoir pressure increases due to water influx from the injection.

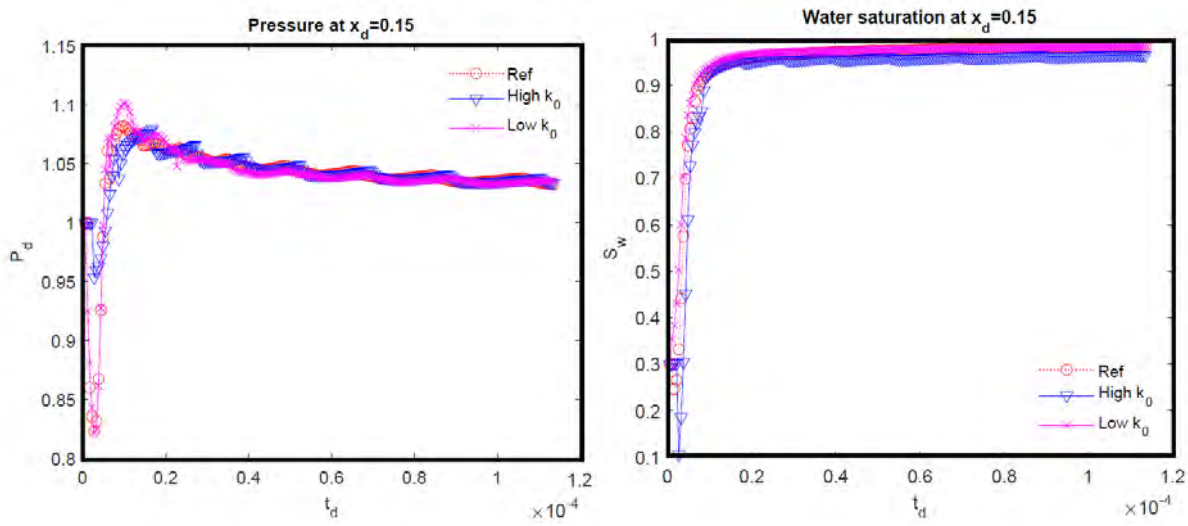

Figure 6.13: Evolution of pressure (left) and water saturation (right) at x_d = 0.15 for the case of different reservoir permeabilities (Case 2).

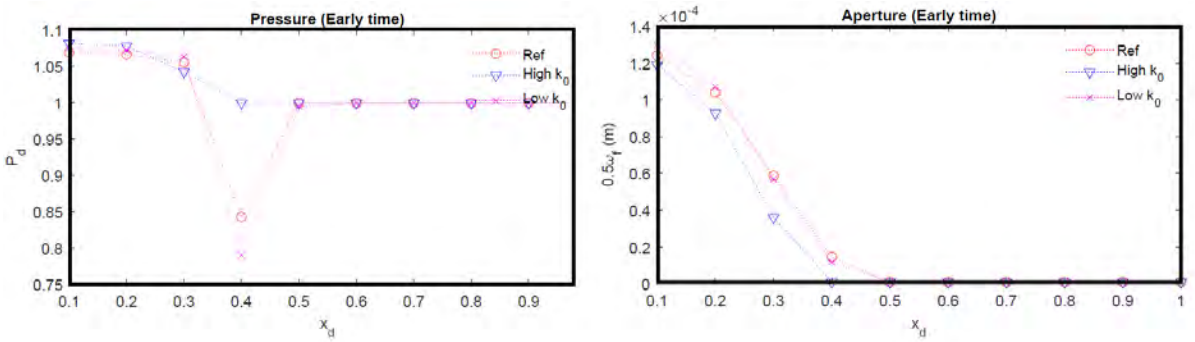

Figure 6.14: Distribution of pressure (left) and the fracture aperture (right) at $t_d = 1.62\times10^{-5}$ for Case 2.

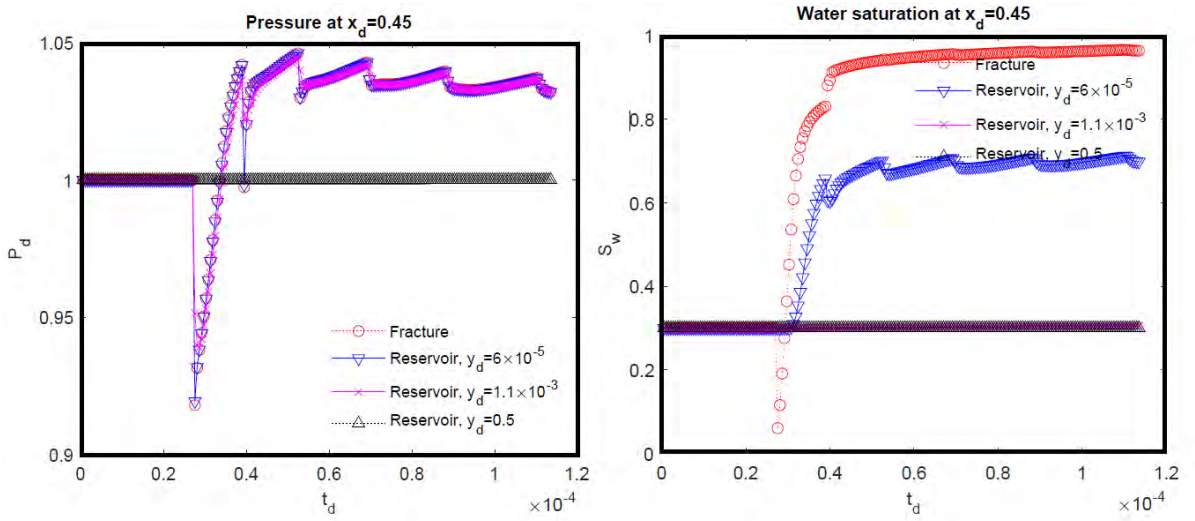

Figure 6.15: Evolution of pressure (left) and water saturation (right) at x_d = 0.45 for the high permeability reservoir case.

- Case 3-Young's modulus and toughness: We analyze the sensitivity of geomechanics properties of the reservoir, which mainly affects the fracture opening. Low Young's modulus induces more deformation of the fracture, which leads to high total compressibility of the fracture. As a result, pressurization with the fracture becomes slow, which results in slow fracture propagation (Figure 6.16). Additionally, lower Young's modulus yields a larger fracture opening followed by higher conductivity. Hence, the flow of the injected water becomes faster than that of the reference case, and water saturation does not drop below the initial saturation even though we still identify the pressure drop at the fracture tip (Figure 6.17).

Toughness of the reservoir rock determines rock failure induced by hydraulic fracturing. We find from Figure 6.16 (right) that low toughness causes fast fracture propagation. Figure 6.18 further shows the comparison of toughness between the reference case and the high toughness case. We identify from the figure that high toughness yields slow fracture propagation. Considering that the same amount of water is injected, this high toughness requires higher

pressurization for fracturing, which also induces a larger fracture opening, similar to the low Young's modulus case.

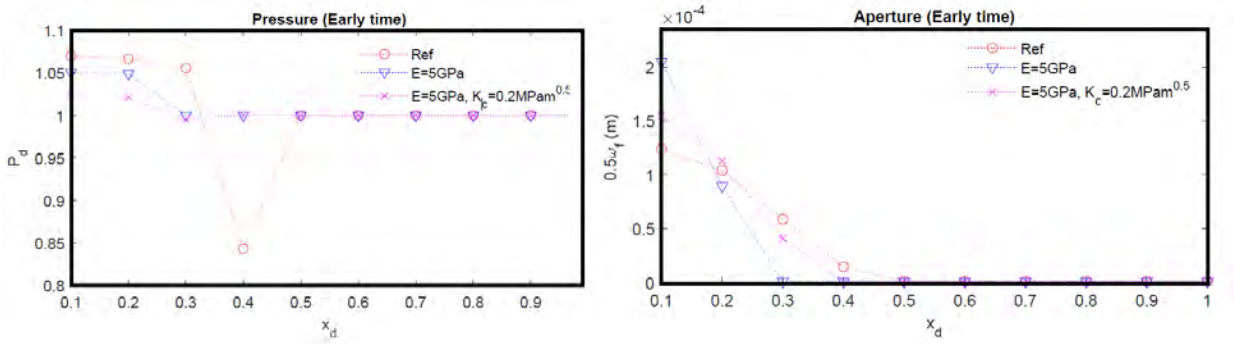

Figure 6.16: Distribution of pressure (left) and the fracture aperture (right) at $t_d = 1.62\times10^{-5}$ (Case 3).

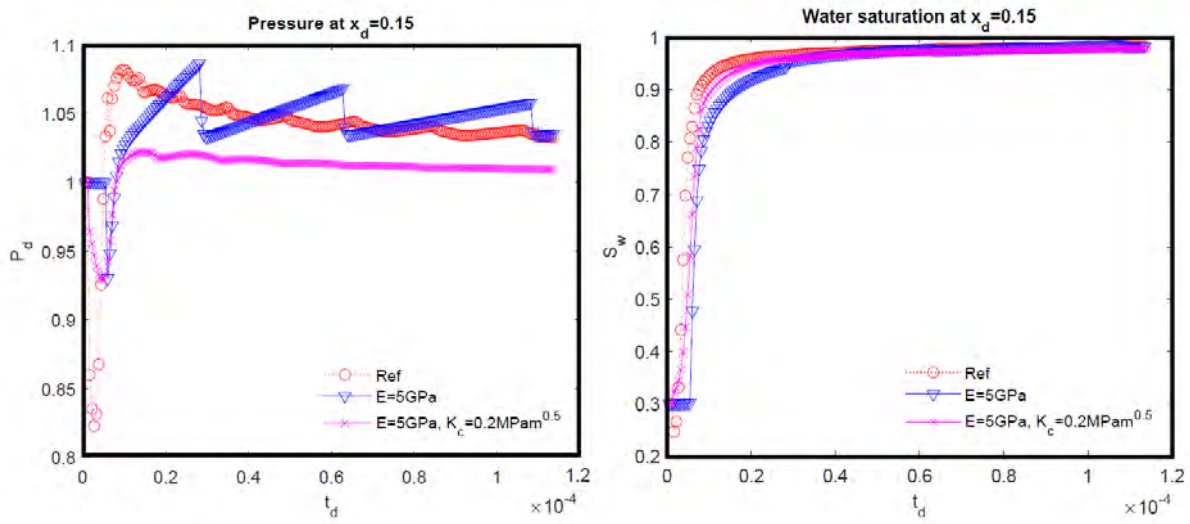

Figure 6.17: Evolution of pressure (left) and water saturation (right) at $x_d = 0.15$ (Case 3).

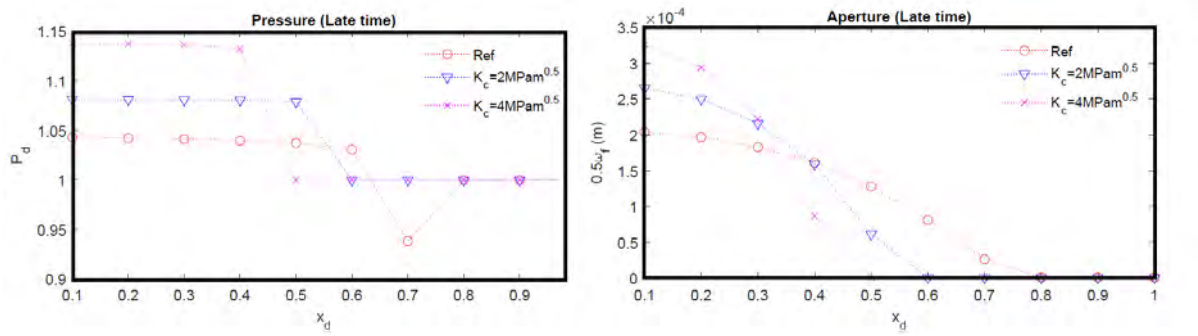

Figure 6.18: Distribution of pressure (left) and the fracture aperture (right) at $t_d = 5.41 \times 10^{-5}$ for the high toughness case.

6.5 Conclusion

Multiphase flow in the hydraulically fractured systems exhibits complex physical responses from strongly coupled flow and geomechanics such as the vacuum area and the dry zone. The vacuum area, an example of the Mandel-Cryer effect in the discrete fractured system, results from the difference in time scales between flow and geomechanics. The vacuum area caused by instantaneous pressure drop is mainly determined by fluid compressibility and fracture deformability. The dry zone is caused not only by the pressure gradient between the fracture and the reservoir formation but also by reservoir permeability and fluid mobility, and thus it is not necessarily identical to the vacuum area. The vacuum area and the dry zone are remarkable in a static fracture (naturally or previously hydraulically fractured) while they are less prominent in hydraulic fracturing in the homogenous reservoir because of the different length scales of the fractures. Since many reservoirs are naturally fractured in the real fields, the dry fractures can be found during hydraulic fracturing, which activates pre-existing fractures and combines them with dynamic fractures. We also identify that a hydraulic fracture propagates slowly when the initial total stress is higher than the initial reservoir pressure, when reservoir permeability or fracture toughness is high, or when Young's modulus is low. To capture the complex physics accurately, it is necessary to employ all-way coupled formulation that can consider

both fluid compressibility and the fracture volume change. The proposed sequentially (iteratively) coupled method motivated by the fixed stress method can solve the strongly coupled physical problems stably and accurately, facilitating using existing individual simulators of hydraulic fracturing geomechanics and multiphase flow. We emphasize that the stabilization term used in the flow equation depends on the fracture length. Since the 1D planar fracture is only considered in this study, the stabilization term might also depend on a fracture shape, which will be further investigated in the future for optimal convergence in the cases of various fracture shapes including nonplanar fractures.

7. SUMMARY

This study using coupled multiphase flow and geomechanics simulation investigates the effects of mechanical failure such as fault reactivation and slip with fluid injection in geological storage operations, wellbore stability issues stemming from depressurization in methane hydrate deposits, and fracture propagation in shale reservoirs. The simulator packages for flow and geomechanics with ~~fixed~~ stress sequential scheme are validated separately with the analytical solution for the McNamee and Gibson problem for each application.

In the first chapter, we design a fault structure with a fault core and surrounded damage zones. Zero-thickness interface elements are employed to represent the fault core with an assumption that the fault is reactivated only along the fault core. In this chapter, we test several cases with different injection scenarios (e.g., in-situ stresses and reservoir pressure) to estimate the impact of pore pressure on fault reactivation and its post-failure behavior. Results indicated that the time at which fault slippage occurs and the associated magnitude of the seismic moment ~~is~~ sensitive to the injection rates. Higher injection rates cause fault reactivation on a shorter time scale and a larger magnitude of seismic moment and vice-versa.

The work presented in the second chapter about the application of ~~CNN based~~ surrogate model on predictions of dynamic hydraulic and geomechanical properties uses multiple realizations of permeability distributions generated using Random Gaussian distribution and varying injection rates to train a surrogate model which on validation can predict the temporal variation of dynamic properties at regions of interest with reasonable accuracy. The idea is to show how such a workflow is indeed feasible and to build a roadmap for extending the application of a similar workflow that will be capable of predicting other properties like fault reactivation and its shear displacement considering the complexities of the system.

In the third chapter, we study how the dissociation of hydrate deposits (decrease in solid-phase saturation) directly influences the stiffness of the formation, which also leads to prob-

lematic deformation of the reservoir especially near the wellbore. The tightly coupled sequential approach with zero-thickness interface elements (discontinuous surface) allows us to consider both confining stress and slippage phenomena. We test several combinations of interface properties between the wellbore and the surrounding formation that are representative of varying completion quality in terms of cementation to select the proper pipe specifications that can endure the expected stress evolution due to depressurization. The results can thus be used as preliminary results for the safety design of the wellbore.

In the last chapter, we firstly identify the vacuum area and the dry zone for not only a static fracture case but also dynamic hydraulic fracture propagation. Then, we examine the numerical stability of hydraulic fracture propagation by changing the reservoir mechanical properties such as total stress, permeability, fracture toughness, and Young's modulus. Moreover, the results show that the fracture length is a key factor ~~in the stabilization term of the flow equation in case the fracture has a bi-wing shape~~.

REFERENCES

[1] H.-C. Gu and I. G. Hwang, "Depositional history of the janggi conglomerate controlled by tectonic subsidence, during the early stage of janggi basin evolution," *Journal of the Geological Society of Korea*, vol. 53, no. 2, pp. 221–240, 2017.

[2] J. Kim and G. J. Moridis, "Development of the t+ m coupled flow–geomechanical simulator to describe fracture propagation and coupled flow–thermal–geomechanical processes in tight/shale gas systems," *Computers & Geosciences*, vol. 60, pp. 184–198, 2013.

[3] S. Horozal, G. H. Lee, Y. Y. Bo, D. G. Yoo, K. P. Park, H. Y. Lee, W. Kim, H. J. Kim, and K. Lee, "Seismic indicators of gas hydrate and associated gas in the ulleung basin, east sea (japan sea) and implications of heat flows derived from depths of the bottom-simulating reflector," *Marine Geology*, vol. 258, no. 1-4, pp. 126–138, 2009.

[4] B.-J. Ryu, T. S. Collett, M. Riedel, G. Y. Kim, J.-H. Chun, J.-J. Bahk, J. Y. Lee, J.-H. Kim, and D.-G. Yoo, "Scientific results of the second gas hydrate drilling expedition in the ulleung basin (ubgh2)," *Marine and Petroleum Geology*, vol. 47, pp. 1–20, 2013.

[5] T. S. Collett, "Natural gas hydrates of the prudhoe bay and kuparuk river area, north slope, alaska," *AAPG bulletin*, vol. 77, no. 5, pp. 793–812, 1993.

[6] T. S. Collett, A. Johnson, C. C. Knapp, R. Boswell, *et al.*, *Natural Gas Hydrates: Energy Resource Potential and Associated Geologic Hazards, AAPG Memoir 89*, vol. 89. AAPG, 2010.

[7] P. A. Hsieh and J. D. Bredehoeft, "A reservoir analysis of the denver earthquakes: A case of induced seismicity," *Journal of Geophysical Research: Solid Earth*, vol. 86, no. B2, pp. 903–920, 1981.

[8] A. Mossop and P. Segall, "Subsidence at the geysers geothermal field, n. california from a comparison of gps and leveling surveys," *Geophysical Research Letters*, vol. 24, no. 14, pp. 1839–1842, 1997.

[9] P. Longuemare, J. L. Detienne, P. Lemonnier, and A. Onaisi, "Numerical modeling of fracture propagation induced by water injection/re-injection," in *SPE European Formation Damage Conference*, (The Hague, Netherlands), 21–22 May 2001. spe 68974.

[10] B. Dost, H. Haak, T. E. Wong, D. Batjes, and J. De Jager, "Natural and induced seismicity," *Geology of the Netherlands*, pp. 223–239, 2007.

[11] J. Rutqvist, J. Birkholzer, F. Cappa, and C.-F. Tsang, "Estimating maximum sustainable injection pressure during geological sequestration of co2 using coupled fluid flow and geomechanical fault-slip analysis," *Energy Conversion and Management*, vol. 48, no. 6, pp. 1798–1807, 2007.

[12] M. Bagheri and A. Settari, "Modeling of geomechanics in naturally fractured reservoirs," *SPE Reservoir Evaluation & Engineering*, vol. 11, no. 1, pp. 108–118, 2008.

[13] J. Rutqvist, D. W. Vasco, and L. Myer, "Coupled reservoir-geomechanical analysis of co2 injection and ground deformations at in salah, algeria," *International Journal of Greenhouse Gas Control*, vol. 4, no. 2, pp. 225–230, 2010.

[14] J. Kim, J. Y. Lee, *et al.*, "Wellbore stability and possible geomechanical failure in the vicinity of the well during pressurization at the gas hydrate deposit in the ulleung basin," in *53rd US Rock Mechanics/Geomechanics Symposium*, American Rock Mechanics Association, 2019.

[15] S. Bachu, "Co2 storage in geological media: Role, means, status and barriers to deployment," *Progress in energy and combustion science*, vol. 34, no. 2, pp. 254–273, 2008.

[16] S. M. Benson and D. R. Cole, "Co2 sequestration in deep sedimentary formations," *Elements*, vol. 4, no. 5, pp. 325–331, 2008.

[17] M. J. Bickle, "Geological carbon storage," *Nature Geoscience*, vol. 2, no. 12, pp. 815–818, 2009.

[18] K. Michael, A. Golab, V. Shulakova, J. Ennis-King, G. Allinson, S. Sharma, and T. Aiken, "Geological storage of co2 in saline aquifers?a review of the experience from existing storage operations," *International journal of greenhouse gas control*, vol. 4, no. 4, pp. 659–667, 2010.

[19] J. Rutqvist, "The geomechanics of co 2 storage in deep sedimentary formations," *Geotechnical and Geological Engineering*, vol. 30, no. 3, pp. 525–551, 2012.

[20] C. Hawkes, P. McLellan, S. Bachu, *et al.*, "Geomechanical factors affecting geological storage of co2 in depleted oil and gas reservoirs," *Journal of Canadian Petroleum Technology*, vol. 44, no. 10, 2005.

[21] J. Rutqvist, D. W. Vasco, and L. Myer, "Coupled reservoir-geomechanical analysis of co2 injection at in salah, algeria," *Energy Procedia*, vol. 1, no. 1, pp. 1847–1854, 2009.

[22] D. Vasco, A. Rucci, A. Ferretti, F. Novali, R. Bissell, P. Ringrose, A. Mathieson, and I. Wright, "Satellite-based measurements of surface deformation reveal fluid flow associated with the geological storage of carbon dioxide," *Geophysical Research Letters*, vol. 37, no. 3, 2010.

[23] L. Röhmann, E. Tillner, F. Magri, M. Kühn, and T. Kempka, "Fault reactivation and ground surface uplift assessment at a prospective german co2 storage site," *Energy Procedia*, vol. 40, pp. 437–446, 2013.

[24] J. P. Verdon, J.-M. Kendall, A. L. Stork, R. A. Chadwick, D. J. White, and R. C. Bissell, "Comparison of geomechanical deformation induced by megatonne-scale co2 storage

at sleipner, weyburn, and in salah," *Proceedings of the National Academy of Sciences*, vol. 110, no. 30, pp. E2762–E2771, 2013.

[25] M. Shirzaei, W. L. Ellsworth, K. F. Tiampo, P. J. González, and M. Manga, "Surface uplift and time-dependent seismic hazard due to fluid injection in eastern texas," *Science*, vol. 353, no. 6306, pp. 1416–1419, 2016.

[26] E. Hooper, "Fluid migration along growth faults in compacting sediments," *Journal of Petroleum Geology*, vol. 14, pp. 161–180, 1991.

[27] S. A. Miller, C. Collettini, L. Chiaraluce, M. Cocco, M. Barchi, and B. J. Kaus, "Aftershocks driven by a high-pressure co 2 source at depth," *Nature*, vol. 427, no. 6976, pp. 724–727, 2004.

[28] L. W. Teufel *et al.*, "Permeability changes during shear deformation of fractured rock," in *The 28th US Symposium on Rock Mechanics (USRMS)*, American Rock Mechanics Association, 1987.

[29] A. Makurat, N. Barton, N. Rad, and S. Bandis, "Joint conductivity variation due to normal and shear deformation," *Publikasjon-Norges Geotekniske Institutt*, vol. 182, pp. 1–6, 1991.

[30] Z. Chen, S. Narayan, Z. Yang, and S. Rahman, "An experimental investigation of hydraulic behaviour of fractures and joints in granitic rock," *International Journal of Rock Mechanics and Mining Sciences*, vol. 37, no. 7, pp. 1061–1071, 2000.

[31] Z. K. Shipton, J. P. Evans, D. Kirschner, P. T. Kolesar, A. P. Williams, and J. Heath, "Analysis of co2 leakage through low-permeability faults from natural reservoirs in the colorado plateau, east-central utah," *Geological Society, London, Special Publications*, vol. 233, no. 1, pp. 43–58, 2004.

[32] J. L. Lewicki, J. Birkholzer, and C.-F. Tsang, "Natural and industrial analogues for leakage of co2 from storage reservoirs: identification of features, events, and processes

and lessons learned," *Environmental Geology*, vol. 52, no. 3, p. 457, 2007.

[33] L. L. Chyi, T. J. Quick, T. F. Yang, and C. Cheng-Hong, "Soil gas radon spectra and earthquakes," *TAO: Terrestrial, Atmospheric and Oceanic Sciences*, vol. 16, no. 4, p. 763, 2005.

[34] S. Singh, A. Kumar, B. S. Bajwa, S. Mahajan, V. Kumar, and S. Dhar, "Radon monitoring in soil gas and ground water for earthquake prediction studies in north west himalayas, india," *TAO: Terrestrial, Atmospheric and Oceanic Sciences*, vol. 21, no. 4, p. 6, 2010.

[35] P. Richon, Y. Klinger, P. Tapponnier, C.-X. Li, J. Van Der Woerd, and F. Perrier, "Measuring radon flux across active faults: Relevance of excavating and possibility of satellite discharges," *Radiation Measurements*, vol. 45, no. 2, pp. 211–218, 2010.

[36] C. Marone, "Laboratory-derived friction laws and their application to seismic faulting," *Annual Review of Earth and Planetary Sciences*, vol. 26, no. 1, pp. 643–696, 1998.

[37] J. Healy, W. Rubey, D. Griggs, and C. Raleigh, "The denver earthquakes," *Science*, vol. 161, no. 3848, pp. 1301–1310, 1968.

[38] C. Raleigh, J. Healy, and J. Bredehoeft, "An experiment in earthquake control at rangely, colorado," *Science*, vol. 191, no. 4233, pp. 1230–1237, 1976.

[39] M. D. Zoback and H.-P. Harjes, "Injection-induced earthquakes and crustal stress at 9 km depth at the ktb deep drilling site, germany," *Journal of Geophysical Research: Solid Earth*, vol. 102, no. B8, pp. 18477–18491, 1997.

[40] M. O. Häring, U. Schanz, F. Ladner, and B. C. Dyer, "Characterisation of the basel 1 enhanced geothermal system," *Geothermics*, vol. 37, no. 5, pp. 469–495, 2008.

[41] I. Moeck, G. Kwiatek, and G. Zimmermann, "Slip tendency analysis, fault reactivation potential and induced seismicity in a deep geothermal reservoir," *Journal of Structural Geology*, vol. 31, no. 10, pp. 1174–1182, 2009.

[42] J. Verdon, J.-M. Kendall, D. White, and D. Angus, "Linking microseismic event observations with geomechanical models to minimise the risks of storing co2 in geological formations," *Earth and Planetary Science Letters*, vol. 305, no. 1-2, pp. 143–152, 2011.

[43] W. L. Ellsworth, "Injection-induced earthquakes," *Science*, vol. 341, no. 6142, 2013.

[44] K.-H. Kim, J.-H. Ree, Y. Kim, S. Kim, S. Y. Kang, and W. Seo, "Assessing whether the 2017 mw 5.4 pohang earthquake in south korea was an induced event," *Science*, vol. 360, no. 6392, pp. 1007–1009, 2018.

[45] W. L. Ellsworth, D. Giardini, J. Townend, S. Ge, and T. Shimamoto, "Triggering of the pohang, korea, earthquake (m w 5.5) by enhanced geothermal system stimulation," *Seismological Research Letters*, vol. 90, no. 5, pp. 1844–1858, 2019.

[46] Z. L. Jin, T. Garipov, O. Volkov, L. J. Durlofsky, *et al.*, "Reduced-order modeling of coupled flow and quasistatic geomechanics," *SPE Journal*, vol. 25, no. 01, pp. 326–346, 2020.

[47] M. Tang, Y. Liu, and L. J. Durlofsky, "A deep-learning-based surrogate model for data assimilation in dynamic subsurface flow problems," *Journal of Computational Physics*, vol. 413, p. 109456, 2020.

[48] M. Tang, X. Ju, and L. J. Durlofsky, "Deep-learning-based coupled flow-geomechanics surrogate model for co _2 sequestration," *arXiv preprint arXiv:2105.01334*, 2021.

[49] Y. Liu and L. J. Durlofsky, "3d cnn-pca: A deep-learning-based parameterization for complex geomodels," *Computers & Geosciences*, vol. 148, p. 104676, 2021.

[50] J. Kim, H. Yang, and J. Choe, "Robust optimization of the locations and types of multiple wells using cnn based proxy models," *Journal of Petroleum Science and Engineering*, vol. 193, p. 107424, 2020.

[51] Z. L. Jin, Y. Liu, and L. J. Durlofsky, "Deep-learning-based reduced-order modeling for subsurface flow simulation," *arXiv preprint arXiv:1906.03729*, 2019.

[52] G. Wen, M. Tang, and S. M. Benson, "Towards a predictor for co2 plume migration using deep neural networks," *International Journal of Greenhouse Gas Control*, vol. 105, p. 103223, 2021.

[53] J.-T. Kim, A.-R. Kim, G.-C. Cho, C.-W. Kang, and J. Y. Lee, "The effects of coupling stiffness and slippage of interface between the wellbore and unconsolidated sediment on the stability analysis of the wellbore under gas hydrate production," *Energies*, vol. 12, no. 21, p. 4177, 2019.

[54] G. Moridis, J. Kim, M. Reagan, and S. Kim, "Feasibility of gas production from a gas hydrate accumulation at the ubgh2-6 site of the ulleung basin in the korean east sea," *Journal of Petroleum Science and Engineering*, vol. 108, pp. 180–210, 2013.

[55] R. Boswell, K. Rose, T. S. Collett, M. Lee, W. Winters, K. A. Lewis, and W. Agena, "Geologic controls on gas hydrate occurrence in the mount elbert prospect, alaska north slope," *Marine and Petroleum Geology*, vol. 28, no. 2, pp. 589–607, 2011.

[56] T. S. Collett, "Arctic gas hydrate energy assessment studies," *The Arctic Energy Summit, Anchorage, Alaska*, pp. 15–18, 2007.

[57] G. J. Moridis, M. T. Reagan, K. Boyle, K. Zhang, *et al.*, "Evaluation of a deposit in the vicinity of the pbu l-106 site, north slope, alaska, for a potential long-term test of gas production from hydrates," in *SPE Western Regional Meeting*, Society of Petroleum Engineers, 2010.

[58] G. J. Moridis, "Numerical studies of gas production from methane hydrates," *SPE Journal*, vol. 8, no. 4, pp. 359–370, 2003.

[59] M. T. Reagan and G. J. Moridis, "Large-scale simulation of methane hydrate dissociation along the west spitsbergen margin," *Geophysical Research Letters*, vol. 36, p. L23612 5pp., 2009.

[60] J. W. Wilder, G. J. Moridis, S. J. Wilson, M. Kurihara, M. D. White, Y. Masuda, B. J. Anderson, T. S. Collett, R. B. Hunter, H. Narita, *et al.*, "An international effort to compare gas hydrate reservoir simulators," in *Proceedings of 6th International Conference on Gas Hydrates (ICGH 2008), Vancouver, CANADA*, 2008.

[61] J. Rutqvist, "Status of the tough-flac simulator and recent applications related to coupled fluid flow and crustal deformations," *Computers & Geosciences*, vol. 37, no. 6, pp. 739–750, 2011.

[62] F. Itasca, "Fast lagrangian analysis of continua in 3 dimensions," *Online Manual*, 2013.

[63] B. Häggblad and G. Nordgren, "Modelling nonlinear soil-structure interaction using interface elements, elastic-plastic soil elements and absorbing infinite elements," *Computers & Structures*, vol. 26, no. 1-2, pp. 307–324, 1987.

[64] J. Rutqvist, G. Moridis, T. Grover, S. Silpngarmlert, T. Collett, and S. Holdich, "Coupled multiphase fluid flow and wellbore stability analysis associated with gas production from oceanic hydrate-bearing sediments," *Journal of petroleum science and engineering*, vol. 92, pp. 65–81, 2012.

[65] P. Fu, S. M. Johnson, and C. R. Carrigan, "An explicitly coupled hydro-geomechanical model for simulating hydraulic fracturing in arbitrary discrete fracture networks," *International Journal for Numerical and Analytical Methods in Geomechanics*, vol. 37, no. 14, pp. 2278–2300, 2013.

[66] X.-P. Zhang and L. N. Y. Wong, "Loading rate effects on cracking behavior of flaw-contained specimens under uniaxial compression," *International Journal of Fracture*, vol. 180, no. 1, pp. 93–110, 2013.

[67] R. I. Borja, "Assumed enhanced strain and the extended finite element methods: A unification of concepts," *Computer methods in applied mechanics and engineering*, vol. 197, no. 33-40, pp. 2789–2803, 2008.

[68] N. Moës, J. Dolbow, and T. Belytschko, "A finite element method for crack growth without remeshing," *International journal for numerical methods in engineering*, vol. 46, no. 1, pp. 131–150, 1999.

[69] A. Ghassemi and Q. Zhang, "Porothermoelastic analysis of the response of a stationary crack using the displacement discontinuity method," *Journal of engineering mechanics*, vol. 132, no. 1, pp. 26–33, 2006.

[70] A. Ghassemi and X. Zhou, "A three-dimensional thermo-poroelastic model for fracture response to injection/extraction in enhanced geothermal systems," *Geothermics*, vol. 40, no. 1, pp. 39–49, 2011.

[71] L. Xie, K.-B. Min, and B. Shen, "Simulation of hydraulic fracturing and its interactions with a pre-existing fracture using displacement discontinuity method," *Journal of Natural Gas Science and Engineering*, vol. 36, pp. 1284–1294, 2016.

[72] T. Heister, M. F. Wheeler, and T. Wick, "A primal-dual active set method and predictor-corrector mesh adaptivity for computing fracture propagation using a phase-field approach," *Computer Methods in Applied Mechanics and Engineering*, vol. 290, pp. 466–495, 2015.

[73] T. Wick, "Modified newton methods for solving fully monolithic phase-field quasi-static brittle fracture propagation," *Computer Methods in Applied Mechanics and Engineering*, vol. 325, pp. 577–611, 2017.

[74] S. Lee, M. F. Wheeler, and T. Wick, "Pressure and fluid-driven fracture propagation in porous media using an adaptive finite element phase field model," *Computer Methods in Applied Mechanics and Engineering*, vol. 305, pp. 111–132, 2016.

[75] R. Gritto and S. P. Jarpe, "Temporal variations of vp/vs-ratio at the geysers geothermal field, usa," *Geothermics*, vol. 52, pp. 112–119, 2014.

[76] M. Commer, G. M. Hoversten, and E. S. Um, "Transient-electromagnetic finite-difference time-domain earth modeling over steel infrastructure," *Geophysics*, vol. 80, no. 2, pp. E147–E162, 2015.

[77] E. S. Um, J. Kim, M. J. Wilt, M. Commer, and S.-S. Kim, "Finite-element analysis of top-casing electric source method for imaging hydraulically active fracture zones," *Geophysics*, vol. 84, no. 1, pp. E23–E35, 2019.

[78] J. Geertsma, F. De Klerk, *et al.*, "A rapid method of predicting width and extent of hydraulically induced fractures," *Journal of petroleum technology*, vol. 21, no. 12, pp. 1–571, 1969.

[79] E. Detournay, "Propagation regimes of fluid-driven fractures in impermeable rocks," *International Journal of Geomechanics*, vol. 4, no. 1, pp. 35–45, 2004.

[80] J. Adachi, m. Siebrits, E, A. Peirce, and J. Desroches, "Computer simulation of hydraulic fractures," *International Journal of Rock Mechanics and Mining Sciences*, vol. 44, no. 5, pp. 739–757, 2007.

[81] K. T. Raterman, H. E. Farrell, O. S. Mora, A. L. Janssen, G. A. Gomez, S. Busetti, J. McEwen, K. Friehauf, J. Rutherford, R. Reid, *et al.*, "Sampling a stimulated rock volume: An eagle ford example," *SPE Reservoir Evaluation & Engineering*, vol. 21, no. 04, pp. 927–941, 2018.

[82] J. Kim and G. J. Moridis, "Numerical analysis of fracture propagation during hydraulic fracturing operations in shale gas systems," *International Journal of Rock Mechanics and Mining Sciences*, vol. 76, pp. 127–137, 2015.

[83] S. Salimzadeh, A. Paluszny, and R. W. Zimmerman, "Three-dimensional poroelastic effects during hydraulic fracturing in permeable rocks," *International Journal of Solids and Structures*, vol. 108, pp. 153–163, 2017.

[84] J. Kim, H. A. Tchelepi, and R. Juanes, "Stability and convergence of sequential methods for coupled flow and geomechanics: Fixed-stress and fixed-strain splits," *Computer Methods in Applied Mechanics and Engineering*, vol. 200, no. 13-16, pp. 1591–1606, 2011.

[85] A. Mikelić and M. F. Wheeler, "Convergence of iterative coupling for coupled flow and geomechanics," *Computational Geosciences*, vol. 17, no. 3, pp. 455–461, 2013.

[86] M. Parchei Esfahani and R. Gracie, "On the undrained and drained hydraulic fracture splits," *International Journal for Numerical Methods in Engineering*, vol. 118, no. 12, pp. 741–763, 2019.

[87] J. Kim, H. A. Tchelepi, and R. Juanes, "Stability and convergence of sequential methods for coupled flow and geomechanics: Drained and undrained splits," *Computer Methods in Applied Mechanics and Engineering*, vol. 200, no. 23-24, pp. 2094–2116, 2011.

[88] K. Aziz and A. Settari, *Petroleum Reservoir Simulation*. London: Elsevier, 1979.

[89] O. Coussy, *Mechanics of porous continua*. Chichester, England: John Wiley and Sons, 1995.

[90] M. A. Biot, "General theory of three-dimensional consolidation," *Journal of Applied Physics*, vol. 12, pp. 155–164, 1941.

[91] M. A. Biot and D. G. Willis, "The elastic coefficients of the theory of consolidation," *Journal of Applied Physics*, pp. 594–01, 1957.

[92] J. Geertsma, "The effect of fluid pressure decline on volumetric change of porous rocks," *Petroleum Transactions, AIME*, vol. 210, pp. 331–340, 1957.

[93] R. W. Lewis and B. A. Schrefler, *The finite element method in the static and dynamic deformation and consolidation of porous media*. Chichester, England: Wiley, second ed., 1998.

[94] D. Snow, *A parallel plate model of fractured permeable media*. Ph.D. Dissertation, Stanford University, 1965.

[95] J. Rutqvist and O. Stephansson, "The role of hydromechanical coupling in fractured rock engineering," *Hydrogeology Journal*, vol. 11, pp. 7–40, 2003.

[96] M. Zeghal and T. B. Edil, "Soil structure interaction analysis: modeling the interface," *Canadian Geotechnical Journal*, vol. 39, no. 3, pp. 620–628, 2002.

[97] R. Rosso, "A comparison of joint stiffness measurements in direct shear, triaxial compression, and in situ," in *International journal of rock mechanics and mining sciences & geomechanics abstracts*, vol. 13, pp. 167–172, Elsevier, 1976.

[98] M. Guatteri and P. Spudich, "What can strong-motion data tell us about slip-weakening fault-friction laws?," *Bulletin of the Seismological Society of America*, vol. 90, no. 1, pp. 98–116, 2000.

[99] R. E. Abercrombie and J. R. Rice, "Can observations of earthquake scaling constrain slip weakening?," *Geophysical Journal International*, vol. 162, no. 2, pp. 406–424, 2005.

[100] J. Rutqvist, F. Cappa, A. Rinaldi, and M. Godano, "Modeling of induced seismicity and ground vibrations associated with geologic co2 storage, and assessing their effects on surface structures and human perception," *International Journal of Greenhouse Gas Control*, vol. 24, pp. 64–77, 2014.

[101] A. P. Rinaldi, J. Rutqvist, and F. Cappa, "Geomechanical effects on co2 leakage through fault zones during large-scale underground injection," *International Journal of Greenhouse Gas Control*, vol. 20, pp. 117–131, 2014.

[102] J. L. Gidley, S. A. Holditch, D. E. Nierode, and R. W. J. Veatch, "Recent advances in hydraulic fracturing," in *SPE Monograph Series Vol. 12*, 1990.

[103] K. Pruess, *ECO2N: A TOUGH2 fluid property module for mixtures of water, NaCl, and CO2*. Lawrence Berkeley National Laboratory Berkeley, CA, 2005.

[104] J. McNamee and R. Gibson, "Displacement functions and linear transformations applied to diffusion through porous elastic media," *The Quarterly Journal of Mechanics and Applied Mathematics*, vol. 13, pp. 98–111, 1960.

[105] J. McNamee and R. Gibson, "Plane strain and axially symmetric problems of the consolidation of a semi-infinite clay stratum," *The Quarterly Journal of Mechanics and Applied Mathematics*, vol. 13, pp. 210–227, 1960.

[106] C. Cryer, "A comparison of the three-dimensional consolidation theories of biot and terzaghi," *The Quarterly Journal of Mechanics and Applied Mathematics*, vol. 16, no. 4, pp. 401–412, 1963.

[107] J. Rice, J. Rudnicki, and D. A. Simons, "Deformation of spherical cavities and inclusions in fluid-infiltrated elastic materials," *International Journal of Solids and Structures*, vol. 14, no. 4, pp. 289–303, 1978.

[108] M.-C. Kim, Y. S. Gihm, E.-Y. Son, M. Son, I. G. Hwang, Y. J. Shinn, and H. Choi, "Assessment of the potential for geological storage of co2 based on structural and sedimentologic characteristics in the miocene janggi basin," *Journal of the geological society of Korea*, vol. 51, no. 3, pp. 253–271, 2015.

[109] M. D. Zoback and S. M. Gorelick, "Earthquake triggering and large-scale geologic storage of carbon dioxide," *Proceedings of the National Academy of Sciences*, vol. 109, no. 26, pp. 10164–10168, 2012.

[110] J. Rutqvist and C.-F. Tsang, "A study of caprock hydromechanical changes associated with co 2-injection into a brine formation," *Environmental Geology*, vol. 42, no. 2-3, pp. 296–305, 2002.

[111] L. Langhi, Y. Zhang, A. Gartrell, J. Underschultz, and D. Dewhurst, "Evaluating hydrocarbon trap integrity during fault reactivation using geomechanical three-dimensional modeling: An example from the timor sea, australia," *AAPG bulletin*, vol. 94, no. 4, pp. 567–591, 2010.

[112] F. Cappa and J. Rutqvist, "Impact of co2 geological sequestration on the nucleation of earthquakes," *Geophysical Research Letters*, vol. 38, p. L17313, 2011.

[113] A. Mazzoldi, A. P. Rinaldi, A. Borgia, and J. Rutqvist, "Induced seismicity within geological carbon sequestration projects: maximum earthquake magnitude and leakage potential from undetected faults," *International Journal of Greenhouse Gas Control*, vol. 10, pp. 434–442, 2012.

[114] H. Kanamori, "The diversity of the physics of earthquakes," *Proceedings of the Japan Academy, Series B*, vol. 80, no. 7, pp. 297–316, 2004.

[115] S. K. Chough, H. J. Lee, and S. H. Yoon, *Marine geology of Korean seas*. Elsevier, 2000.

[116] W. J. Ludwig, S. Murauchi, and R. E. Houtz, "Sediments and structure of the japan sea," *Geological Society of America Bulletin*, vol. 86, no. 5, pp. 651–664, 1975.

[117] Y. K. Kwon and S. K. Chough, "Sequence stratigraphy of the cyclic successions in the dumugol formation (lower ordovician), mideast korea," *Geosciences Journal*, vol. 9, no. 4, p. 305, 2005.

[118] J.-J. Bahk, G.-Y. Kim, J.-H. Chun, J.-H. Kim, J. Lee, B.-J. Ryu, J.-H. Lee, B.-K. Son, and T. S. Collett, "Characterization of gas hydrate reservoirs by integration of core and log data in the ulleung basin, east sea," *Marine and petroleum geology*, vol. 47, pp. 30–42, 2013.

[119] H.-S. Kim, G.-C. Cho, J. Y. Lee, and S.-J. Kim, "Geotechnical and geophysical properties of deep marine fine-grained sediments recovered during the second ulleung basin

gas hydrate expedition, east sea, korea," *Marine and petroleum geology*, vol. 47, pp. 56–65, 2013.

[120] G. J. Moridis, J. Kim, M. T. Reagan, and S.-J. Kim, "Feasibility of gas production from a gas hydrate accumulation at the ubgh2-6 site of the ulleung basin in the korean east sea," *Journal of Petroleum Science and Engineering*, vol. 108, pp. 180–210, 2013.

[121] E. Ryu, S. Yi, and S.-J. Lee, "Late pleistocene–holocene paleoenvironmental changes inferred from the diatom record of the ulleung basin, east sea (sea of japan)," *Marine Micropaleontology*, vol. 55, no. 3-4, pp. 157–182, 2005.

[122] Y. Makogon, "Gas hydrates: the frozen energy," *Recherche;(France)*, vol. 18, no. 192, 1987.

[123] J. Kim, G. J. Moridis, and J. Rutqvist, "Coupled flow and geomechanical analysis for gas production in the prudhoe bay unit l-106 well unit c gas hydrate deposit in alaska," *Journal of petroleum science and engineering*, vol. 92, pp. 143–157, 2012.

[124] J. Kim, G. J. Moridis, D. Yang, and J. Rutqvist, "Numerical studies on two-way coupled fluid flow and geomechanics in hydrate deposits," *SPEJ*, vol. 17, no. 2, pp. 485–501, 2012.

[125] H. F. Bueckner, "Crack problems in the classical theory of elasticity (in sneddon and m. lowengrub)," 1971.

[126] J. Geertsma and F. de Klerk, "A rapid method of predicting width and extent of hydraulically induced fractures," *Journal of Petroleum Technology*, vol. 21, pp. 1571–1581, 1969. SPE 2458.

[127] F. Tzschichholz and H. Herrmann, "Simulations of pressure fluctuations and acoustic emission in hydraulic fracturing," *Physical Review E*, vol. 51, no. 3, p. 1961, 1995.

[128] R. H. Dean and J. H. Schmidt, "Hydraulic fracture predictions with a fully coupled geomechanical reservoir simulation," *SPEJ*, vol. 14, no. 4, pp. 707–714, 2009.